Ph.D Thesis

July 30, 2008

Study of direct production and polarization measurement of J/ψ at the ATLAS experiment

Jonatan Ginzburg

Supervisor prof. E. Etzion

Tel Aviv University, Israel

Abstract

The ATLAS B-physics program covers many aspects of charm and beauty flavour physics. Among the earliest are measuring the production cross-sections of beauty and charm hadrons and of the heavy-flavour quarkonium, J/ψ and Υ. These will provide a sensitive test bed of QCD predictions for production in proton-proton collisions at the LHC energies. While the main B-physics measurements will be taken with an instantaneous luminosity of around $10^{33} cm^{-2} s^{-1}$, the B-physics potential begins during the early data taking at lower luminosity of $10^{31} cm^{-2} s^{-1}$. With an integrated luminosity of 10 pb^{-1} ATLAS will already be able to register about $15 \cdot 10^4$ events containing $J/\psi \rightarrow \mu^+\mu^-$ selected by the low luminosity trigger menu. Recorded events will contain $J/\psi(\mu\mu)$ produced both directly in proton proton interactions as well as indirectly from decays of B hadrons. With this statistics, beauty and quarkonia studies will play a key role in the early data-taking period. J/ψ and its decay to di-muon final state will be utilized in calibration, alignment and determination of the trigger efficiencies. The availability of large sample of J/ψ decay to muon pairs for these studies, especially at initial low luminosity, will depend strongly on reaching the lowest p_T threshold and obtaining good understanding of the trigger performance and the tracking system.

In this thesis we present a study of the ATLAS reach for the analysis of the J/ψ production in proton proton interaction at 14 TeV. The study focuses on the decays of the charmonium to muon pair. We discuss methods of separating promptly produced J/ψ mesons from various background sources and review the ATLAS accessible range in transverse momentum and pseudorapidity and its implication on the spin alignment of the vector states. The separation of potential quarkonia production mechanism suggested by the theories and the feasibility of observing radiative decays of χ_c decays is discussed.

Contents

List of Figures

List of Tables

1 Introduction and theoretical motivations

When switched on, the LHC will produce large number of charm quarks even in low luminosity runs during the first few years of running. The number of produced quarkonium states such as J/ψ , important for many physics studies, will also be large. The reasonable branching fraction of the J/ψ into charged lepton pairs allows for easy separation of these events from the huge hadronic background at the LHC.

The importance of $J/\psi \rightarrow \mu^{+}\mu^{-}$ decay for ATLAS is first, being narrow resonances, they can be used as tools for alignment and calibration of the trigger, tracking and muon systems. Secondly, understanding the details of the prompt charmonia production is a challenging task and a good testbed for various QCD calculations, spanning both perturbative and non-perturbative regimes through the creation of heavy quarks in the hard process and their subsequent evolution into physical bound states.

This thesis mainly concentrates on the capabilities of the ATLAS detector to study various aspects of prompt charmonia production and polarization measurement at LHC. The methods of separating promptly produced J/ψ mesons from various backgrounds and the way to measure its polarization are discussed, as well as suggested ways of offline data quality monitoring based on J/ψ reconstruction and analysis.

1.1 The Standart Model

The experimental discoveries and theoretical developments of the last 50 years have led to the development of the Standard Model of particle physics [1]. The uniting principle of modern fundamental physics is that of symmetry. In addition to the familiar spacetime symmetries and discrete symmetries, it appears that Nature exhibits local gauge symmetries. There exists a deep connection between local gauge symmetries and physical interactions: the phase variation permitted by local symmetry is reconciled by a field which is considered to be the mediator of interactions between matter particles. The Standard Model is a gauge field theory with local gauge invariance. It describes all of the known fundamental particles and their interactions via three of the four known forces of nature: electromagnetism, the weak force and the strong force. Gravity is by far the weakest of the four forces, and is not described within the Standard Model. There are three types of particle described in the Standard Model: spin $1/2$ fermions (matter particles), spin 1 gauge bosons (which mediate interactions between matter particles), and a spin-0 Higgs boson [2] (which is a consequence of spontaneous symmetry breaking). The up and down quarks, the electron, and the electron neutrino are all that is needed to make up normal matter. For reasons unknown, this pattern is repeated three times, that is, for three "generations", each generation containing two quarks, a lepton and a neutrino (see Table 1).

The electromagnetic force is described in extremely good agreement with experiment by quantum electrodynamics (QED), a gauge field theory with local gauge in-

gen 1	gen 2	gen 3	T	T^3	Y	Q
$\begin{pmatrix}\nu_e \\ e\end{pmatrix}_L$	$\begin{pmatrix}\nu_\mu \\ \mu\end{pmatrix}_L$	$\begin{pmatrix}\nu_\tau \\ \tau\end{pmatrix}_L$	+1/2	$\begin{pmatrix}+1/2 \\ -1/2\end{pmatrix}$	+1	$\begin{pmatrix}0 \\ 1\end{pmatrix}$
e_R	μ_R	τ_R	0	0	-2	-1
$\begin{pmatrix}u \\ d\end{pmatrix}_L$	$\begin{pmatrix}c \\ s\end{pmatrix}_L$	$\begin{pmatrix}t \\ b\end{pmatrix}_L$	+1/2	$\begin{pmatrix}+1/2 \\ -1/2\end{pmatrix}$	+1/3	$\begin{pmatrix}+2/3 \\ -1/3\end{pmatrix}$
u_R	c_R	t_R	0	0	+4/3	+2/3
d_R	s_R	b_R	0	0	-2/3	-1/3

Table 1: Fermion multiplet assignments and quantum numbers T (weak isospin), T^3 (third component of weak isospin), Y (hypercharge) and Q (electric charge).

variance. It describes the interaction between particles carrying electric charge via a massless spin-1 gauge boson the photon. The electromagnetic and weak forces are described in the Standard Model in the "unified" framework of the electroweak model. Experimental evidence suggested that the weak force should be mediated by three massive vector bosons $W^\pm$ and Z^0. One of the major blocks in the development of a field theory description of the weak force was a way of permitting the gauge bosons to be massive, but also maintaining the renormalisability essential for a predictive theory. A solution to this problem is the so-called Higgs mechanism (one massive scalar particle, whose mass is not specified in the theory). The strong force is described in the Standard Model by quantum chromodynamics (QCD) [3] as described in the next section. At the time of writing, no experimental result has been conclusively shown to disagree with the predictions of the Standard Model. There is perhaps one exception the indication of neutrino masses which are not part of the model and would require an extension. The most significant confirmation of the approach taken in the Standard Model is surely the discovery in 1984 of the $W^\pm$ and Z^0 at the expected masses. The top quark was discovered 1995, leaving the Higgs boson as the only remaining particle of the Standard Model which has not been found. Resolution of the puzzle of electroweak symmetry breaking is currently one of the most burning issues in High-Energy Physics, and is one of the main reasons the for constructing of the Large Hadron Collider.

1.2 Quantum Chromodynamics and Hadron Production

1.2.1 QCD Introduction

Like the precisely tested QED and Electroweak theories, QCD is a local gauge field theory. It is based on the color SU(3) symmetry. Quarks are color triplets, having three components of color, denoted red, green and blue. Anti-quarks meanwhile possess three types of analogous anti-color. In terms of group theory, quarks and anti-quarks transform respectively under the three-dimensional 3 and $\tilde{3}$ representations of the gauge group SU(3). The gauge bosons of the theory are the gluons, which couple to color. Gluons themselves are color octets, transforming under the eight-dimensional representation 8 of SU(3). Since they carry color, gluons can interact among themselves as the weak vector bosons do. However, like the photon, they are massless. The six flavors of quarks have a wide range of masses, varying from well under 1 GeV/c^2 for the up, down and strange quarks to about 175 GeV/c^2 for the top quark. Up, down and strange are called light quarks, while charm, bottom and top are called heavy quarks, for reasons, which will become evident below. The strong force acts on quarks independently of their flavor, although their different masses result in different behaviors. Quarks appear point-like at the scale of $\sim 10^{-18} m$, the current limit of experimental resolution [4]. Quarks and gluons have never been observed as free particles. This fact is included in QCD as the "color confinement" hypothesis, which states that naturally occurring states are all colorless. Therefore, $q\tilde{q}$ and qqq states are allowed because the individual quark colors may combine to form a color singlet state, whereas qq states, for example, are not [1)]. Color may seem more like a mathematical convenience than a genuine property, but its existence is confirmed by a wide variety of experimental evidences [6]. The strong force between hadrons, such as nucleons in a nucleus, is somewhat different from the strong force between quarks, because hadrons are colorless. It is understood as being carried by colorless mesons, such as the pion, and may be thought of as a "residual" strong force.

In weakly bound systems (hydrogen, for example) the components may be separated if sufficient energy is added, for example in the form of a collision. However, in QCD bound systems, it is generally understood that the binding force is too strong for this to occur, regardless of the amount of energy added. If a hadron is struck hard, the constituent quarks do not simply come free. Rather, additional $q\bar{q}$ pairs are generated from the color field, and recombine to form more hadrons. This process of generating $q\bar{q}$ pairs in energetic strong interactions is central to models of hadron production.

The strong coupling constant α_s parameterized the strength of the quark-gluon and gluon-gluon couplings, and it is analogous to the electromagnetic coupling constant α.

The value of α_s depends on the transverse momentum of the process being studied, a characteristic known as 'running coupling constant'. At low energies, E $<$ 1 GeV, the coupling is so strong that perturbation theory breaks down . At higher energies α_s decreases, becoming small enough for perturbation theory to be applied reliably. This decrease in α_s implies that in the limit of very high energies, quarks behave as free particles, a property known as asymptotic freedom. In general, perturbative QCD successfully describes hard processes in high energy collisions produced at modern par-

[1)] Color-less bound states of gluons may exist, although no candidates have yet been confirmed [5] ticle colliders. However, the understanding of strong dynamics at low energies remains a major challenge for particle physics. With perturbation theory unavailable, a variety of theoretical models must be applied to different situations. For example, the original quark model is very useful in classifying hadrons and understanding their quantum numbers. However, it does not include any dynamics and therefore is not able to predict quantities such as masses or scattering cross sections. Meanwhile, several models exist to deal with the process of hadronization, the evolution of a single energetic quark or gluon into a jet of hadrons. These models can be tested in the study of jet production at collider experiments.

1.2.2 Quarkonium production

The heavy charm quarks are valuable to the study of QCD because their mass, on the order of 1.5 GeV/c^2 , are large enough for perturbation theory to be at least somewhat applicable . The 'charmonia' states of $c\bar{c}$ are the weel-understood hadrons . These are to some extent nonrelativistic systems, and so are analogous to electromagnetically bound systems like hydrogen or positronium. Charmonia may thus be modeled as a quark and an anti-quark moving in a central potential, leaving the form of the potential to be fitted to data [7]. Table 2 lists the masses and other properties of the bound quarkonium states, and Figure 2 shows the energy levels of bound charmonium states. In this context, 'bound' refers to states with mass below the open-flavor threshold ($2m_D$ for charmonia). In general, states above this threshold decay rapidly to $D\bar{D}$ and are not so amenable to study as the bound states.

Name	Quark content	$n^{2S+1}L^J$	Mass(GeV/c^2)	J^{PC}
η_c	$c\bar{c}$	1^1S_0	2.980	0^{+-}
J/ψ	$c\bar{c}$	1^3S_1	3.097	1^{--}
χ_{c0}	$c\bar{c}$	1^3P_0	3.417	0^{++}
χ_{c1}	$c\bar{c}$	1^3P_1	3.510	1^{++}
χ_{c2}	$c\bar{c}$	1^3P_2	3.556	2^{++}
$\eta_c(2S)$	$c\bar{c}$	2^1S_0	3.594	0^{+-}
$\psi(2S)$	$c\bar{c}$	2^3S_1	3.686	1^{--}

Table 2: The charmonium states. The column ($n^{2S+1}L^J$) lists the standard spectroscopic notation of principal quantum number and angular momenta. The column J^{PC} lists the values of spin, parity and charge-parity.

At the J/ψ mass, it is estimated that $\alpha_s(M_{J/\psi}) \approx 0.25$ [8]. These values can be used to estimate the quark velocities in the potential model [9], yielding $v_c^2 \approx 0.3$. The nonrelativistic approximation even if not very accurate for charmonia, is useful nonetheless. The production of heavy quarks in high-energy particle collisions is an active field of

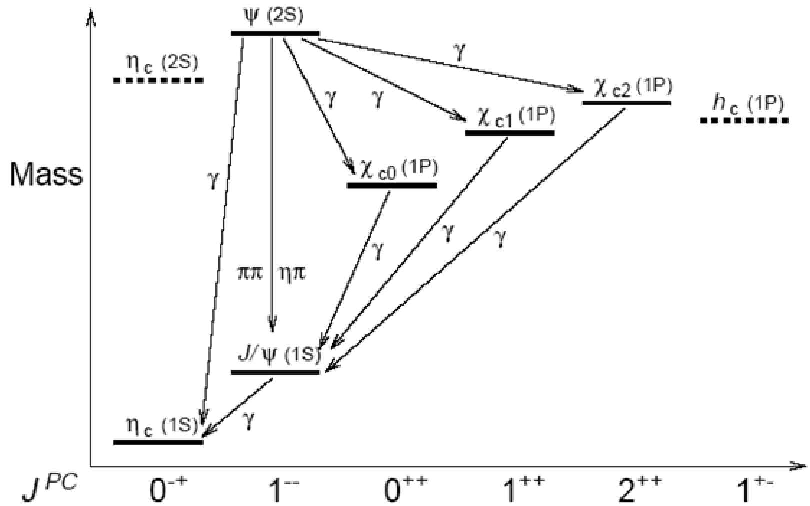

Figure 1: The bound charmonium states. Arrows denote some common transitions between states.

research. Perturbative QCD can be used to make predictions of inclusive heavy flavor production, i.e. charm, bottom and top production [10]. Provided the colliding beam particles have sufficient energy, heavy quarks may be produced in a variety of collisions, for example at $e+e-$, ep and pp colliders. The highest energies are attained in pp collisions, where heavy quark pairs are produced by $q\bar{q}$ and gg interactions between the components of the proton. At high energies, due to asymptotic freedom the incoming hadrons behave approximately as beams of independent quarks and gluons. The momentum distributions of the quarks and gluons within a hadron are characterized by a set of measured parton distribution functions, which depend on the energy scale of the production process. The inclusive heavy quark production cross section thus depends on the parton distribution functions and the amplitudes for $q\bar{q}$ and gg collisions to produce heavy quarks. The study of quarkonium production in high-energy collisions is useful because it involves QCD processes at different energy scales. First, the heavy quark-anti-quark pair is produced in an energetic collision (at distance $r \sim 1/M_{Q^2}$), then the pair binds together into a quarkonium state ($r \sim 1/\alpha_s(M)M$). If the energy scales of these two steps differ sufficiently, the cross section for the production of a quarkonium meson H may factor into two parts First, the cross section for inclusive production of the heavy quark pair $Q\bar{Q}$, which can be calculated perturbatively ($r << 1/\Lambda_{QCD}$), and second is the probability for the $Q\bar{Q}$ pair to evolve into the bound state H, which must be modeled. The technique of separating a production process into two stages is formally known as factorization and is central to QCD calculations of high-energy collisions. The validity of the factorization of the quarkonium production cross section depends on the energy scales and interactions involved in the two steps, and can be tested experimentally.

1.3 Charmonium Production

There are three widely known approaches to describe the evolution of a heavy quark-antiquark pair into a bound state. These approaches, listed below, deal with the probability for a $Q\overline{Q}$ pair produced in a particular color and angular momentum state to form a particular quarkonium meson. If factorization is valid, these probabilities are independent of the $Q\overline{Q}$ production process. For example, charmonium production is studied in several experimental environments including Z_0 decays, B-hadron decays, ep collisions, pp collisions and fixed target hadron experiments. While the perturbative productions cross section is different for each process, the subsequent binding process is the same, provided factorization holds.

1.3.1 The Color Evaporation Model

The Color Evaporation Model (CEM) [11] is a relatively simple model, in which there is no correlation of color and angular momentum quantum numbers between the initial $Q\overline{Q}$ state and the final quarkonium state. It is assumed that soft gluon emission during the binding process alters the quantum numbers to arrive at the appropriate final state. Thus any $c\overline{c}$ pair with invariant mass between $2m_c$ and the open flavor threshold $2m_D$ can form a charmonium state. There is a fixed probability to form each quarkonium state, so the CEM predicts that the ratio of quarkonia cross sections is the same for any production process. However, the actual values are not predicted and must be measured experimentally.

1.3.2 The Color Singlet Model

The Color Singlet Model (CSM) [12] takes the opposite approach, assuming that each quarkonium state can only be produced by a $Q\overline{Q}$ pair in the same color and angular momentum state as that quarkonium. Therefore, a J/ψ meson, for example, can only be derived from a $c\overline{c}$ pair created in a 1^3S_1 color-singlet state. The attractive feature of the CSM is that it makes definite quantitative predictions for production cross sections, because the binding probability is related to the quarkonium wavefunction from the potential model. In the potential model, the amplitude for the quark and anti-quark to overlap, R(0), is related to the quarkonium decay width . For example, $R_{J/\psi}(0)$ can be measured in leptonic J/ψ decays:

$$\Gamma(J/\psi \to l^+l^-) \cong \frac{4\alpha_s^2}{9m^2}\left|R_{J/\psi}(0)\right|^2 \quad (1)$$

The derived value of $\left|R_{J/\psi}(0)\right|^2$ then appears in the CSM formula for inclusive J/ψ production:

$$d\sigma(J/\psi + X) = d\hat{\sigma}(c\bar{c}[1,^3S_1] + X)\left|R_{J/\psi}(0)\right|^2 \quad (2)$$

Here $d\hat{\sigma}(c\bar{c}[1,^3S_1] + X)$ is the inclusive cross section for producing the $c\bar{c}$ in the correct $[1,^3S_1]$ state , which is calculated perturbatively. One of the important predictions of the CSM concerns the differential production cross sections versus transverse momentum in high-energy hadronic collisions. It is a natural quantity to measure at a collider, because high-P_T particles are well separated from the remnants of the colliding beams. Various perturbative processes contribute to the total cross section, two of which are shown in Figure 2. The leading order process in α_s is expected to dominate at lower P_T. It is an example of a 'fusion' process, in which the quarkonium is produced in the collision of two incoming partons. The second main contribution at the lower p_T comes from the subprocess shown in Figure 2(b), where both singlet and octet $c\bar{c}$ states with various quantum numbers contribute to J/ψ production, through $\chi_{cJ} \to J/\psi + \gamma$ decays and/or soft gluon emission. At higher p_T,on the other hand, 'fragmentation' processes (shown in Figure 2(c) and Figure 3) are expected to dominate due to their shallower p_T dependence [9]. Fragmentation refers to the production of a quarkonium meson in the jet produced by a single high p_T particle, as discussed in next section.

1.3.3 The NRQCD Model

The third and more "sophisticated" theoretical approach to quarkonium production is known as the Nonrelativistic QCD (NRQCD) factorization formalism [13]. [2)] NRQCD [14] is an effective field theory [15] ,which treats quarkonium as an approximately nonrelativistic system. NRQCD makes systematic corrections to this approximation using an expansion series in v the velocity of the heavy quark in the quarkonium rest frame. When applied to production, this implies that $Q\bar{Q}$ pairs produced with one set of quantum numbers can evolve into a quarkonium state with different quantum numbers, by emitting low energy gluons. The probabilities of such transitions are suppressed by specific powers of v. This is in contrast to the CSM, in which such transitions have zero probability. The NRQCD factorized cross section for inclusive production of a quarkonium state H has the form:

$$d\sigma(H + X) = \sum_n d\hat{\sigma}(Q\bar{Q}[n] + X)\left\langle O_n^H \right\rangle \quad (3)$$

[2)] Sometimes the phrase "Color Octet Model" (COM) is encountered when color-octet mechanisms are considered. However, the COM lacks the formal organization of energy scales that NRQCD provides.

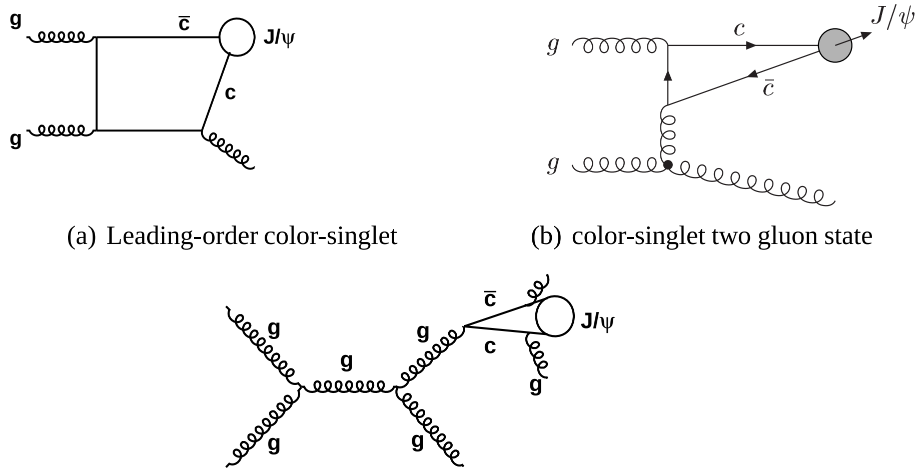

(a) Leading-order color-singlet

(b) color-singlet two gluon state

(c) color-singlet fragmentation

Figure 2: Examples of production in the CSM .The leading order diagram is shown in (a) and occurs at order α_s^3 ; it is a two-gluon fusion process. The large 'blob' vertex represents the nonperturbative binding process; the $c\bar{c}$ pair entering the blob must be in a $[1,^3S_1]$ state. χ_{cJ} production process ,shown in (b), is the second main contribution at the lower p_T region. A color-singlet fragmentation diagram is shown in (c). In all cases, an outgoing gluon balances the transverse momentum of the J/ψ meson.

Here $d\hat{\sigma}$ is the inclusive cross section for producing a $Q\overline{Q}$ pair in the color and angular momentum state n, with small relative velocity [3].

The number $\langle O_n^H \rangle$ is known as the 'matrix element' for the transition of a $Q\overline{Q}$ pair in state [n] to the quarkonium H along with light hadrons whose energies in the rest frame of H are of order $m_Q v_Q^2$ [16]. NRQCD cannot predict the exact values of the matrix elements, but it can estimate their order of magnitude: it predicts that each matrix element is proportional to a specific power of v. The matrix elements are formally defined in NRQCD. They have the form [13],

$$\left\langle O_n^H \right\rangle = \left\langle 0 \left| \chi^\dagger K_n \psi (a_H^\dagger a_H) \psi^\dagger K_n' \chi \right| 0 \right\rangle \tag{4}$$

where ψ and χ are Pauli spinor operators which destroy heavy quarks and create heavy anti-quarks respectively. The operator a_H creates the quarkonium [4] along with light

[3] In calculating $d\hat{\sigma}$, the relative velocity of the quark and antiquark is restricted to sufficiently small values, of order v or less, that they will not move apart and hadronize separately.

[4] Note that a_H as written here implies a sum over helicity states, which must instead be separated when considering polarization.

hadrons. The factor K_n contains color and spin matrices and covariant derivatives, depending on the quantum numbers in n. Equation 4 is therefore describing a projection of a $Q\overline{Q}$ pair onto a quarkonium state. Although there are an unlimited number of matrix elements with various values of n, in practice only those at lowest order in v are considered. This can be illustrated by the expansion in powers of v of the J/ψ meson state:

$$|J/\psi\rangle = O(1)\left|c\bar{c}[1,^3S_1]\right\rangle + O(v)\left|c\bar{c}[8,^3P_J]g\right\rangle + O(v^2)\left|c\bar{c}[8,^3S_1]g\right\rangle + \\ + O(v^2)\left|c\bar{c}[(1,8),^3S_1]gg\right\rangle + O(v^2)\left|c\bar{c}[(1,8),^3D_J]gg\right\rangle + \dots \quad (5)$$

The velocity scaling of a particular matrix element depends on the scaling of the related term in this expansion. Only those matrix elements at small powers of v are included in the calculations. The leading order (in v) matrix element for J/ψ production is $\left\langle O_1^{J/\psi}(^3S_1)\right\rangle$, which corresponds to the CSM case: the $c\bar{c}$ pair is produced in a $[1,^3S_1]$ state. In NRQCD this matrix element is of order v_c^3, and its value can be measured from the J/ψ leptonic decay width, in analogy with Equation 5. The next matrix elements involve color octet initial states and occur at order v_c^7; they are $\left\langle O_8^{J/\psi}(^3P_J)\right\rangle$, $\left\langle O_8^{J/\psi}(^1S_0)\right\rangle$ and $\left\langle O_8^{J/\psi}(^3S_1)\right\rangle$. Their values have been fitted from production cross sections in pp collisions, as have analogous matrix elements for other quarkonia [17], [18], [19], [20]. The short-distance cross section $d\tilde{\sigma}$ associated with each matrix element has a certain P_T dependence, so the matrix elements can be fitted to the observed P_T spectrum. The matrix elements $\left\langle O_8^{J/\psi}(^3P_J)\right\rangle$ and $\left\langle O_8^{J/\psi}(^1S_0)\right\rangle$ cannot be separately determined because their cross sections have the same P_T dependence, so their weighted sum is fitted. NRQCD spin symmetry relations, in this case :

$$\left\langle O_8^{J/\psi}(^3P_J)\right\rangle = (2J+1)\left\langle O_8^{J/\psi}(^3P_0)\right\rangle \quad (6)$$

are used to reduce the number of free parameters in the fits [21]. If the above formalism is valid, then any J/ψ production process should yield the same fitted values for the matrix elements [5)]. This universality may however be limited in certain regions of phase space [22] and by the details of the soft gluon emission process [23]. The attempt to understand quarkonium production in all types of experimental environments in the NRQCD framework is an ongoing one. In high-energy pp collisions, there are three distinct types of charmonium production. The first is the type discussed above, in which the meson is produced in the collision of the two protons. This is called direct production. The second is in the decay of heavier charmonia, for example the production of a J/ψ meson in the decay of a χ_c or $\psi(2S)$ meson, and is known as feeddown. The third, B-decay, is in the weak decay of b-flavored hadrons: B^+, B^0, B^0_S, Λ_b and their antiparticles. This third type is distinguished from the first two by the relatively long lifetime

[5)] NRQCD can also be applied to quarkonium decays, with different but related matrix elements [13] of B-hadrons, about 2 ps. The decay vertex of a B-hadron is usually far enough from the primary pp interaction point to be identified as a displaced secondary vertex [6)]. The first two types of charmonium production occur at the primary interaction point and are collectively known as prompt production. At high P_T ($P_T \gg mc$) the dominant process in NRQCD is the fragmentation of a single gluon to a $c\bar{c}$ pair in a $[8,^3S_1]$ state [24]. This process is illustrated in Figure 3. In comparison to the color singlet fragmentation process in Figure 2(c), this occurs at a higher order of v_c (v_c^7 versus v_c^3) but at a lower order of α_s (α_s^3 versus α_s^5). Thus it is indeed plausible that the color octet process could explain the Tevatron observed direct cross sections (detailed in the following section).

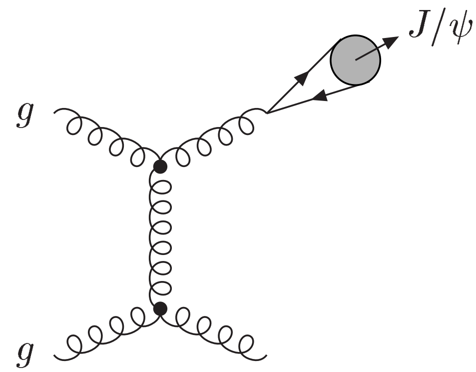

Figure 3: Schematic diagram of gluon fragmentation to a $c\bar{c}[8,^3S_1]$ pair, followed by binding (the blob) into a meson. Light hadrons with low energies may also be emitted during the binding but are not shown. The fragmenting gluon could also be produced by other perturbative QCD processes.

1.3.4 k_T factorization

At the energies of modern colliders, the interaction dynamics is governed by the properties of parton distributions in the small x region. This domain is characterized by the double inequality $s \gg \mu^2 \simeq \hat{s} \gg \Lambda^2$, which shows that the typical parton interaction scale μ (of the order of the subprocess invariant energy $\sqrt{\hat{s}}$) is much higher than the QCD parameter Λ, but is much lower than the total c.m. system energy $\sqrt{s}$. The situation is therefore classified as "semihard". In such a case, the perturbation expansion in α_s may contain large coefficients $O[ln(s/\mu^2)] = O[ln(1/x)]$ which compensate the smallness of the coupling constant $\alpha_s(\mu^2/\Lambda^2)$. The resummation ([25] [26] [27] [28]) of the terms $[ln(\mu^2/\Lambda^2)\alpha_s]^n$, $[ln(\mu^2/\Lambda^2)ln(1/x)\alpha_s]^n$, and $[ln(1/x)\alpha_s]^n$ results in the so

[6)] A sequential decay such as $B \to \chi_c \to J/\psi$ is classified as B-decay, not feeddown, because it occurs at a displaced vertex called noncollinear or unintegrated parton distributions $F_i(x,k_T^2,\mu^2)$, which determine the probability of finding a parton of type i carrying the longitudinal momentum fraction x and transverse momentum k_T at the probing scale μ^2. These k_T-dependent distributions generalize the factorization of the hadronic matrix elements beyond the collinear approximation. Hereafter this generalized factorization will be referred to as "k_T factorization". The unintegrated parton distributions obey certain evolution equations [e.g., Balitski- Fadin-Kuraev-Lipatov (BFKL) [29] or Ciafaloni, Catani, Fiorani,Marchesini (CCFM) [30] and reduce to conventional Dokshitzer-Gribov-Lipatov-Altarelli-Parisi (DGLAP) [31] densities once the k_T dependence is integrated out. Nowadays, the significance of the k_T-factorization (semihard) approach is becoming more and more commonly recognized [32] [35]. Remarkable agreement is found between the data and the theoretical calculations regarding the photo- and electroproduction [38] of D* mesons and forward jets [39], as well as for specific kinematic correlations observed in the associated D*+jets photoproduction [40] at the DESY ep collider HERA. The semihard approach was also shown to reasonably describe the data on the hadroproduction of beauty [41] [42], J/ψ[[43], and χ_c mesons [44] at the Fermilab Tevatron. The theoretical predictions made in [45] have triggered dedicated experimental analyses [46] [47] of the J/ψ polarization (i.e., spin alignment) at HERA conditions. In the framework of the CSM (as discribed before), the production of any heavy meson is described as the perturbative production of a color-singlet $Q\bar{Q}$ pair with the quantum numbers of the quarkonium state under consideration. The corresponding Feynman diagrams are shown in Figure 4 (a) (assuming also five possible permutations of the incoming and outgoing gluons!. The formation of a meson from the quark pair is a nonperturbative process. Within the NRQCD approximation which we are using, this probability reduces to a single parameter related to the meson wave function at the origin $|R(0)|^2$, which is known for the J/ψ from the measured leptonic decaywidths. In addition to the above, we consider the color-octet production scheme [48], which implies that the heavy $Q\bar{Q}$ pair is perturbatively created in a hard subprocess as an octet color state and subsequently evolves into a physical quarkonium state via emitting soft (nonperturbative) gluons, which may be interpreted as a series of "classical" color-dipole transitions. Although these transition probabilities can, in principle, be expressed in terms of field operators and therefore calculated, no such calculation exists to date. Thus, the transition probabilities remain free parameters, which are assumed to obey a definite hierarchy in powers of v, the relative velocity of the quarks in the bound system under study. This freedom is commonly used to estimate the color-octet parameters by adjusting them to experimental data. In the case when the color-octet $Q\bar{Q}$ state is allowed, there appear additional contributions due to the diagrams shown in Figures 4 (b,c,d). The complete gauge invariant set comprises six diagrams of the type "a", six diagrams of the type "b", four diagrams of the type "c", and one diagram "d". The nonperturbative transition matrix elements mentioned here (usually denoted in the literature as $\langle 0|Ø_8|0\rangle$) are related

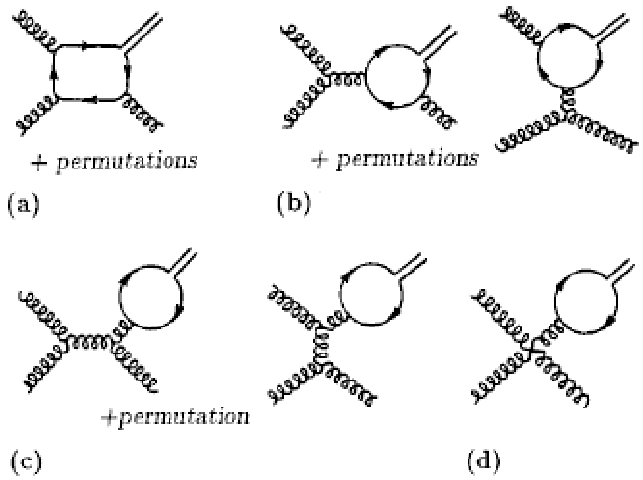

Figure 4: Feynman diagrams representing the gluon-gluon fusion mechanism in the color-singlet and color-octet models. Only the perturbative skeleton of the process is presented; the soft gluons corresponding to the nonperturbative color-octet transitions are not shown.

to the fictitious color-octet wave functions, which are used in calculations in place of the ordinary color-singlet wave functions:

$$\langle 0\,|\varnothing_8|\,0\rangle = \frac{9}{2\pi}\,|R_8(0)|^2 = \frac{9}{2\pi}4\pi\,|\Psi_8(0)|^2 \tag{7}$$

This equation applies to all S-wave color-octet states, and a similar relation holds for $R_8(0)$ and $\Psi_8(0)$ if the P-wave color-octet states are involved. A generalization of the above formalism to the k_T-factorization approach implies two important steps. These are the introduction of noncollinear gluon distributions and the modification of the gluon spin density matrix in the parton level matrix elements. k_T-factorization approach is now at the stage of development, however it claims to solve (explain) the problem of missing J/ψ transverse polarization.

1.3.5 Charmonium measurements

Quarkonium production was originally described in CSM model. This approach had the benefit that all non-perturbative aspects could be absorbed into the wave function of the quarkonium state. This model enjoyed some success before CDF measured an excess of direct J/ψ production [50] more than an order of magnitude greater than that predicted by the CSM (see Figure 5).

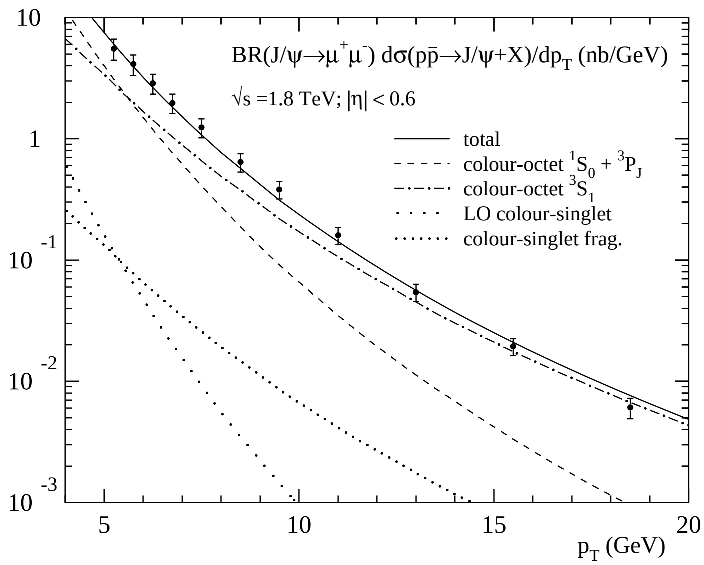

Figure 5: Differential cross-section of J/ψ production at CDF with theoretical predictions for color-singlet and color-octet model production [51].

The Color Octet Model (COM) [52] was proposed as a solution to the theory prediction mismatching. COM provides a solution to the infrared divergences that were present in the production cross-sections of P-wave states in CSM [53], by incorporating the description of the problematical soft gluon emission into the non-perturbative color-octet parameter.

NRQCD factorisation approach isolates non-perturbative physics from the perturbative hard process and parametrises the former in a long-distance matrix element. The latter represents a free parameter in the theory and requires an experimental fit to data. However, the universality of these matrix elements means that their values can be extracted independently from a number of different processes including photoproduction [54] and Deep Inelastic Scattering [55].

Hence the good description of the Tevatron data by the COM shown in Figure 5 is, at least in part, due to the fact that the values of some parameters were determined from the same data. Tests of other COM predictions have not been so successful: Figure 6 shows the polarisation coefficient in $J/\psi \rightarrow \mu\mu$ decay as a function of its transverse momentum, where the COM prediction is very different from the data.

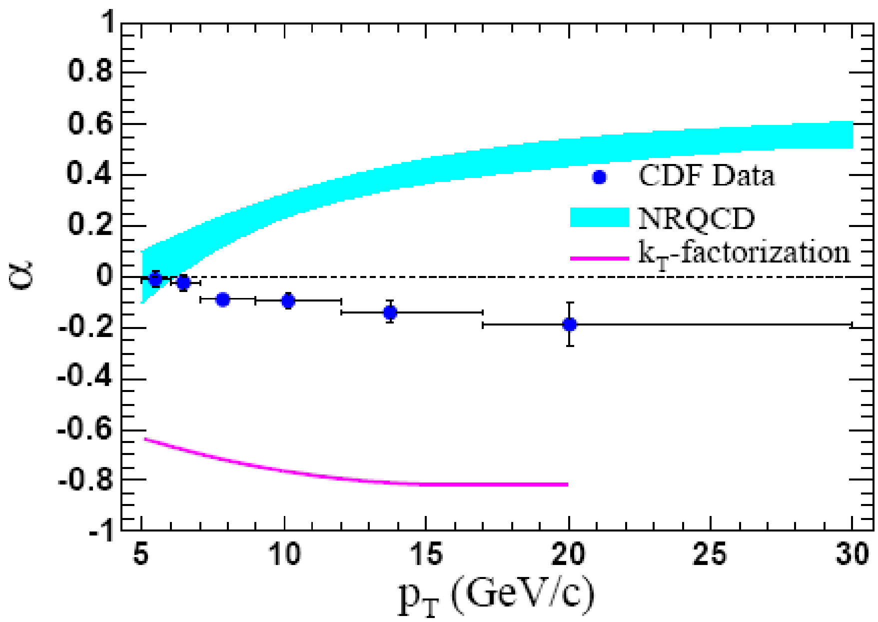

Figure 6: Polarisations of J/ψ production as a function of p_T at CDF, (blue circles) , curves for limit cases of the k_T factorisation model, and a band for NRQCD predictions (from [56]).

The model based on k_T factorisation in QCD showers claims to be able to describe both the lack of transverse polarisation in J/ψ decays and the high cross section of J/ψ

production. Another model [57] argues that the deficit in the cross section as predicted by CSM can be largely explained by the production of a quarkonium state in association with an additional heavy quark, and also predicts lower levels of polarisation. This thesis shows that ATLAS is capable of detailed checks of the predictions of these and other models by measuring not only p_T and η distributions of onium states in a wide range of these variables, but also the degree of polarisation, associated hadronic activity, and the production of C-even states. In the absence of a comprehensive Monte Carlo generator capable of simulating all aspects of all theoretical models, we use the PYTHIA 6.403 [58] generator incorporating the COM Mechanism, with model parameters fixed through a combination of theoretical and experimental constraints [59](for details see Appendix A.1). Inevitably, this simulation is unable to reproduce adequately some features of the data, notably the polarisation angle distributions and hadronic accompaniment of the quarkonium states. However, the simulated samples should be enough to study the acceptance and efficiency of ATLAS to detect all required particles and measure their parameters across the whole range of the phase space. The polarization of the sample introduced into the analysis code by building the angular distribution according the weighted normalization of events. This subject is discussed in Section 5. While current theoretical predictions of the absolute value are rather uncertain, it is expected that it will be about a factor of five higher than the one obtainable at the Tevatron, running at $\sqrt{s} \sim 2TeV$. Therefore, this kind of physical analysis has good opportunity to study the QCD processes and may be to measure signals of the new physics.

1.3.6 Dissertation Overview

This dissertation describes the measurement of the polarization of J/ψ mesons produced in pp collisions at a centre-of-mass energy of 14 TeV. The collisions will be produced by the Large Hadron proton-proton collider (LHC), located at European Organization for Nuclear Research in Geneva, Switzerland. The collision data will by colected by the ATLAS Collider Detector , which is one of the two biggest detectors constructed at the LHC.

Chapter 2 describes ATLAS and the LHC in detail.

Chapter 3 describes the ATLAS trigger and ATLAS trigger scheme that will be used for quarkonium selection.

Chapter 4 describes the direct J/ψ events selection, performance of background suppression, separation of direct and indirect J/ψ events, analysis of χ_c production and its rejection procedure.

In Chapter 5 the details of the polarization analysis are described. The angular distribution of the muons in the J/ψ decays is used to measure the polarization. Furthermore, the polarization of promptly produced J/ψ mesons is separated from the polarization of those produced in B-hadron decays, using measured J/ψ decay time.

Chapter 6 presents the study of various systematical errors, and estimate their impact on

the direct J/ψ polarization measurements.
Chapter 7 summarizes the analysis.
Appendix A.1 contains a study of heavy quarkonium generation in PYTHIA particle generator, implementation of color-octet processes in PYTHIA, new showering model description and its implementation. It covers also discussion on PYTHIA dependence on parton distribution functions (PDF).

2 ATLAS experiment in the Large Hadron Collider

The LHC [60] is a pp collider that will operate at the highest center of mass energies ever achieved. It is currently under construction at CERN in the former LEP tunnel and will become operational in September 2008. The LHC will be the first collider to allow the study of physics in the TeV range. Theoretical predictions hint at a rich field of new physics. The main goals of the LHC include studies of the Standard Model, the discovery of the Higgs boson and searches for new physics beyond the Standard Model like SUSY and extra dimensions. Six experiments are under construction along the LHC tunnel: Two multi purpose detectors ATLAS and CMS are designed to explore the full field of physics offered at the LHC. In addition, four dedicated experiments are being constructed. ALICE is designed to study the physics of strongly interacting matter, in particular the quarkgluon plasma, by means of Pb-Pb collisions. LHCb is a B-physics experiment that will study CP-violation in the B-system. The aim of TOTEM is to measure the total pp cross section and to study elastic scattering. Finally LHCF will study the energy distributions of particles emitted almost parallel to the beam direction.

2.1 The Large Hadron Collider

Figure 7 shows a schematic overview of CERNs accelerator complex located at the Swiss-French border near Geneva. The acceleration is performed in several stages. The protons are accelerated using a linear accelerator and the Proton Synchrotron (PS) after which they are injected into the Super Proton Synchrotron (SPS). Here the energy of the protons is increased up to 450 GeV before they are injected into the LHC. In the LHC ring, build in the former 26.7 km circumference LEP tunnel, the acceleration continues until the protons reach their final energy of 7 TeV. The two proton beams will collide at four interaction points along the LHC beam line with a nominal center of mass energy of 14 TeV. The beams will be structured in 2808 bunches, 10^{11} protons each; the time interval between successive bunches is 25 ns i.e. 40,000,000 bunch-bunch collisions per second. At the beginning the LHC collider will start with low luminosity run ($10^{33} cm^{-2}s^{-1}$). After one year run with low luminosity, it is planed to upgrade the collider to the highest possible luminosities $10^{34} cm^{-2}s^{-1}$. The production cross-section for $c\bar{c}$ pairs will be very high (about $2 \times 10^{-2} \mu b$).

2.2 Experimental challenges at the LHC

Figure 8 shows the pp cross sections as a function of the center of mass energy for several physics processes. Indicated on the right side of the figure is the event rate assuming an instantaneous luminosity of $0.01 pb^{-1}s^{-1}$. The vertical line indicates the center of mass energy of the LHC. At this energy the total pp cross section is in the order of 10^8 nb, which corresponds to an interaction rate of 10^9 events per second. Furthermore the

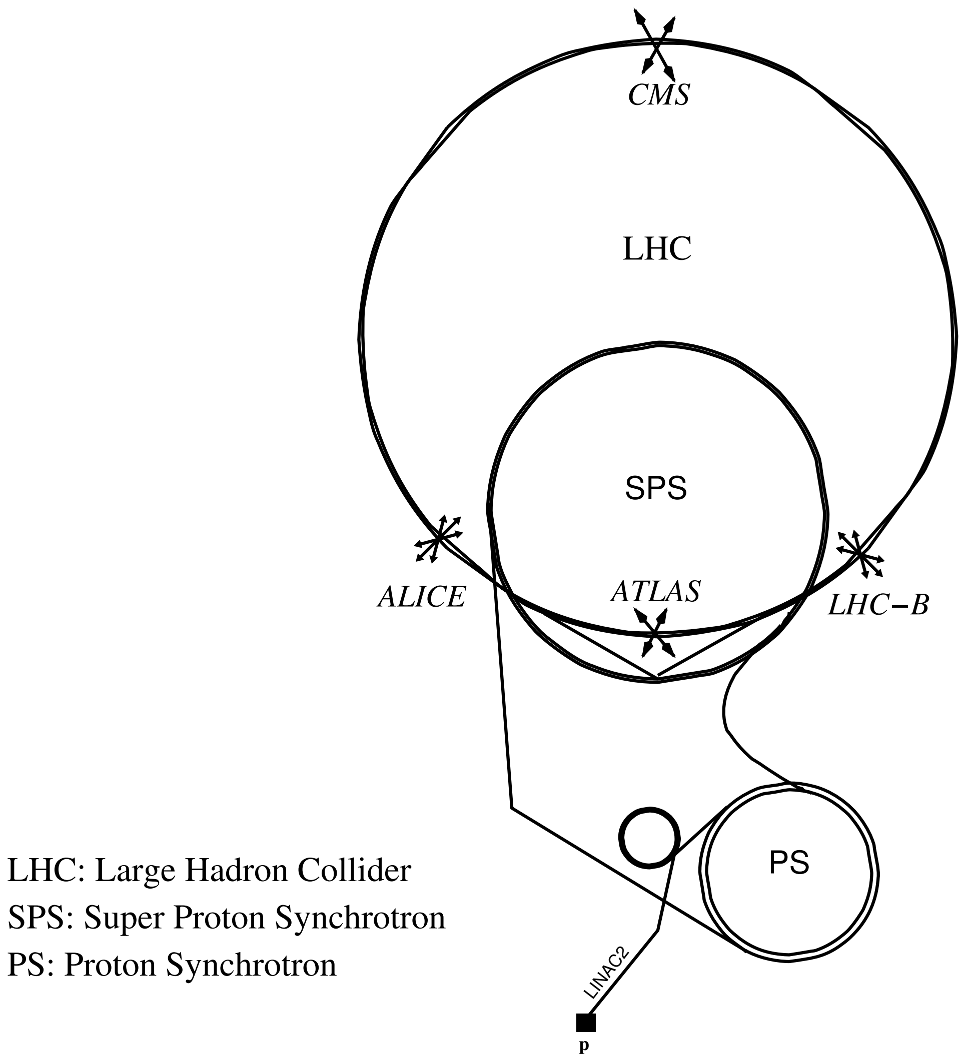

Figure 7: Overview of the accelerator complex at CERN.

QCD cross sections are orders of magnitude larger than the cross sections of processes such as the production of top quarks, W and Z bosons and Higgs bosons. For example the production cross section for Z bosons is one million times smaller than the total pp cross section, meaning that on average only during one out of a million collisions a Z boson is created. This ratio is another two orders of magnitude smaller for the production of Higgs bosons. Identifying these rare events in the vast amount of collisions is one of the main experimental challenges to be faced at the LHC.

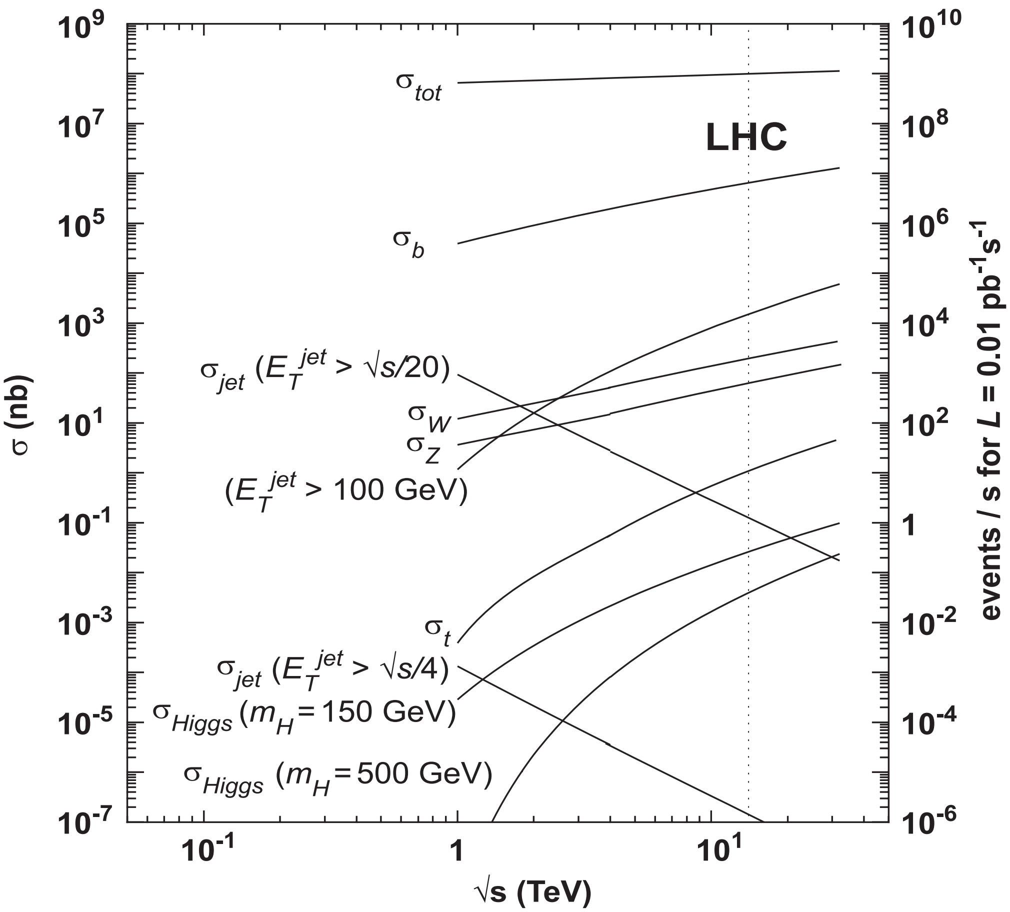

Figure 8: Proton-proton cross sections as a function of the center-of-mass energy.

2.3 ATLAS experiment

The ATLAS detector [61] is now towards the end of its construction phase and is scheduled to be operational by September 2008. It consists of a series of ever-larger concentric cylinders around the interaction point where the proton beams from the LHC collide. It can be divided into four major parts: the Inner Detector, the calorimeters, the muon spectrometer and the magnet systems. Each of these is in turn made of multiple layers. The detectors are complementary: the Inner Detector tracks charged particles precisely, the calorimeters measure the energy of easily stopped particles, and the muon system makes additional measurements of highly penetrating muons. The two magnet systems bend charged particles in the Inner Detector and the muon spectrometer, allowing their momenta to be measured.

The design criteria of the ATLAS detector include: [61]

- Efficient tracking at high luminosity for high-p_T lepton-momentum measurements, electron and photon identification, τ-lepton and heavy-flavour identification, and full event reconstruction capability at lower luminosity;
- Very good electromagnetic calorimetry for electron and photon identification and measurements, complemented by full-coverage hadronic calorimetry for accurate jet and missing transverse energy (E_T^{miss}) measurements;
- High-precision muon momentum measurements, with the capability to guarantee accurate measurements at the highest luminosity using the external muon spectrometer alone;
- Large acceptance in pseudorapidity $\eta = -ln(tan(\theta/2))$ with almost full azimuthal angle ϕ coverage everywhere. The azimuthal angle is measured around the beam axis, whereas pseudorapidity relates to the polar angle θ where θ is the angle from the z direction (the direction of the beam line).
- Triggering and measurements of particles at low-p_T thresholds, providing (see Figure 8) high efficiencies for most physics processes of interest at LHC.

The overall detector layout is shown in Figures 9.

2.4 The Inner Detector

The inner detector was designed to reconstruct the trajectories of charged particles in the high density environment at the LHC. The interaction rate of 40 MHz requires a very fast detector with a time window smaller than 25 ns to reduce the number of tracks seen by the detector coming from earlier bunch-bunch crossings. Furthermore high granularity is needed to separate the large number of tracks. The choice was made to

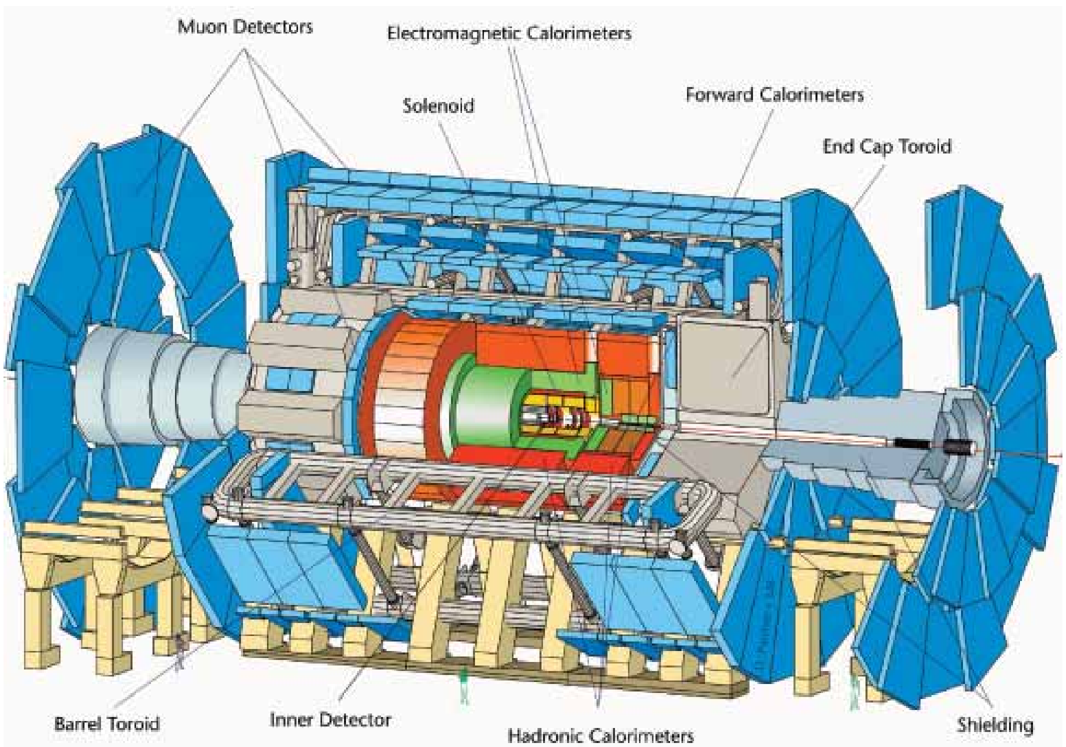

Figure 9: Schematic view of the ATLAS detector. Overall dimensions are roughly 45m long and 25m in diameter (and only 7000 T).

use three different detector technologies. In Figures 10 a three dimensional view of the inner detector [62] is shown. The inner most layers of the detector closest to the interaction point comprises the silicon pixel detector. The pixel detector is surrounded by the Semi-Conducting Tracking (SCT) detector which consists of silicon strip detectors. The outer layers of the inner detector are formed by the Transition Radiation Tracking (TRT) detector which is made of multiple layers of drift straws. The complete system is contained in a 2 Tesla solenoidal magnet. A particle originating from the interaction point crosses at least three pixel layers, four SCT strip layers and a large number (typically 36) of TRT straws, allowing a precise measurement of the momentum of the particle. As seen in the following sections while tracking is crucial for the polarization measurements the impact parameters plays important role in the event selection.

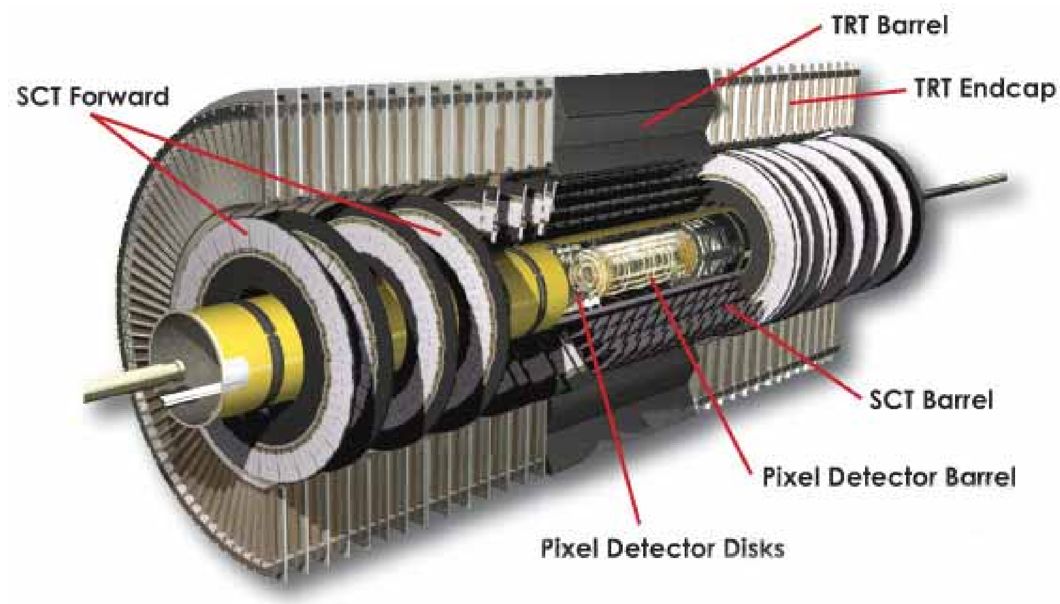

Figure 10: Schematic view of the ATLAS Inner Detector.

The Figure 11 shows (a) the momentum resolution typically achieved with the inner detector that is $\Delta p_T/p_T = 0.04\% \times p_T \otimes 2\%$ (p_T in GeV) and (b) an impact parameter resolution of 15 μm in the transverse plane .

The pixel detector is situated directly around the beam pipe. It has three layers of which the first pixel layer is positioned at a radius of 4 cm. The total system has 80 million pixels, each 50 μm in the $r\phi$ direction and 400 μm along the z-axis. The three measurements per track determine the impact parameter resolution and are vital for the pattern recognition in the inner detector. The barrel SCT consists of four double layers of silicon strip detectors with a strip pitch of 80 μm providing four accurate

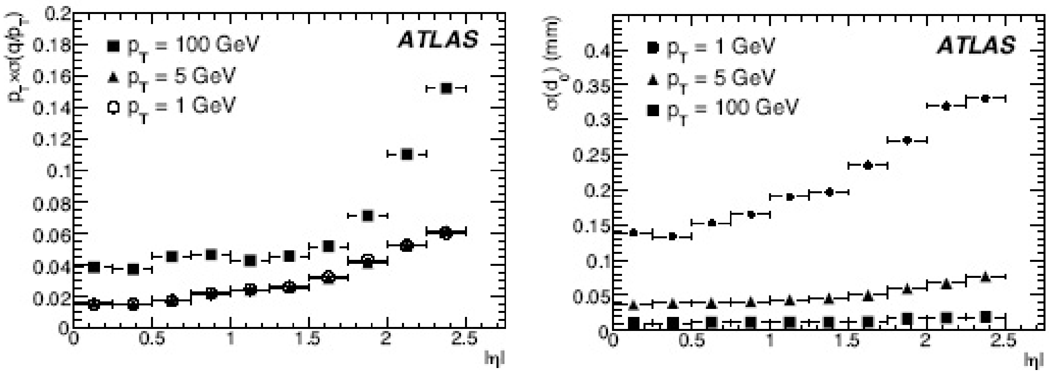

(a) Transverse momentum resolution (b) Impact parameter resolution

Figure 11: ID resolution in the transverse momentum p_T and impact parameter D0 measurement versus pseudorapidity.

measurements in the $r\phi$ plane. A small stereo angle between the strips in different layers is used to obtain a measurement of the z position. The SCT end-caps both contain nine disks equipped with double layers of silicon strip detectors. The strips are pointing towards the beam axis providing a measurement in the $r\phi$ plane. A small stereo angle between the strips in different layers makes it possible to measure the radial position of the hit. The TRT was designed to provide a relatively large number of space point measurements at low cost. This is achieved by using drift straws with a diameter of 4 mm and a maximum length of 150 cm. In the barrel the straws are oriented parallel to the beam axis providing a measurement in the bending plane of the magnet. Following the design of the SCT, the straws in the end-caps are pointing towards the beam axis. The TRT can also detect transition radiation occurring when a relativistic particle crosses the boundary between two media with different electrical properties. The number of transition radiation hits is a measure for the velocity of a particle. This allows the separation of electrons and pions, and to a lesser extent the separation of kaons and pions.

2.5 The Calorimeters

The ATLAS calorimetry [63] consists of an electromagnetic calorimeter (ECAL) and a hadronic calorimeter (HCAL) (see Figures 12). The very forward region is covered by a dedicated radiation hard calorimeter with courser granularity. The electromagnetic calorimeter is a sampling calorimeter which uses lead as absorber and liquid argon as sampling material. It covers the rapidity range up to $|\eta| < 3.2$

Its accordion geometry provides a complete η coverage without azimuthal cracks. The ionization charge is collected on copper clad Kapton electrodes. The segmentation

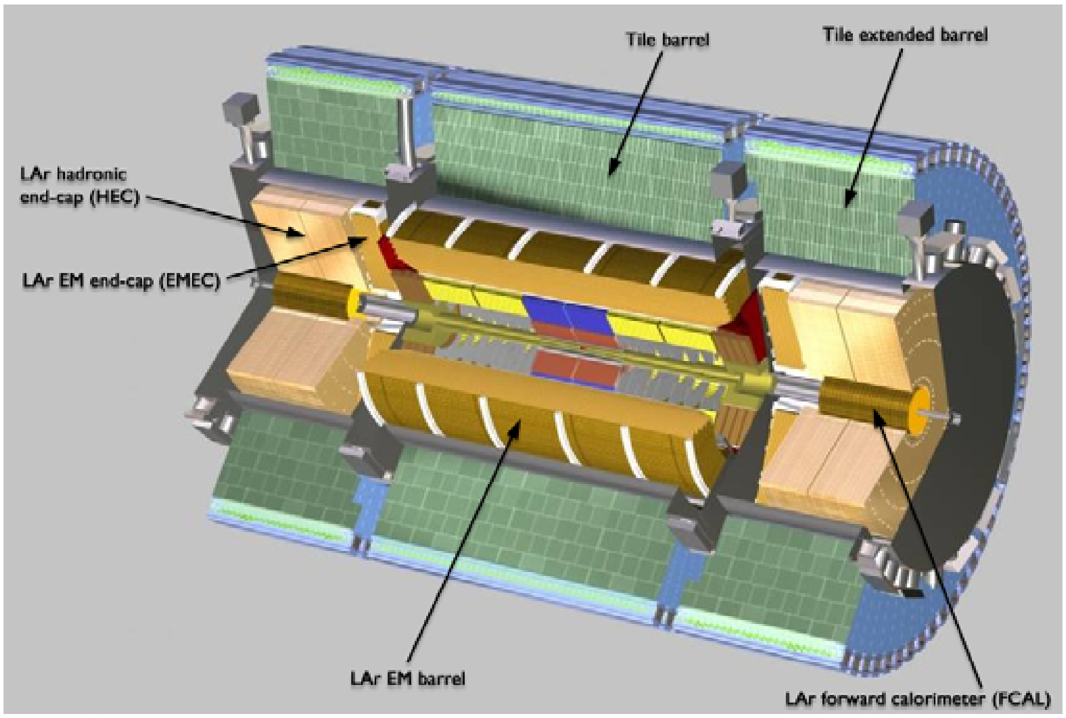

Figure 12: Schematic view of the ATLAS Electromagnetic and Hadronic Calorimeters

of the calorimeter varies from $\Delta\eta = 0.003 - 0.1$ and $\Delta\phi = 0.025 - 0.1$. In the region up to $|\eta| = 2.5$ the calorimeter provides three longitudinal sections whereas only two are available for larger rapidities. The total thickness of the electromagnetic calorimeter is more than 24 radiation lengths [7)] in the barrel and more than 26 radiation lengths in the end-cap. The typically achieved energy resolution is $\Delta E/E = 11.5\%/\sqrt{E} \otimes 0.5\%$ (E in GeV), the resolution on the polar direction of a shower is $\Delta\theta = 50\ mrad/\sqrt{E}$ (E in GeV). The hadronic calorimeter is divided into three sub detectors. The barrel calorimeter, $|\eta| < 1.6$, is a sampling calorimeter which uses iron absorber tiles interleaved with scintillators. The tiles are placed perpendicular to the colliding beams and are staggered in depth. The resulting granularity of the detector is $\Delta\eta \times \Delta\phi = 0.1 \times 0.1$. It has a longitudinal segmentation of three samplings. The total thickness of 11 interaction lengths at $\eta = 0$ has been shown to be sufficient to reduce punch-through well below the irreducible level of prompt or decaying muons. The hadronic liquid argon end-cap calorimeter covers the range $1.5 < |\eta| < 3.2$. It has a $\Delta\eta \times \Delta\phi = 0.1 \times 0.1$ segmentation in the range of $|\eta| < 2.5$ and a segmentation of $\Delta\eta \times \Delta\phi = 0.2 \times 0.2$ in the range up to $2.5 < |\eta| < 3.2$. Over the full η range four longitudinal samples are available. The average jet energy resolution is $\Delta E/E = 50\%/\sqrt{E} \otimes 3\%$ (E in GeV). The forward calorimeter, $3.1 < |\eta| < 4.9$, consists of three sections. The first is made out of copper while the others are made out of tungsten. Each section uses a matrix of longitudinal channels containing thin gaps filled with liquid argon.

2.6 The Muon Spectrometer system

The muon spectrometer [64] covers the outer most layers of the ATLAS detector and occupies by far the largest volume. It was designed to serve two purposes: an independent muon trigger and high quality stand-alone muon reconstruction over a wide range in transverse momentum, pseudo-rapidity and azimuthal angle. This is achieved by the use of a large toroidal magnet system together with trigger and high precision tracking chambers. The magnet system of the muon spectrometer consists of three air-core toroids. The barrel toroid extends over a length of 25 m with an inner radius of 4.7 m and an outer radius of 10 m. The two end-cap toroids are inserted into the barrel toroid. These have a length of 5 m, an inner bore of 1.65 m and an outer diameter of 10.7 m. Each toroid is build up of eight super conducting coils assembled in a radial configuration. Due to the finite number of coils, the field is not perfectly toroidal but shows a regular eight fold pattern as can be seen in Figure 13(a). The deviations are most profound in the transition region between barrel and end-cap. The magnets provide an average bending power of 3 Tm in the barrel and 6 Tm in the end-cap as is shown in Figure 13(b). Accurate knowledge of the field is required in order not to degrade the

[7)] The radiation length is defined as the distance over which a high-energy electron on average loses all but $1/e$ of its energy momentum resolution. During ATLAS running a large number of magnetic field sensors will measure the local field ensuring a knowledge of the bending power with a precision better than 0.3%.

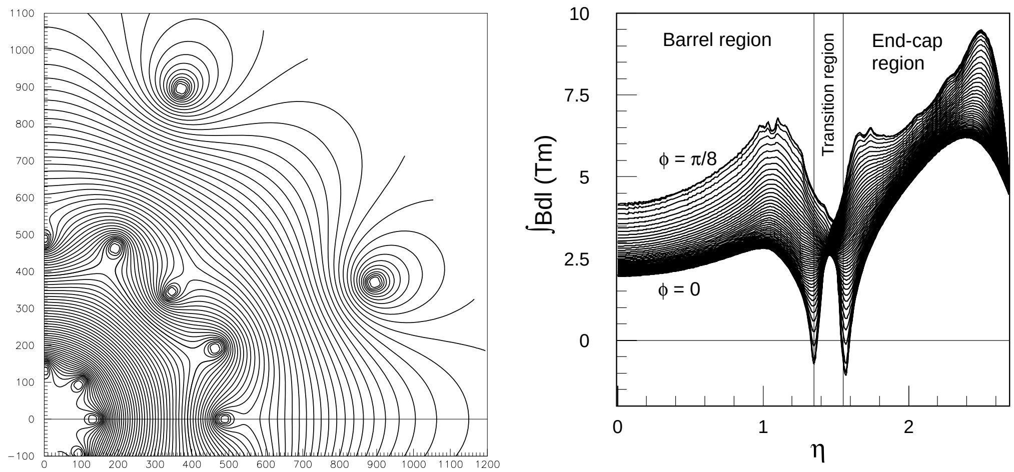

(a) Magnetic field map (b) Toroid bending power

Figure 13: (a) Magnetic field map in the transition region between barrel and end-cap. The field lines in the transverse plane are shown. The coordinate system of the magnetic field is rotated by $\frac{\pi}{8}$ with respect to the ATLAS coordinate system. (b) Toroid bending power $\int Bdl$ of the azimuthal field component, integrated between the inner and outer muon station as a function of the pseudo-rapidity.

Figure 14 shows the transverse view of the barrel part of the muon spectrometer. In the barrel a particle typically traverses three measurement planes. The inner most stations are situated directly after the hadronic calorimeter, just outside the toroidal magnetic field. They are equipped with Monitor Drift Tube (MDT) chambers which allow a high precision measurement of the muon trajectory. The second layer of stations is situated in the magnet. The stations in this layer consist of a combination of one MDT chamber and two Resistive Plate Chambers (RPC). A third layer of stations is located just outside the magnetic field. The outer stations are formed by a combination of a MDT chamber and a RPC. The design of the muon system in the end-caps is different as it is not possible to install stations inside the end-cap magnets and the background rate is much higher. In the end-cap (Figure 15), the first layer of stations sits in front of the magnet. The region closest to the beam pipe, where the background counting rates are highest, is equipped with Cathode Strip Chambers (CSC) instead of MDT chambers because of their higher rate capability. MDT chambers provide the remaining coverage. Thin Gap Chambers (TGC) are installed providing the trigger signal. The second station layer is installed behind the end-cap magnet and is equipped with one layer of MDT chambers and two layers of TGCs. The outer station layer is equipped with MDT chambers.

2.6.1 The Muon Instrumentation

The barrel and most of the end-cap region are equipped with MDT chambers for the precision measurement of muon trajectories. A MDT is an aluminum tube with a diameter of 30 mm with a 50 μm diameter central tungsten wire. A single tube measures the hit distance to the wire with a typical average resolution of 80 μm. The position along the tube cannot be measured and has to be provided by an external measurement. It can either be provided using the information from the trigger chambers or by extrapolation of tracks from the inner detector into the muon system. A full MDT chamber consists of two multi-layers of tubes separated by a support structure. For chambers situated in the middle and outer part of the spectrometer each multi-layer consists of three layers of tubes, the chambers closest to the interaction point are equipped with four layers per multi-layer. Depending on the location of the chamber the number of tubes per layer varies from 30 up to 72 tubes. The length of the tubes also varies between: 1.6 m and 6.2 m. In comparison to the other techniques describes in this section, the MDT chambers utilize completely different concepts developed to obtain a technology which is cheep and which can cover a large area. This detection technology is specialized in an accurate position measurement of a muon track in the direction of its deflection caused by the externally applied magnetic field. The need to cover a large area requires the use of long tubes. However, it was found that, in practice, no support structure exist to keep the tubes rigid enough. The simplest solution to this problem was to allow the chamber sag due to gravity, but to give the wire such a tension that it has an equal sag. Because of deviations to the chamber geometry which are caused by air flow, temperature differences, vibrations, and other external influences, the necessity arises to continuously monitor the chamber. It is floppy by nature and the deviations are accurately registered in order to guarantee a high precision position measurement.

The inner layer of the end-cap of the spectrometer, $2 < |\eta| < 2.7$, is equipped with CSCs. The CSCs are multi-wire proportional chambers with a cathode strip readout and with a symmetric cell in which the anode-cathode spacing is equal to the anode wire pitch. The precision coordinate is obtained by measuring the charge induced on the segmented cathode by the avalanche formed on the anode wire. The small electron drift time of less than 30 ns and the high spatial resolution $\Delta r \approx 50 \mu m$ allow them to operate in the high background environment of the forward region. The trigger chambers of the ATLAS muon spectrometer serve a threefold purpose:

- A momentum dependent muon trigger;
- Bunch crossing identification;

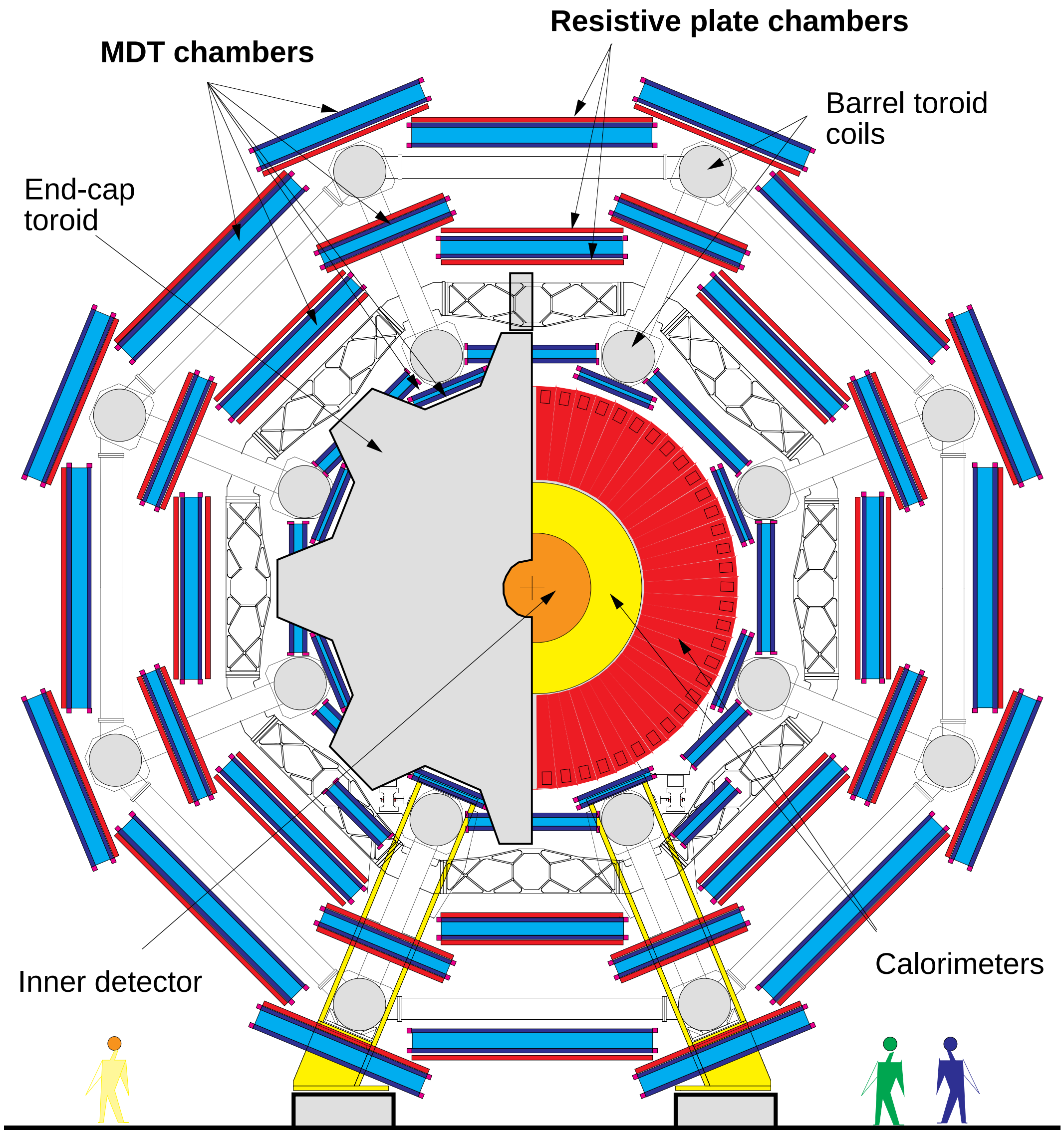

Figure 14: Transverse xy-view of the ATLAS muon detector.

- Measurement of the second coordinate along the tube in the MDT chambers.

Two technologies are deployed in the spectrometer. The barrel region is equipped with RPCs; The end-caps with TGCs.

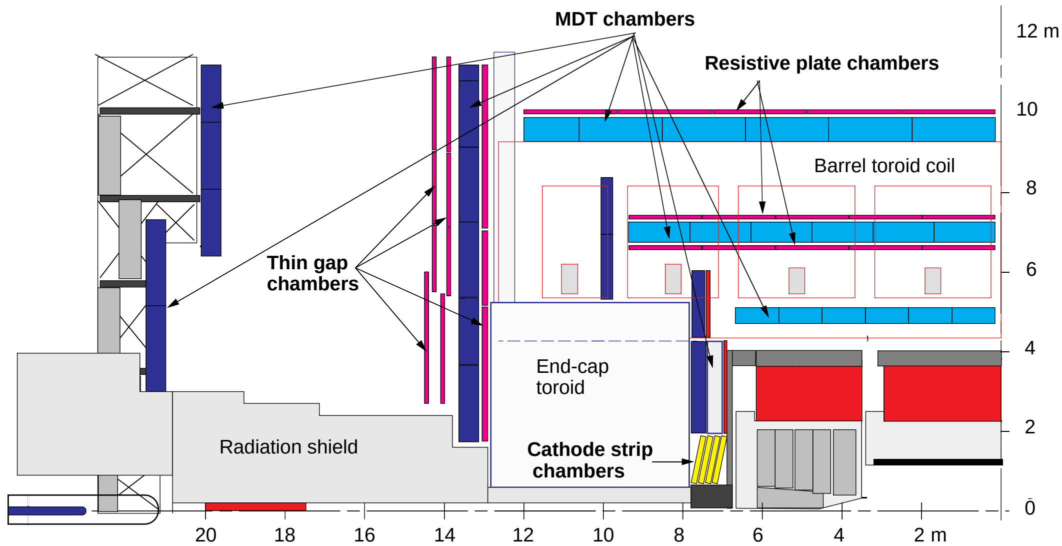

Figure 15: Side view of one quadrant of the ATLAS detector. The interaction point is situated in the lower right corner of the figure.

A RPC is a gaseous detector with a typical spatial resolution of 1 mm and a time resolution of 1.5 ns. The basic detector unit consists of a thin gas gap formed by two Bakelite plates, separated by insulating spacers. The gas gap is filled with a gas mixture of 97% tetrafluorethane ($C_2H_2F_2$) and 3% isobutane (C_4H_1O). The chambers are operated with a typical electric field of 4.5 kV/mm. A trigger chamber is read out using two orthogonal series of pick-up strips: the η strips are parallel to the MDT wires and as such determine a position in the bending plane of the magnet, the ϕ strips are orthogonal to the MDT wires and provide a measurement of the position along the MDT wire required for the precise calibration of the MDT tubes. The measured time in the RPCs is read out and made available during offline reconstruction.

2.6.2 Trigger Gap Chambers

The TGCs are similar in design to multiwire proportional chambers, with the difference that the anode wire pitch is larger than the cathode-anode distance. They have been developed for the OPAL detector, and successfully operated in that experiment for several years. Thin gap chambers filled with CO_2 npentane mixture (55:45), operate in a saturated mode at the nominal high voltage of 2.9 kV. A schematic view is presented in Figure 16. The anode plain is sandwiched between two cathode planes made of 1.6 mm G-10 plates on which the graphite cathode is deposited. On the backside of the cathode plates, facing the center plane of the chamber, etched copper strips provide the readout of the azimuthal coordinate. Signals from the anode wires together with the

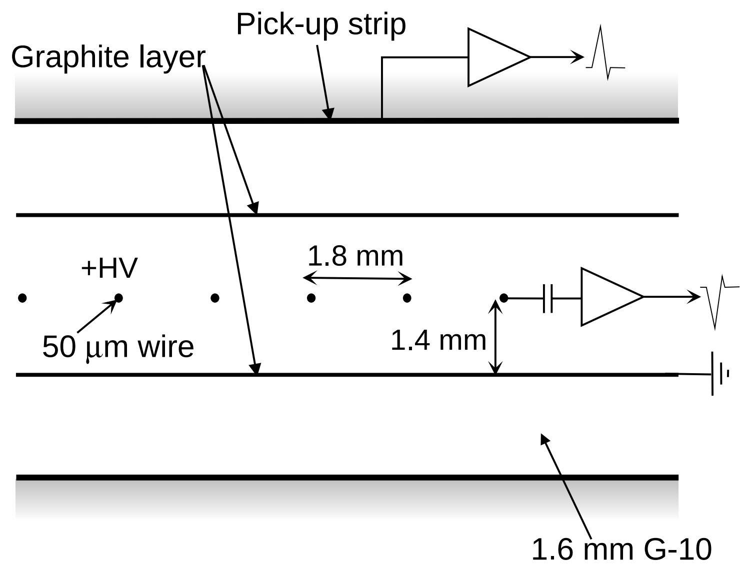

Figure 16: Schematic view of a thin gap chamber.

readout strips arranged orthogonal to the wires provide the trigger information. TGCs are characterized by:

- saturated-mode operation, leading to small Landau tails and a pulse shape from slow neutrons similar to that from minimum-ionizing particles;
- small sensitivity to magnetic field;
- fast signals with a typical rise time of 10 ns and r.m.s. time resolutions $\leq 4ns$;
- rate capability of up to 150 kHz/cm^2 without signal deterioration;
- full geometrical efficiency, except for a small area of dead space needed for wire supports $(3-4\%)$;
- strip and wire readout providing redundancy for position reconstruction.

One chamber has been irradiated with 10^{11} $particles/cm^2$ [65] with no expected deterioration in response. This is equivalent to the exposure during three years of LHC operation at the highest rapidities covered by the muon spectrometer. In the ATLAS detector, the units are mounted on big wheels. The size of the various units depends on the radial position and the station number. There are 11 types of units, (T1 to T11). The active area of the various chambers is changing from 1.31 m^2 to 2.27 m^2. The trigger TGC chambers cover an area of 3750 m^2 and the total number of the readout channels is 490000. The ATLAS TGCs were designed and built at the Weizmann Institute in Israel, at KEK in Japan as well as at the Shandong University in China. There were three test sites to check the performance of the TGC units, two in Israel, at the Technion and at Tel-Aviv University, and one at Kobe University in Japan. The purpose of these tests was to provide a detailed map of detection efficiency and time resolution for each detector. As part of my PhD service I was involved in the design, construction and operation of the Tel-Aviv Cosmic ray Testbench [66].

2.6.3 Muon reconstruction performance

Within the ATLAS experiment has a few reconstruction algorithms for Muon Spectrometer and Inner Detector tracking were prepared.
Muon spectrometer tracking

- **MuonBoy** is a muon spectrometer ”standalone” track reconstruction code. Its core algorithms are written in Fortran-90 and has been in development for more than 13 years. It is a product of the Saclay Muon Software Group . It is very well integrated into the Athena framework via C++ wrappers. Muonboy includes segment pattern recognition at the MDT/CSC and trigger chamber level, global spectrometer track tracing through the B field, track fitting to extract the momentum, and back propagation to the interaction point.

- **MOORE** Muon Object Oriented Reconstruction- is a C++ based Muon Spectrometer reconstruction package. MOORE was conceived from its inception to be a modular code and to exploit the inheritance virtues of C++ and Object Oriented Programming. This initiative was also required in order to conform to LHC mandated initiatives to bring CERN software into the realm of C++ and OOP.

- **Mugirl** The philosophy of MuGirl is to associate an inner detector track to muon spectrometer activity. It uses pattern recognition algorithm and cleverly incorporates reasonable assumptions about MDT low level performance. The result is highly efficient and low fake rate segment finder. Mugirl uses all spectrometer technologies towards segment identification: It is designed to find patterns in the RPCs, TGC, MDT and CSC. It incorporates an artificial neural network to combine the information from each source of hits. In this regard MuGirl promises to be highly efficient low noise. The Mugirl group also intends to provide full tracking in the spectrometer and not confine itself to just the low p_T regime. In this sense it is complimentary to the spectrometer based muon finders.

Inner Detector tracking

- **iPatRec** began life in 1992 as an Inner Detector reconstruction program, written in Fortran, with digits as input and track as output. The current version retains the same basic strategy, although all aspects of the performance have been considerably enhanced. This modern version took shape between 1998 and 2002, with the conversion to a modular set of C++ packages. Concurrently, certain other reconstruction packages adopted the iPatTrack data model in order to profit from the tools for track-fitting and extrapolation through the solenoid and toroid fields.

- **xKalman** tracking, in its original form, initiates a track search in the TRT where track density is lowest. The current version allows a variety of reconstruction strategies, and can, for example, elect to seed the track search from Silicon strips (SCTs) and Pixels detectors and not use the TRT at all. From the initial track seeds a global pattern recognition flags all possible helical trajectories over the full acceptance of the detector. These helices define search roads through the precision detectors. Starting from initial helices, the xKalman fitter propagates a track candidate to successive hits or measurements. At each step the track parameters and covariance matrices are updated based on the last measurment to be added. In this fashion the fitter predicts where its next hit is likely to be- and therefore accomplishes pattern recogntion and track fitting together

The momentum resolution of muons, produced at the interaction point, is studied in detail with help of an analytical method, taking into account the detailed detector geometry, the material distribution and the magnetic field [64]. The results of the study are summarized in Figure 17. The left figure shows the contributions to the resolution averaged over the region $|\eta| < 1.5$, the right figure shows the results for the region $|\eta| > 1.5$. The figure shows the main contributions to the muon momentum resolution as a function of the p_T . One can identify three regions:

- Low momenta, $p_T < 30$ GeV, the resolution is dominated by the energy loss of the muons in the calorimeter;

- Intermediate momentum range, $30 < p_T < 100$ GeV, the resolution is mainly determined by multiple scattering;

- High muon momenta, $p_T > 100$ GeV, the impact of the single tube resolution as well as the precision of the calibration and the alignment of the tracking chambers becomes more and more important and dominates the resolution for momenta larger than 300 GeV.

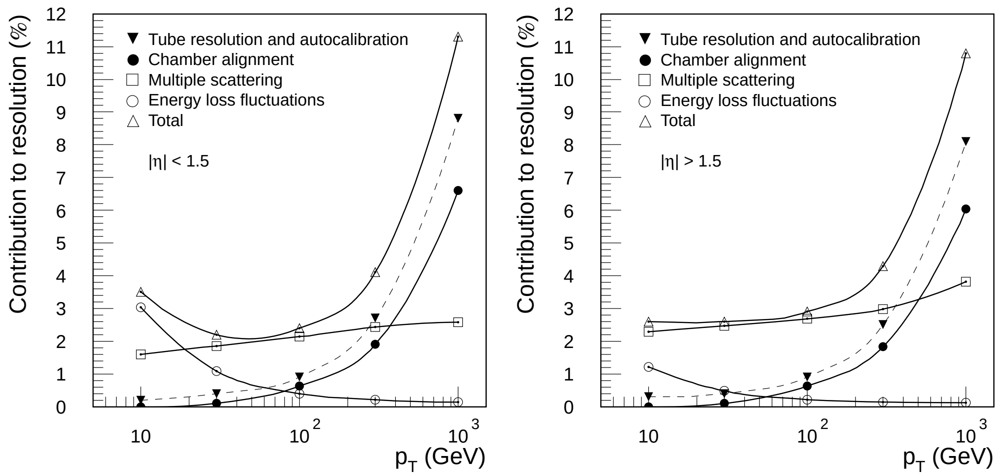

Figure 17: Contributions to the momentum resolution, averaged over $|\eta| < 1.5$ (left plot) and averaged over $|\eta| > 1.5$ (right plot).

As seen in the following sections the polarization study shows the importance of high quality calibration constants for the MDT chambers in ATLAS to achieve the maximum possible momentum resolution for low energetic muons.

3 The trigger system

The LHC will collide protons at a rate of 40 MHz, which together with pile-up will result in an interaction rate of up to around 1 GHz. The ATLAS trigger acts to reduce this interaction rate to around 100 Hz written to mass storage, whilst keeping ‘interesting’ events. To make this possible the usual strategy is a two-step procedure. The first step is the online (i.e. in real time) pre-selection of interesting events (triggering) to reduce the huge 40 MHz bunch crossing rate to a manageable event rate of about 100 Hz, which are written to mass storage devices. In the second step, the stored data is reconstructed offline to yield quantities like tracks, energy clusters, jets, missing transverse energy, secondary decay vertices, etc. These quantities are subject to various physics selection criteria in offline analyses, for example to maximise the efficiency and purity in direct J/ψ particle idintification. This paragraph outlines the online data reduction (trigger) scheme shown schematically in Figure 18.

The first level trigger (LVL1) is designed to operate at a maximum pass rate of 75 kHz. The LVL1 decision time (called latency) is 2 μs. The information of all detector channels must be stored in pipeline memories, because the LVL1 latency extends over many of the 25 ns spaced LHC bunch crossings. The LVL1 decision is based on information with a coarse granularity of two sub-detector systems: the muon trigger chambers and the calorimeters. Quantities used in the LVL1 decision are typically: the estimated transverse momentum of muon candidates, the total energy deposited in the calorimeters, the missing (transverse) energy in the calorimeters and the occurrence of isolated energy depositions in the calorimeters. For events accepted by the LVL1, the information of all sub-detector systems is pre-processed and stored in the so-called Read-Out Buffers (ROBs).

The second level trigger (LVL2) uses both the LVL1 output and the data stored in the ROBs to further reduce the data rate to a maximum of 1 kHz. Even though the LVL2 has access to the full data, the selection is generally restricted to so-called Regions of Interest (RoI) as flagged by the output of the LVL1. For a LVL1 muon trigger, the LVL2 will use the information from the precision MDT chambers to improve the muon momentum estimate, which allows a tighter cut on this quantity. For a LVL1 calorimeter trigger, the LVL2 has access to the full detector granularity, and has in addition the possibility to require a match with a track reconstructed in the inner detector. The LVL2 has an event dependent latency, which varies from 1 ms for simple events to about 10 ms for complicated events. For events accepted by the LVL2, the data fragments stored in the ROBs are collected by the so-called Event Builder and written into the Full Event Buffers. The third trigger stage is called LVL3 and uses the information stored in the Full Event Buffers to keep the event rate sent to mass storage below 100 Hz. The LVL3 can use complex offline algorithms like track reconstruction, vertex finding, etc., because it has access to the complete event. For the maximum trigger rate of 100 Hz, the data rate written to mass storage corresponds to 100 MB/s. One nominal LHC

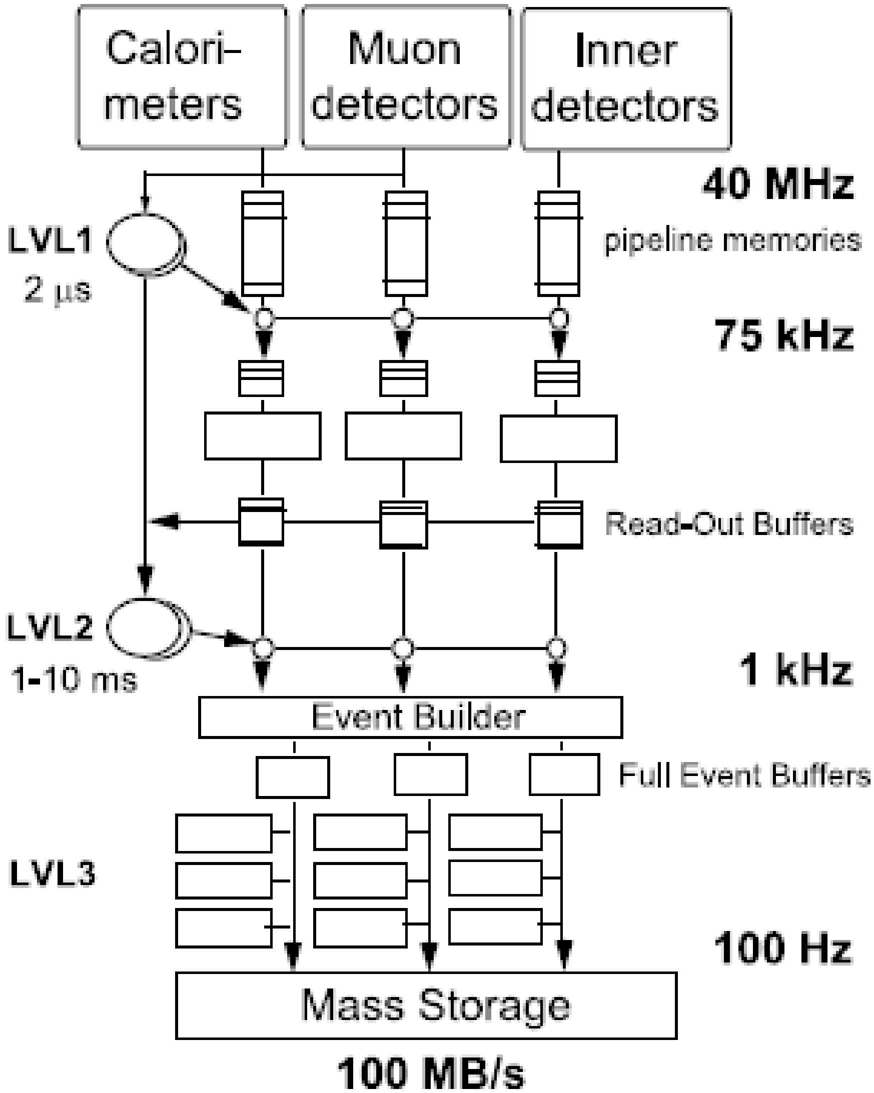

Figure 18: Schematic view of the ATLAS trigger system. The three trigger levels (LVL1, LVL2, LVL3) are indicated, including the latencies (on the left side) for the first two. The frequencies on the right side give the input LHC bunch crossing frequency (40 MHz) and the maximum allowed output frequencies of the respective trigger levels (75, 1, 0.1 kHz).

running year counts 10^7 s and therefore amounts to a total data volume of 1 PB (10^9 MB) annually.

Quarkonium production will be subject to trigger cuts on di-muons at Level-1 and Level-2.

3.1 Quarkonium Trigger

This section discusses the trigger signatures relevant for quarkonium production at these two levels, the implications they have on the measured cross-section and the expected effects they will have on our ability to make various physics measurements.

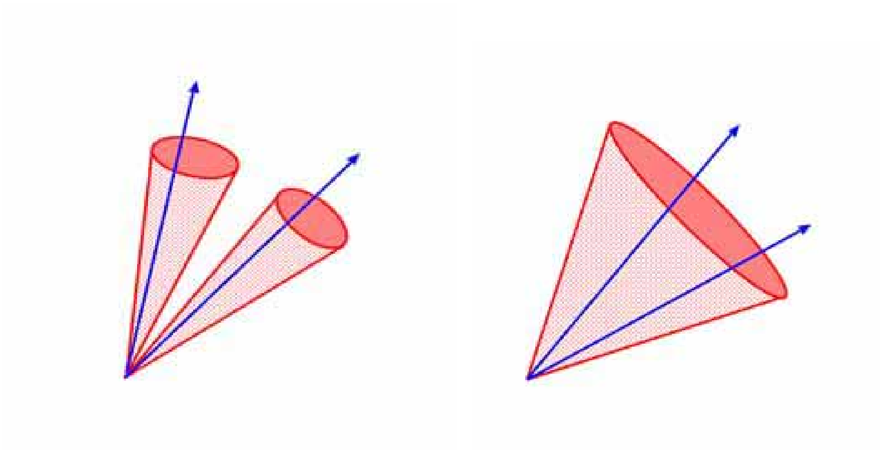

Figure 19: Two types of dimuons triggers the topological trigger (left) and the "TrigDiMuon" trigger (right).

Two specific types of trigger dedicated to quarkonium (see Figure 19) are the topological di-muon triggers (left plot), which require two Level-1 regions of interest (RoIs) corresponding to two muon candidates with p_T's above thresholds of 4 and 6 GeV respectively, and "TrigDiMuon" di-muon triggers that only requires a single Level-1 RoI above a threshold of 4 GeV and searches for the second muon of opposite charge in a wide RoI at Level-2. The J/ψ production rates are presented in Table 3 Further details can be found in [75]. Both of these trigger types will be used to select quarkonium in data-taking. An additional trigger strategy based on a higher p_T single muon trigger is discussed in Section 3.5 If not stated otherwise, the quoted trigger efficiencies have been calculated with respect to the Monte Carlo samples, generated with the cuts $p_T(\mu_1) > 6$ GeV , $p_T(\mu_2) > 4$, where μ_1 (μ_2) is the muon with the largest (second largest) transverse momentum in the event ($\mu 6 \mu 4$).

Threshold (GeV)	Chain starting	TrigDimuon J/ψ rate (Hz)	TrigDimuon Total rate (Hz)	Topological trigger J/ψ rate (Hz)	Topological trigger Total rate (Hz)
$4(10^{31})$	Level-1	1.2	3.5	0.8	24
	Level-2	1.15	2.7	0.5	0.6
$6(10^{33})$	Level-1	43.5	180.5	32.5	357.5
	Level-2	35	126	8.7	9.3

Table 3: The trigger rates. The initial rate of 10^{33} (low luminosity) is taken for LVL1 so the rate for LVL2 is 10^{31}.

3.2 Level-1 Trigger

From Figure 20 we can learn that in order to reduce the low p_T contributions (pion/kaon decays colored in green, photon decays colored in red and b-hadrons decays colored in blue) in $pp \rightarrow \mu$ production we need to set a threshhold on the muon p_T at the level of a few GeV.

The Level-1 trigger is a hardware trigger that uses coarse calorimeter and muon spectrometer information to identify interesting signatures to pass to the Level-2 and Event Filter stage.

The total single-muon trigger efficiency at Level-1 running over direct J/ψ events is 96%. Figure 21 shows the various individual Level-1 trigger efficiencies as a function of the J/ψ p_T.

In this dataset, only those triggers which have greater than 2% efficiency in some region of p_T are displayed.

3.3 Level-2 Trigger

The Level-2 trigger is software-based and is designed to reduce the output rate of the data, passed to it from Level-1, by two orders of magnitude. Within regions of interest defined by the Level-1 trigger, full granularity of the detector is accessible. The Table 4 presents some of Level-2 trigger signatures of interest for quarkonium studies .

Many more trigger signatures will be available for data-taking. The efficiency of the Level-2 triggers described above on direct J/ψ events are plotted in Figure 22 as a function of J/ψ p_T. Only those triggers which have greater than 2% efficiency in this dataset in some region of p_T are displayed. Note that these are relative trigger efficiencies to the Level-1 trigger, and not absolute efficiencies at the Level-2 trigger stage. The total Level-2 trigger efficiency in the reconstructed data is 94%.

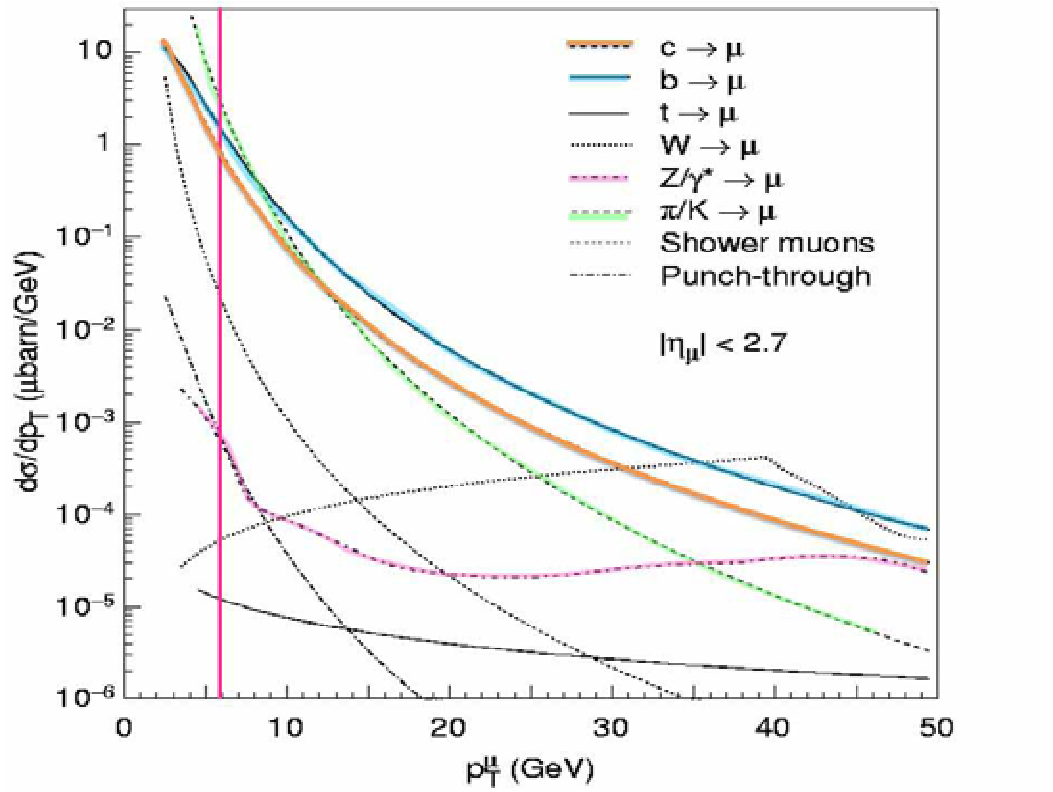

Figure 20: Muon production channels.

LVL1 trigger threshold	LVL2 trigger threshold	Trigger name
0	0	L2_BJpsimu0mu0
5	5	L2_BJpsimu5mu5
6	6	L2_BJpsimu6mu6
6	4	L2_BJpsimu6mu4
10	10	L2_mu10
20	20	L2_mu20i

Table 4: The following triggers , for selection direct/indirect $J/\psi \rightarrow \mu^{+}\mu^{-} + X$ decay channel, are implemented in Atlas Trigger menu .

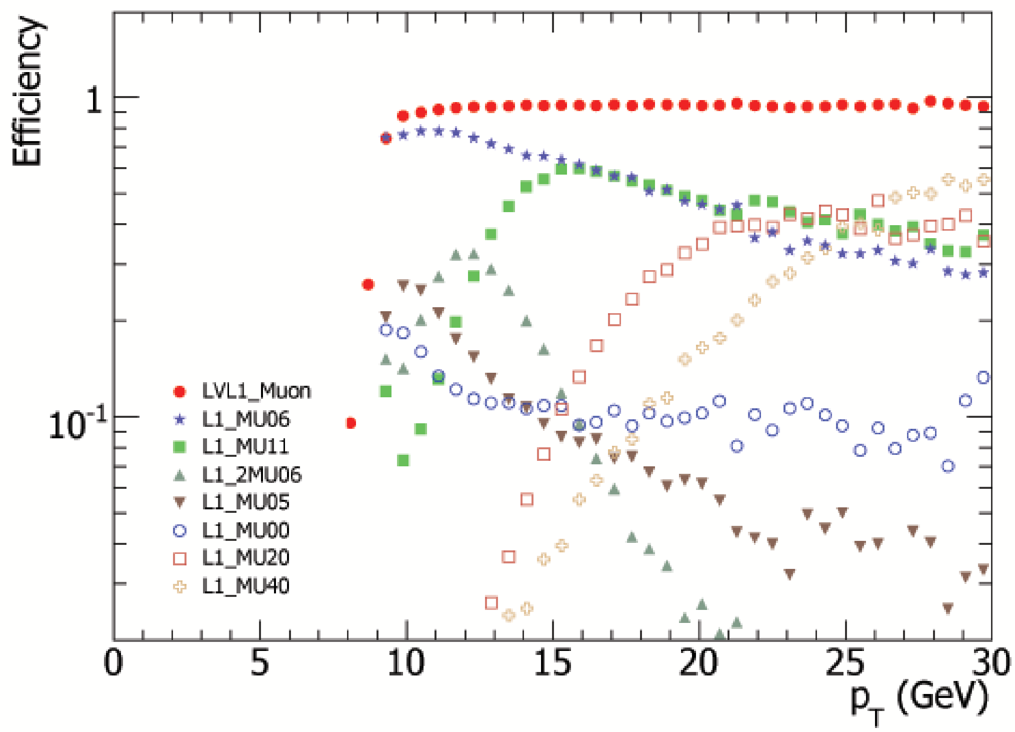

Figure 21: Efficiency of various Level-1 triggers on direct J/ψ events versus J/ψ p_T. The efficiency curve labelled `LVL1_Muon` is the sum of all LVL1 single muon efficiencies.The single muon p_T threshold (on XX GeV) triggers namely `L1_MUXX` and the di-muon trigger namely `L1_2MUYY` when YY is the same p_T threshold on LVL1 and LVL2 triggers.

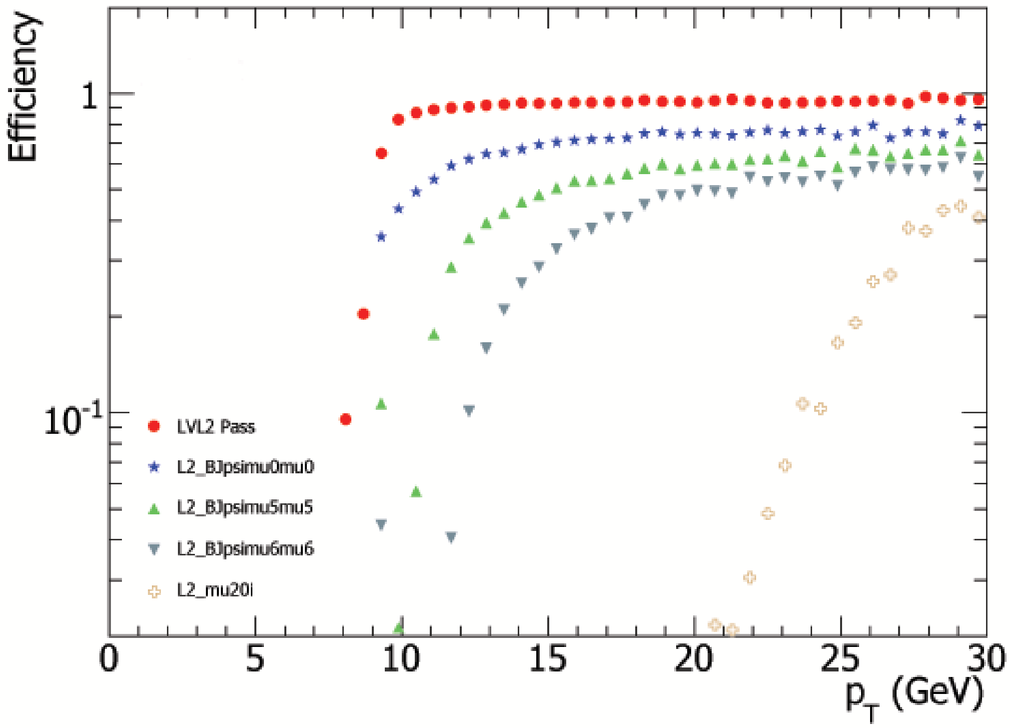

Figure 22: Efficiency of various Level-2 triggers on direct J/ψ events versus J/ψ p_T. The efficiency curve labelled `LVL2_Pass` is the sum of all LVL2 efficiencies.

3.4 Trigger efficiency estimation

Being able to determine the trigger efficiency of measured J/ψ is crucial to be able to correctly infer the production cross-section of quarkonium at the LHC. Indeed, using J/ψ (as well as the Υ the Z) to construct a trigger efficiency map will be a necessity if any cross-sections of Standard Model or new physics processes are to be measured successfully at ATLAS.

Studies have been conducted into developing an online calibration method to obtain the low-p_T single muon trigger efficiency, and henceforth the di-muon trigger efficiency of events using real data by virtue of the so-called 'track and probe method'. Briefly, the method permits extraction of the muon trigger efficiency by applying the following recipe:

1. Select events where one muon is triggered at Level-1 (this is the 'tag' muon).

2. Offline reconstruction — build the object (e.g. J/ψ) with invariant mass cut and remove triggered muon.

3. Analyse of the second 'probe' muon to calculate single muon efficiency based on whether this muon would have triggered the event.

Further details of this method can be found in [78].

It is worth noting that the J/ψ are individually very good candidates for studying low-p_T muon trigger efficiencies, as the different masses and complementary decay kinematics allow access to different momentum regions and different angular separation of the muons .

An important consideration for calculating the di-muon trigger efficiencies of J/ψ is the angular distribution of the decay angle $\cos\theta^\star$ — the angle between the direction of the positive (by convention) muon from quarkonium decay in the quarkonium rest frame and the direction of quarkonium itself in the laboratory frame (Figure 23, see Section 5 for more details).

The distribution depends on the relative contributions of the various production mechanisms (Section 1) and is as of yet not fully understood. Crucially, Monte Carlo studies have shown that different production mechanisms (and thus different angular distributions) can have significantly different trigger acceptances which requires well understanding in order to correctly measure the J/ψ polarization.

3.4.1 Effect of di-muon trigger cuts on charmonium rates

Before incorporating trigger and reconstruction efficiencies, the predicted cross-sections for $pp \to J/\psi \to \mu^+\mu^- + X$ were calculated for a number of p_T thresholds on the di-muon trigger (see Table 5 for details). Figures 24 illustrates the distribution of cross-sections across the values of the p_T of the harder and softer muon from the quarkonium

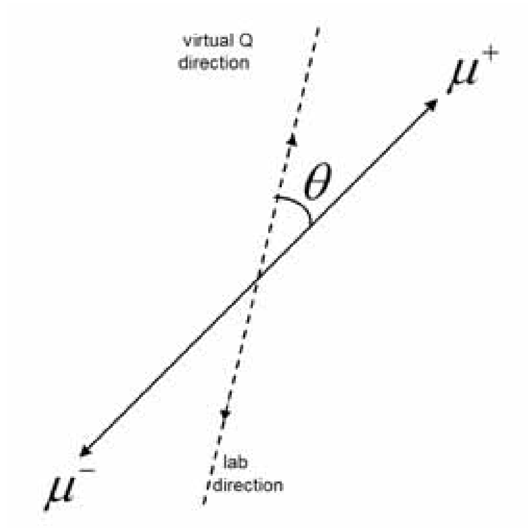

Figure 23: Spin align diagram.

decay without any muon cuts applied at generator level and zero polarisation. The lines overlaid on the plots represent the 6+4 GeV ($\mu 6 \mu 4$) and 4+4 GeV ($\mu 4 \mu 4$) di-muon trigger cuts, as well as the cuts corresponding to the single muon trigger $\mu 10$ (see Section 3.5 for details and discussion).

For J/ψ the bulk of the cross-section lies near the 4+1 GeV region, far from the low-p_T muon trigger thresholds proposed for ATLAS, and we see only a small increase in accessible cross-section by lowering the cut on the harder muon from 6 GeV to 4 GeV (although this reduction in the effective J/ψ p_T threshold is still useful from a physics standpoint).

No ψ and higher states of Υ were simulated for this analysis, but the expected cross-sections have been estimated from Tevatron results applied to ATLAS acceptances and trigger efficiencies. Estimated cross-sections of these higher states for two di-muon trigger scenarios are also presented in Table 5.

It is likely that the true cross-section measured at ATLAS will be higher than the values quoted above, as during early running the low p_T muon trigger will run with an open coincidence window in η at Level-1 (trigger item L1_MU00) and no requirement of an additional Level-2 di-muon trigger. The L1_MU00 trigger item has a turn-on threshold at around 4 GeV (giving the 4+4 GeV trigger scenario quoted above) but in practice there is a non-zero trigger efficiency below 4 GeV, which combined with the large rate of low p_T muons may add a significant additional contribution to the overall cross-section.

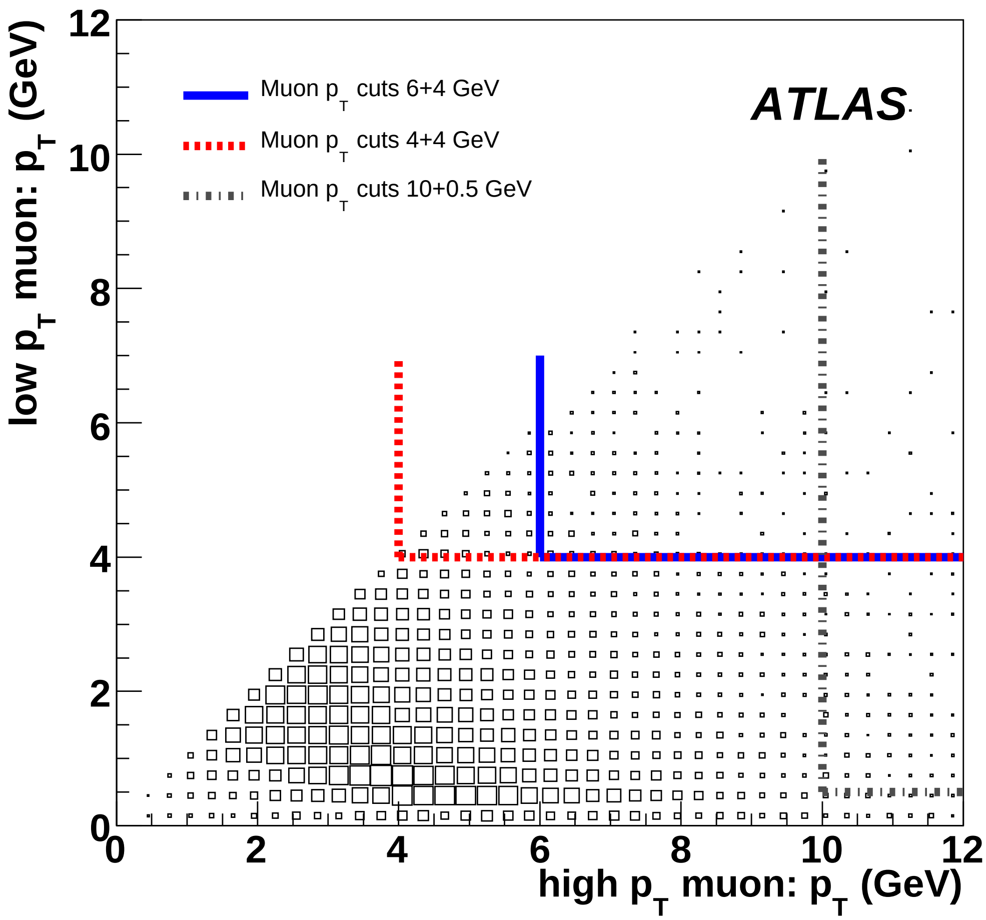

Figure 24: Density of J/ψ production cross-section as a function of the hardest and softer muon p_T of muons coming from J/ψ. No cut was placed on the generated sample, but the overlaid lines represent the thresholds of observed events with trigger cuts applied.

Quarkonium	Cross-section, nb			
	$\mu4\mu4$	$\mu6\mu4$	$\mu10$	$\mu6\mu4\cap\mu10$
J/ψ	28	23	23	5
ψ'	1.0	0.8	0.8	0.2
$\Upsilon(1S)$	48	5.2	2.8	0.8
Υ(2S)	16	1.7	0.9	0.3
Υ(3S)	9.0	1.0	0.6	0.2

Table 5: Predicted cross-sections for various prompt vector quarkonium state production and decay into muons, with di-muon trigger thresholds $\mu4\mu4$ and $\mu6\mu4$ and the single muon trigger threshold $\mu10$ (before trigger and reconstruction efficiencies). The last column shows the overlap between the di-muon and single muon samples.

3.4.2 Effect of trigger on analysis

As discussed above, the p_T differential cross-section for charmonium is composed of three main classes of processes: direct singlet production, octet production and singlet production of χ states. Figure 25 illustrates the contributions of these three classes to the overall production rate for J/ψ once muon p_T trigger cuts of 6 and 4 GeV are applied to the muons coming from the J/ψ .

Lower p_T trigger cuts will enhance the rate of J/ψ production measured at ATLAS and allow for analysis of color singlet production, which is expected to dominate for charmonium with $p_T < 6$ GeV. As seen in Figure reffig:L2Jpsitrigeff the J/ψ can only be observed above around 8 GeV. Lower trigger cuts available during early running, such as the 4+4 trigger described above, will allow the opportunity to explore this low-p_T region further and help separation of octet and singlet contributions.

3.4.3 Angular distribution with di-muon triggers

In the case of a di-muon trigger, both muons from the J/ψ decays are required to have relatively large transverse momenta. Whilst this condition allows both muons to be identified, it also severely restricts acceptance in the polarisation angle (see Section 5 for more details), meaning that for a given p_T of J/ψ a significant fraction (up to 60%) of the total cross-section is lost. An example of the polarisation angle distribution for a $\mu6\mu4$ trigger is shown in Figure 26. Here, the samples for both J/ψ were generated with zero polarization, so with full acceptance the corresponding distribution in $\cos\theta^\star$ should be flat, spanning from -1 to $+1$.

With the above trigger cuts, J/ψ decays where the two muons have equal transverse momenta have $\cos\theta^\star \simeq 0$, while in order to have $|\cos\theta^\star|$ close to ±1 one muon's p_T

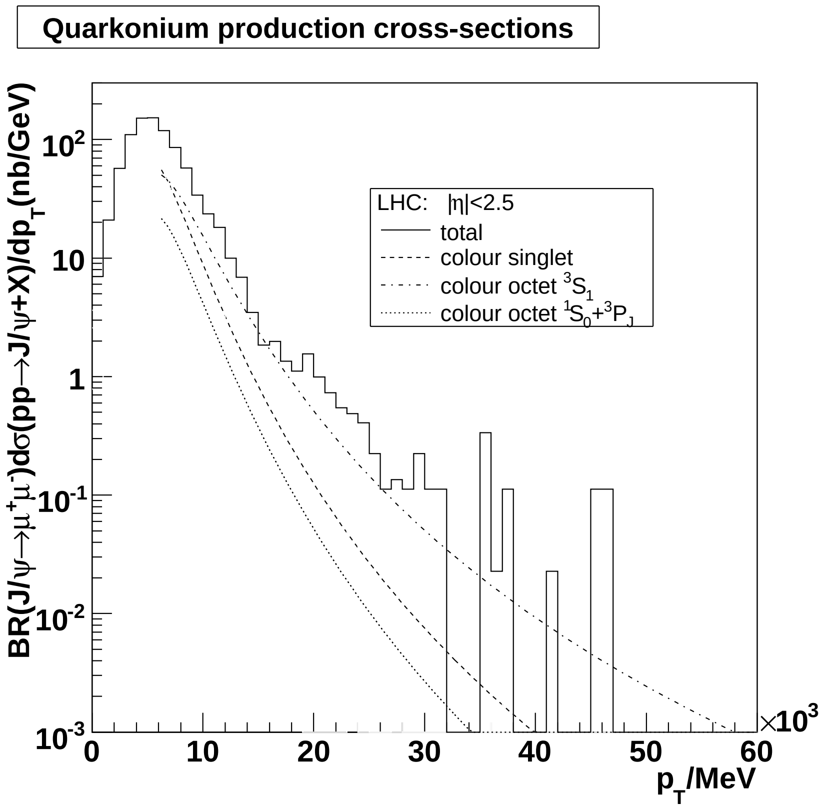

Figure 25: Monte Carlo differential cross-section for J/ψ production with J/ψ p_T with the differential cross-section contributions from direct color singlet, singlet χ production and octet production overlaid.

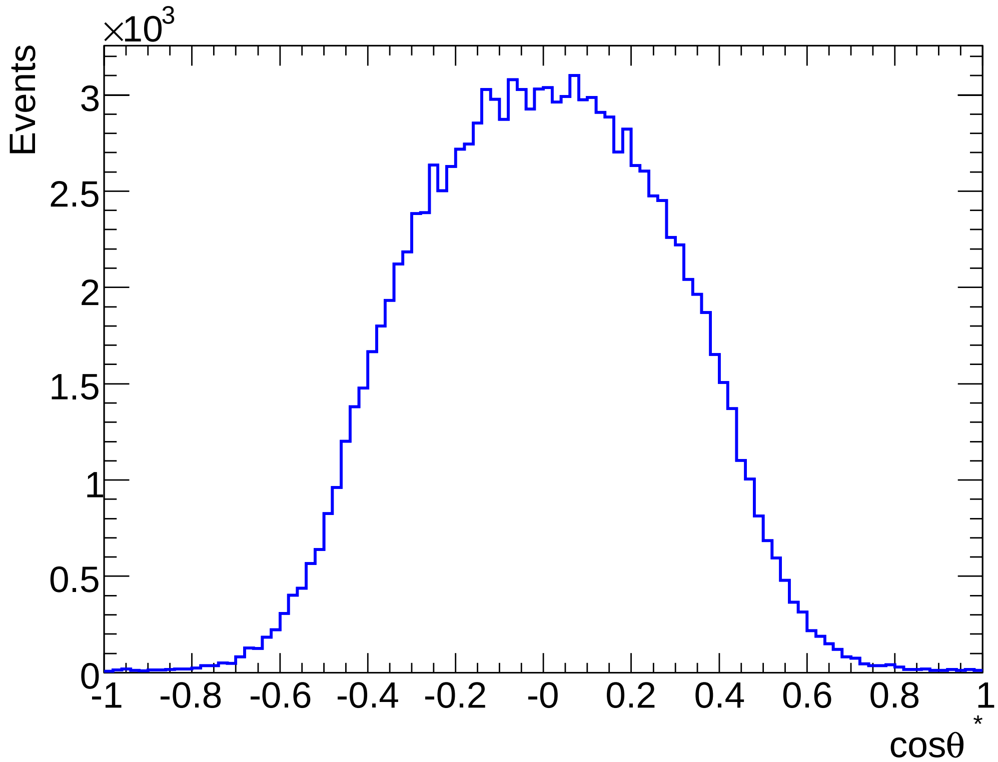

Figure 26: Example of the loss of acceptance in the reconstructed polarisation angle distribution when using a $\mu6\mu4$ di-muon trigger for J/ψ . The *true* angular distribution in both cases should be flat.

needs to be very high, while the other's p_T is very low. In fact, in order to achieve a configuration with $|\cos\theta^\star| \simeq 1$, one must have

$$\frac{p_{\mu 1}}{p_{\mu 2}} \simeq \left(\frac{M_Q}{m_\mu}\right)^2 \simeq 900 \tag{8}$$

which is a very unlikely configuration in ATLAS. Therefor for di-muon trigger $\mu 6\mu 4$, events with large $|\cos\theta^\star|$ are lost due to the p_T cut on the softer muon. Narrow acceptance in $|\cos\theta^\star|$ complicates and may bias thes polarisation measurements.

3.5 Single muon trigger

Another possibility for charmonium reconstruction is to trigger on a single identified muon. Once this muon triggers the event, offline analysis can reconstruct the charmonium by combining the identified muon with an oppositely-charged track in the event.

The single muon trigger has an advantage over the di-muon trigger for polarisation studies, providing complementary acceptance in the polarisation angle compared to the di-muon triggered events. The single muon trigger also provides significant event overlap with the di-muon trigger (mainly at high p_T regime) for an independent calibration of the muon trigger acceptance.

By using a single muon trigger, one removes the need for two muons to trigger the event, and hence removes the need for the other muon to have a large p_T. In this configuration, one has a 'fast' muon, that triggered the event, and one 'slow' (unidentified) muon, whose transverse momentum is limited only by the track reconstruction capabilities of ATLAS with a threshold around 0.5 GeV. This is demonstrated in Figure 24 in gray line. As explained above, these events should have much higher values of $|\cos\theta^*|$, and would thus fill the gaps to the left and to the right of the peak, as illustrated in Figure 26. The main and most important disadvantage of using this trigger scheme is the amount of background events that are entering in the data sample.

An important consideration for J/ψ reconstruction with a single muon trigger is the measured cross-section of both the J/ψ signal itself (which from Figure 24 can be seen to increase dramatically without a second muon requirement) and the backgrounds, which have much larger single muon cross-sections than the di-muon equivalents [79]. The main background sources to J/ψ in this case are kaon and pion decays in flight, $cc \to \mu X$ and $bb \to \mu X$. Out of these, $bb \to \mu X$ have by far the hardest muon spectrum and are expected to dominate in the area of interest $p_T(\mu) > 6$ GeV, with an estimated cross-section of 6.14 μb.

In order to reduce the overall rate, as well as to reduce the combinatorial background under the J/ψ peak, the single muon trigger cut of $p_T > 10$ GeV was used (a non-prescaled Level-1 single muon trigger '$\mu 10$'). With this trigger, the cross section corresponding to the main background, $bb \to \mu X$, is about 1 μb, while the contribution of the 'signal' process $pp \to J\psi X$ is about 15 nb.

The expected cross section for prompt J/ψ production with the single muon trigger $\mu 10$ is comparable to that with the di-muon triggers.

The single muon trigger sample allows for wider acceptance in the decay angle distribution, largely complementary to the di-muon sample.

4 Charmonium reconstruction

In this section we show the reconstruction performance for charmonium based on the $\mu 6 \mu 4$ di-muon trigger scenario. We present the expected reconstruction efficiencies, resolutions and acceptances for onia at ATLAS, and analyse the main background sources. At ATLAS, muon candidates consist of tracks reconstructed in the Inner Detector (ID), ID tracks tagged with muon spectrometer hits or simply standalone muons from the muon spectrometer. The candidates are initially recorded by the trigger system described in Section 3. In each event which passes the di-muon trigger, all the reconstructed muon candidates are combined into oppositely charged pairs, and each of these pairs is analysed in turn. Truth-matching of reconstructed tracks is achieved using a η-ϕ match to the Monte Carlo generated information (mc-truth), where the particle in the mc-truth that has the correct Particle Data Group (PDG) [77] ID number and the closest match in $\Delta R = \sqrt{\Delta\eta^2 + \Delta\phi^2}$ is returned. Once all the required information about the muon pair has been stored. The invariant mass is calculated and if the mass is above 1 GeV, (applied to reduce the number of onium candidates rate; no upper mass limit is imposed at this point) then the CTVMFT vertexing package [76] is used to refit the two tracks to a common vertex. The fraction of surviving J/ψ candidates before the refit is 96% (constraints to refit the tracks of the muon candidates to a common vertex, if possible). If a good vertex fit is achieved, the pair is accepted for further analysis. If the invariant mass of the refitted tracks is within 300 MeV of the PDG mass , the pair is considered as a charmonium candidate. The mass windows are chosen to be about six times the expected average mass resolution.

These invariant mass distributions are plotted in Figure 27.

Vertexing stage	Candidates reconstructed	ΔM	Resolution
Before	96%	3 MeV	54 MeV
After	87%	4 MeV	54 MeV

Table 6: Percentage of J/ψ candidates reconstructed (without trigger efficiencies) in ± 300 MeV mass interval in the direct J/ψ sample, before and after vertexing, along with the corresponding invariant mass deviation from PDG values and derived resolutions.

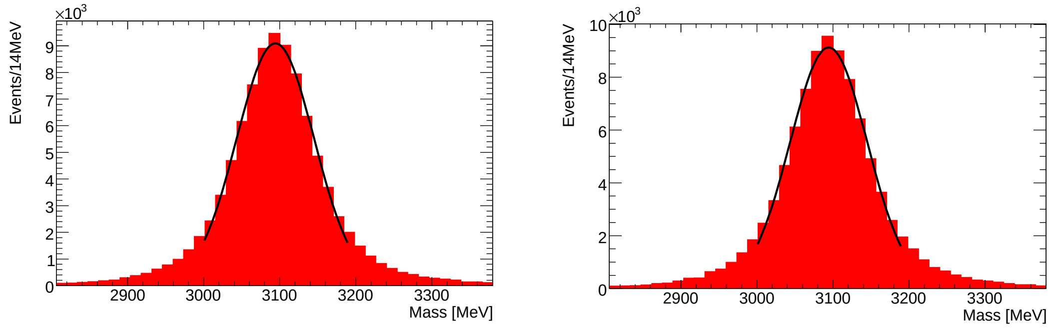

(a) J/ψ before vertexing

(b) J/ψ after refitting

Figure 27: J/ψ invariant mass distribution for muon candidates before and after the unconstrained vertex fit.

Table 6 summarises the invariant mass distributions of the J/ψ that result pre- and post-vertexing.

The invariant mass resolution depends on the pseudorapidities of the two muon tracks. To illustrate this effect (Fugure28), all accepted onia candidates are divided into three classes depending on the η of the muons, and Gaussian fits are performed to determine the resolutions and mass shifts.

The results are presented in Table 7.

charmonium	$M_{\text{rec}} - M_{\text{PDG}}$, MeV	Resolution σ, MeV			
		Average	Barrel	Mixed	Endcap
J/ψ	$+4 \pm 1$	53	42	54	75

Table 7: Mass shifts and resolutions for di-muon invariant mass distributions after the vertex fit, for J/ψ candidates.

It is found that the mass resolution is the highest when both tracks are reconstructed in the barrel area, $|\eta| < 1.05$, degrades somewhat if both tracks are reconstructed in the endcap region, $|\eta| > 1.05$, and is close to its average value for the mixed η events. It should be noted that no significant non-gaussian tails are observed in either of these distributions, and the fit quality is good ($\frac{\chi^2}{dof} < 10$). Also shown in the table are the shifts of the mean reconstructed invariant mass from the respective $M_{J/\psi} = 3096.9$ PDG value. The observed mass shifts are due to a problem with simulation of material effects in the endcap, which has since been understood and corrected(see Section 4.5)

The reconstructed muon pairs that remain after vertexing cuts are considered to be

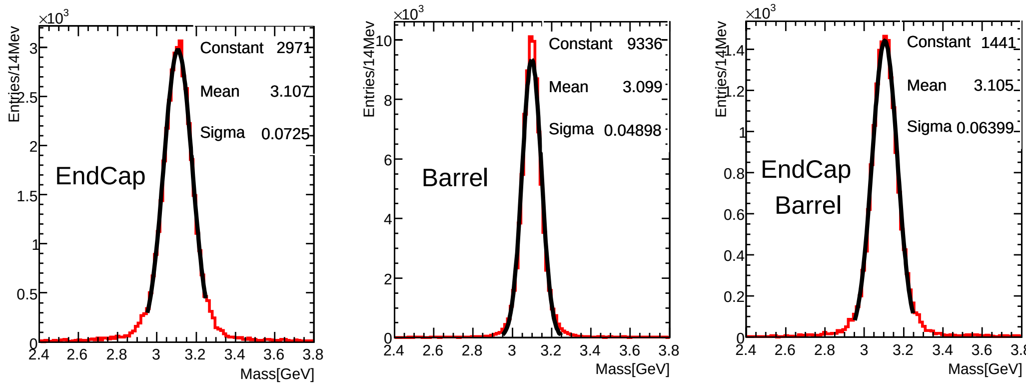

Figure 28: Mass and resolution of J/ψ invariant mass plotted separately for various η region of the two muons. 'Barrel' refers to the region $|\eta| < 1.05$ and 'Endcap' refers to the region $1.05 < |\eta| < 2.7$.

good charmonium candidates and further analysis is done using these pairs only. The transverse momentum distributions of these candidates are shown in Figure 29.

As can be seen from the Figure 27 (a), prompt J/ψ are mainly produced with p_T above around 10 GeV, due to the di-muon trigger cuts applied to the events. Even at these, relatively low statistics, one expects to see significant numbers of charmonia at large p_T, which will allow statistically significant high-p_T analyses beyond the reach of the Tevatron.

Where some J/ψ are produced at lower p_T values, this is due to the event being triggered by one or more muons not from the J/ψ allowing the muons from the J/ψ to be accepted with lower p_T's. The mean J/ψ p_T from events with a $\mu6\mu4$ trigger cut is 14.6 GeV. The statistical errors on this sample correspond to the number of events that will be produced within two weeks of early data-taking at low luminosity (assuming 10^{31} cm^{-2} s^{-1}).

Figure 30 (a) presents the J/ψ acceptance as a function of the J/ψ transverse momentum, relative to the Monte Carlo generated dataset, which requires the two muons be in $|\eta| < 2.5$ and have transverse momenta greater than 6 and 4 GeV, respectively. These plots take into account geometric acceptance of the detector and reconstruction efficiency losses due to vertexing, as well as trigger efficiencies.

When J/ψ are produced with a transverse momentum above 10 GeV we see a sharp rise in the acceptance as J/ψ above this threshold are able to satisfy the muon trigger requirements within a certain kinematic configuration.

The structure in the plot of the η-dependence of J/ψ reconstruction efficiency, shown in Figure 30, highlights the configuration necessary in order for muons from the

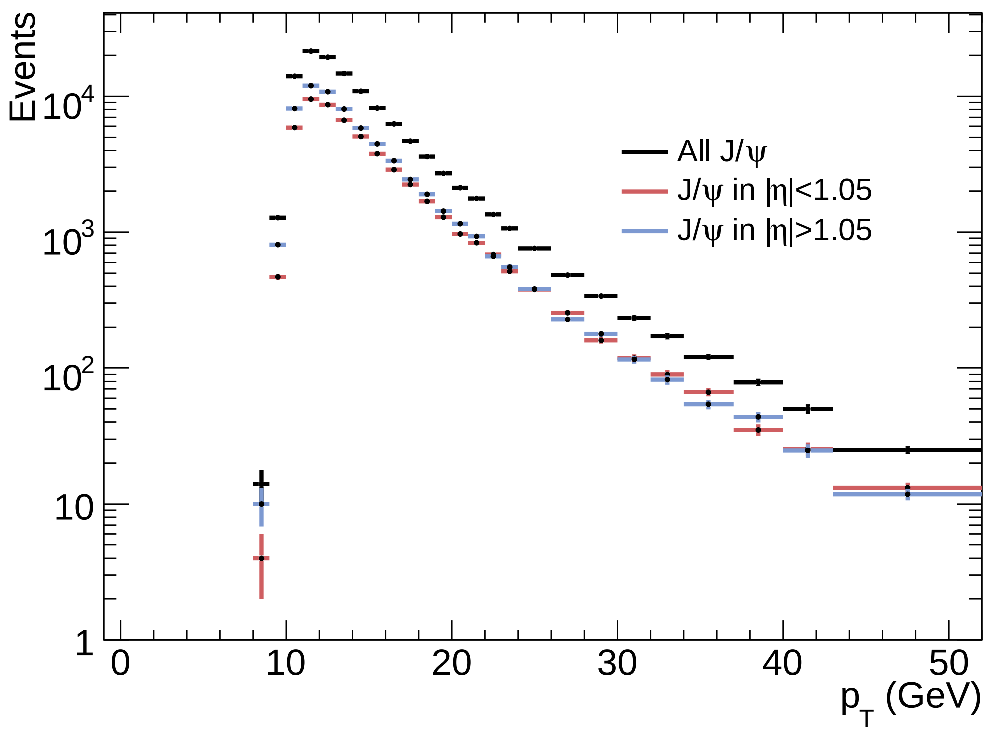

Figure 29: Transverse momentum distribution of triggered reconstructed charmonium candidates, also separated into distributions for quarkonia found in the barrel and endcap regions of the detector. Statistics shown in the figures corresponds to integrated luminosities of about 6 pb^{-1} for J/ψ .

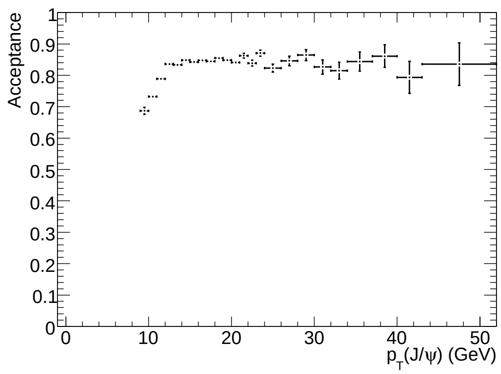

(a) J/ψ acceptance vs. p_T

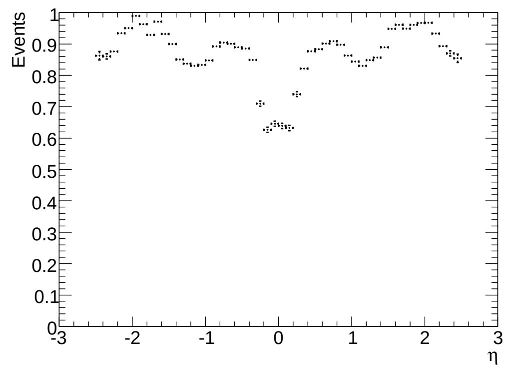

(b) J/ψ acceptance vs. η

Figure 30: Acceptance of reconstructed prompt J/ψ vs. J/ψ transverse momentum and pseudorapidity (relative to the MC generated dataset with $\mu6\mu4$ cuts).

J/ψ to be able to pass the di-muon trigger. The distribution of reconstructed charmonium candidates with the angular separation of the two muons, described by the variable ΔR, is shown in Figure 31.

On average, muons from reconstructed J/ψ ($\mu6\mu4$) candidates are separated by $\Delta R \simeq 0.47$, and are restricted from being produced at separations larger than around 0.7.

In comparison, the higher mass of Υ requires the muons in the $\mu6\mu4$ case to have much larger opening angle, with a broad distribution in ΔR peaking at around 1.8 and spanning up to 2.6. (dotted line in Figure 31 (a)). One can see that for the single $\mu10$ case in Figure 31(b) (b) the distributions are much broader, and generally with smaller separation in ΔR, reflecting the lower p_T constraint on the second muon.

The small separation of muons in ΔR for the J/ψ ($\mu6\mu4$) case has consequences for the J/ψ reconstruction efficiency as a function of pseudorapidity, shown in Figure 30(b). Significant dips in efficiency are seen near $\eta \pm 1.2$ and $\eta = 0$, due to the muon spectrometer layout [64]. As the muons from J/ψ are on average separated by only $\Delta R = 0.47$, they are subject to similar material and detector effects, and so these effects are carried over into the J/ψ reconstruction with very little smearing. Hence, this distribution has a similar shape to the individual muon reconstruction efficiency distribution in ATLAS.

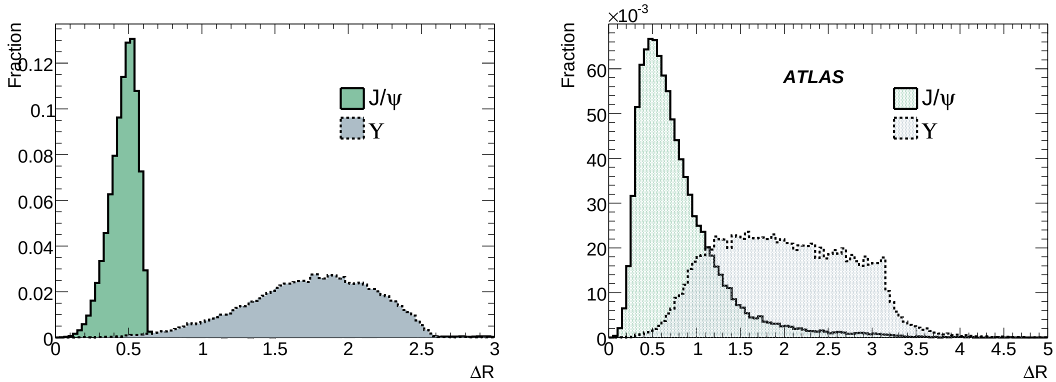

(a) ΔR with $\mu 6\mu 4$ cuts (b) ΔR with $\mu 10$ cuts

Figure 31: Distribution of ΔR separation of the two muons from J/ψ and Υ candidates with di-muon $\mu 6\mu 4$ generator-level cuts (left) and single muon $\mu 10$ cuts (right) applied.

4.1 Background suppression

The main sources of background for prompt charmonium with a di-muon $\mu 6\mu 4$ trigger are:

- Decays in flight of $\pi^{\pm}$ and $K^{\pm}$
- Drell-Yan
- Indirect J/ψ production
- Continuum of muon pairs from beauty (and charm) decays

The sources of low invariant mass di-muons expected to dominate at masses relevant to J/ψ analysis are the irreducible Drell-Yan continuum, indirect J/ψ production (separation of which from the prompt signal is dealt with in Section 4.1.1), and continuum of muon pairs from decays of charm quarks.

The rate of muon pairs from decays in flight in the mass region of interest is expected to be very small. Individual rates for muons from decays in flight and single muon beauty decays are expected to be of the order of microbarns, but require random coincidences in the charmonium invariant mass range. The total possible rate of such sources has been estimated to be of the order of 1% of the signal rate, spread in a continuum. Contributions from charm decays have not been simulated, but despite having an estimated total rate twice as high as from beauty for a $\mu 6 \mu 4$ trigger, as the p_T distributions of muons from charm quarks falls more steeply, charm sources are expected to contribute at a lower level than beauty.

Figure 32 illustrates the main backgrounds and charmonium signal invariant mass distributions in the mass range $2-12$ GeV, for those events satisfying the $\mu 6 \mu 4$ trigger after reconstruction efficiencies have been taken into account. Peaks from the J/ψ and $\Upsilon(1S)$are clearly visible above the background. No higher ψ states were simulated for this analysis (see Table 5 for details of estimated cross-sections of these states).

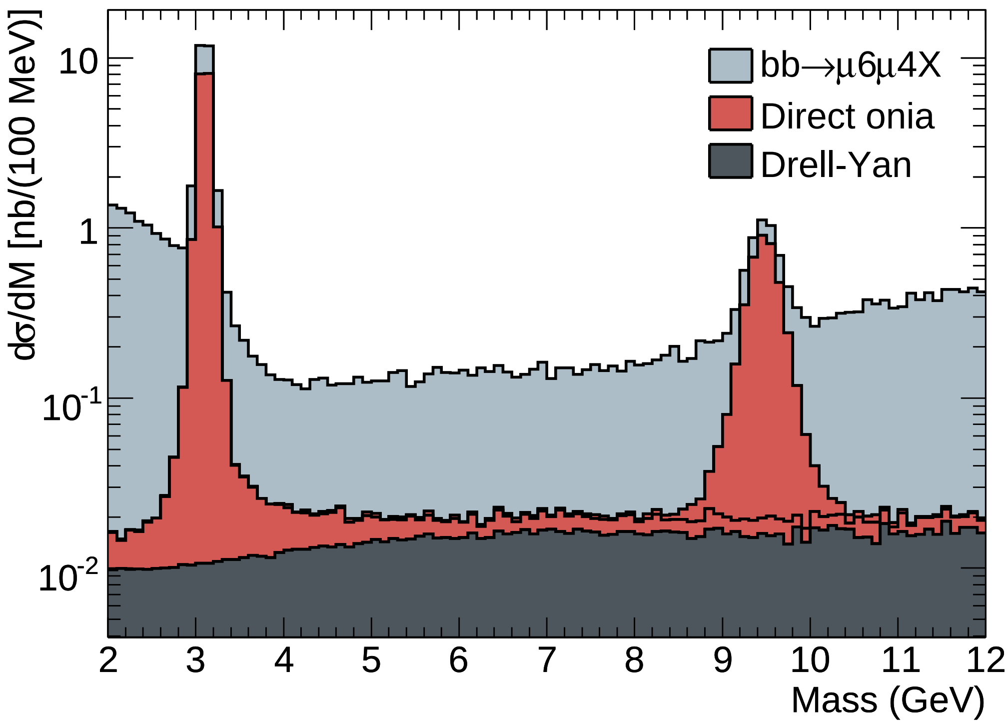

Figure 32: Sources of low invariant mass di-muons, reconstructed with a $\mu 6 \mu 4$ p_T trigger cut, but without any additional cuts.

4.1.1 Separation of prompt and indirect J/ψ

Once two muons forming a candidate J/ψ are reconstructed, the radial displacement of the two-track vertex from the beamline is used to distinguish between prompt J/ψ (which have a pseudo-proper time of zero), and B-hadron decays having an exponentially decaying pseudo-proper time distribution due to the non-zero lifetime of the parent

B-hadrons that may decay into quarkonia. The pseudo-proper time is defined as

$$\text{Pseudo-proper time} = \frac{L_{xy} \cdot M_{J/\psi}}{p_T(J/\psi) \cdot c}, \tag{9}$$

where $M_{J/\psi}$ and $p_T{}^{J}/\psi$ represent the J/ψ invariant mass and transverse momentum, c is the speed of light in vacum, and L_{xy} is the transverse decay length of the meson as shown in Figure 33.

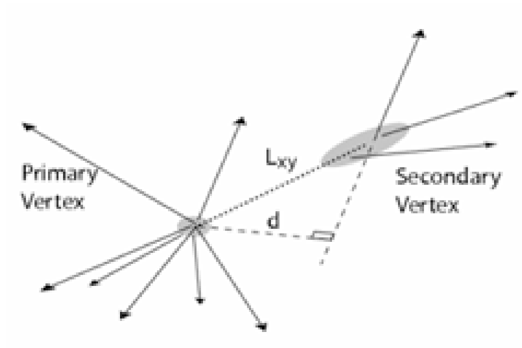

Figure 33: Definition of the Lxy.

The dependence of the resolution in radial decay length L_{xy} on di-muon pseudorapidity η is shown in Figure 34,

The pseudo-proper time (rather than the proper-time) is used because of its better resolution. Figure 35 illustrates the pseudo-proper time distribution for both the prompt and indirect J/ψ samples.

The resolution of the pseudo-proper time of prompt J/ψ mesons is shown in Table 8 in several p_T regions and Table 9 for pseudorapidity regions. As expected, the means for the distributions leading to these resolutions were found to be compatible with zero.

J/ψ transverse momentum (GeV)	$9-12$	$12-13$	$13-15$	$15-17$	$17-21$	>21
Pseudo-proper time resolution (ps)	0.107	0.103	0.100	0.093	0.087	0.068

Table 8: Pseudo-proper time resolution of direct J/ψ events as a function of J/ψ p_T.

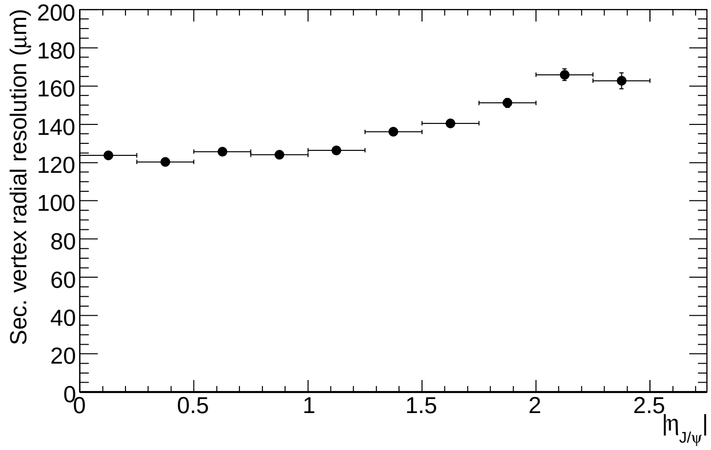

Figure 34: Radial position resolution of secondary vertex for J/ψ decays as a function of the J/ψ pseudorapidity.

J/ψ pseudorapidity	$0-0.8$	$0.8-1.6$	$1.6-2.5$
Pseudo-proper time resolution (ps)	0.087	0.095	0.117

Table 9: Pseudo-proper time resolution of direct J/ψ events as a function of J/ψ pseudorapidity.

An improvement in resolution can be seen with increasing of the J/ψ p_T and decreasing $|\eta|$. Resolution is stable in the barrel region, but gradually gets worse in the high $|\eta|$ region.

A cut on the pseudo proper time can efficiently distinguish between prompt and indirect J/ψ samples. The efficiency and purity of the pseudo-proper time cuts for prompt and indirect J/ψ is presented in Figure 36.

The left plot depicts the efficiency and purity of the pseudo-proper time cut to select direct J/ψ and to reject the indirect sample. Conversely, the right plot displays the efficiency and purity to separate B-decay candidates from the direct J/ψ events. Selecting events with pseudo-proper time cut of ≤ 0.2 ps results in a direct J/ψ sample with an efficiency of 93% and purity of 92%, whilst selecting events with a pseudo-proper time cut of ≥ 0.15 ps yields an indirect J/ψ sample with an efficiency of 80% and purity of 60%.

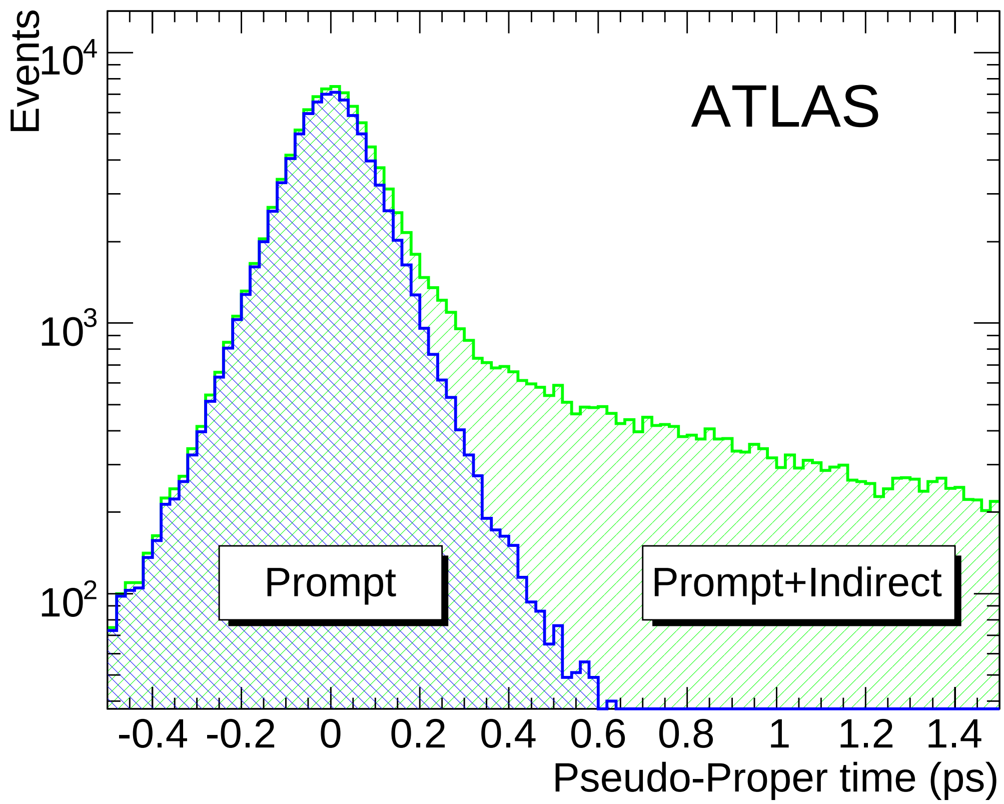

Figure 35: Pseudo-proper time distribution for reconstructed prompt J/ψ (red, centred at zero) and the sum of prompt and indirect J/ψ from B-decays (green, exponential distribution).

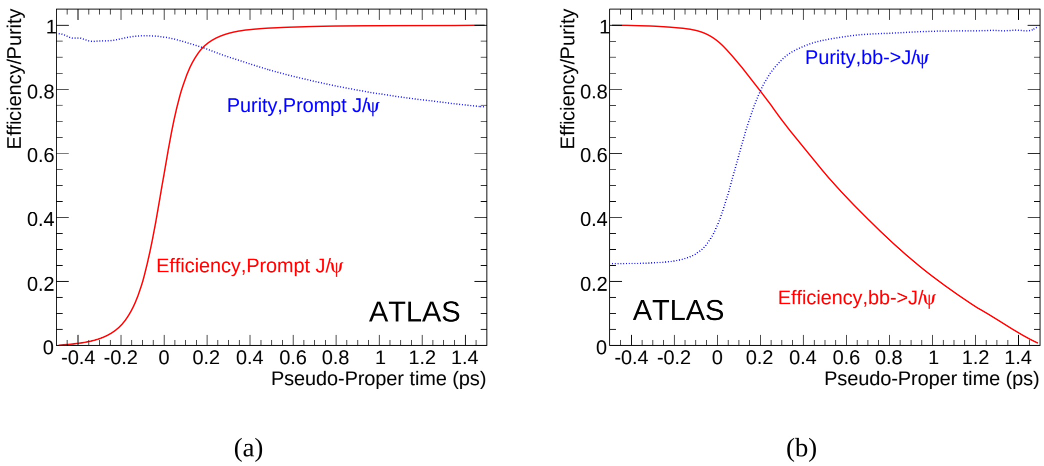

Figure 36: Purity and efficiency measurements for J/ψ pseudo-proper time cuts. (a) Selection the direct J/ψ from the indirect.(b) Selection the indirect J/ψ from the direct. A pseudo-proper time cut of less than 0.2 ps gives prompt J/ψ with an efficiency of 93% and 8% indirect J/ψ contamination. A cut of more than 0.15 ps gives indirect J/ψ with an efficiency of 80% and 40% prompt J/ψ contamination.

Additional flags associated to individual reconstructed muons provide further vertexing information. Reconstructed muon tracks are assigned to either come from the primary vertex, a secondary vertex, or are left undetermined. By requiring that both of the muons combined to form a J/ψ candidate are initiated at the primary vertex, background from the $bb \rightarrow \mu 6 \mu 4$ continuum can be reduced by a factor of three whilst reducing the signal events by around 10%. By using these muon vertex flags in conjunction with a cut of 0.2 ps on the pseudo proper time, we can reduce the backgrounds from Figure 32 to the levels shown in Figure 37.

4.2 Reconstruction and background suppression with a single muon candidate

By using the $\mu 10$ trigger, one selects events with at least one identified muon candidate with p_T above 10 GeV. In this part of the analysis, each reconstructed single muon candidate is combined with oppositely-charged tracks reconstructed in the same event. The identified muon candidate must have a $p_T > 10$ GeV. For J/ψ reconstruction, we insist that any other reconstructed track to be combined with the identified trigger muon has an opposite electric charge and is within a cone of $R = 3.0$ around the muon

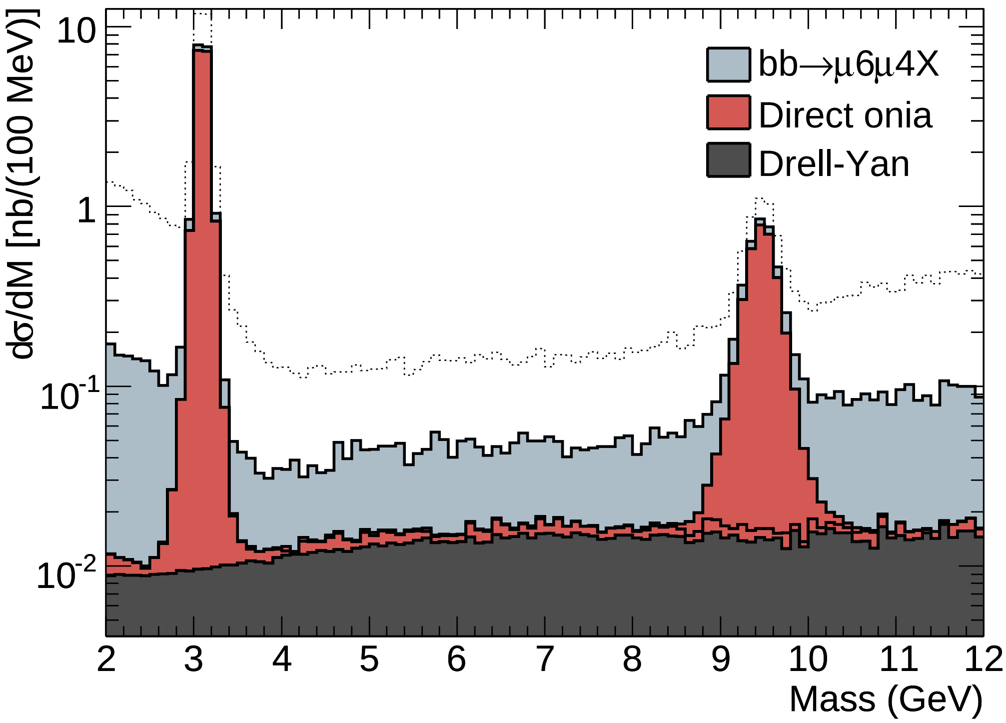

Figure 37: Sources of low invariant mass di-muons, reconstructed with a $\mu 6 \mu 4$ p_T trigger cut, with the requirement that both muons are identified as coming from a primary vertex and with a proper time cut of 0.2 ps.

direction, so as to retain over 99% of the J/ψ signal events. As in the di-muon analysis, we require that both the identified muon and the track are flagged as having come from the primary vertex. In addition, we impose a cut on the transverse impact parameter d_0, $|d_0| < 0.04$ mm on the identified muon and $|d_0| < 0.10$ mm on the second track, in order to further suppress the number of background pairs from B-decays.

The invariant mass distribution for the remaining pairings of a muon and a track is shown in Figure 38(a) for J/ψ with p_T larger than 9 GeV and in Figure 38(b) for J/ψ with p_T larger than 17 GeV. The distributions are fitted using a single gaussian for the signal and a straight line for the background (which now just comprises of the combinatorial background from random muon+track pairs). Clear J/ψ peaks can be seen, with statistically insignificant mass shifts and the resolution close to that in the di-muon sample. It's worth noting that the signal-to-background ratio around the J/ψ peak improves slightly with increasing transverse momentum of J/ψ. At higher p_T the $\cos\theta^*$ acceptance also becomes broader, which should help independent polarisation measurements.

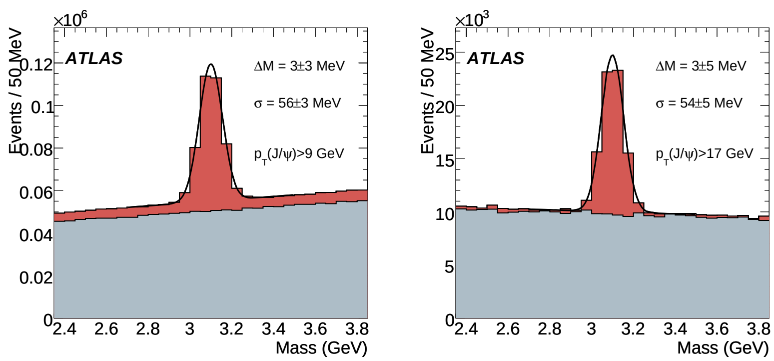

(a) J/ψ @ 9 GeV (b) J/ψ @ 17 GeV

Figure 38: Prompt charmonium signal and $bb \to \mu X$ background events selected with the μ10 trigger, in the mass range around (a) J/ψ with p_T above 9 GeV, (b) J/ψ with p_T above 17 GeV. The background from B decays is shown in grey. Cuts described in the text have been applied.

We expect that the single muon sample will to be useful to select prompt J/ψ events at significantly higher statistics and higher transverse momenta. The expected background is much larger than in di-muon case.

4.3 Summary of cuts and efficiencies

Table 10 summarises the efficiencies of all the selection and background suppression cuts described above, for both the di-muon and single muon trigger samples.

	Trigger type	$\mu 6 \mu 4$	$\mu 10$
	MC cross section	23 nb	23 nb
ε_{L1}	Level 1 trigger	86.6%	*96%*
ε_{L2}	Level 2 trigger	96.6%	*>99%*
ε_{Rec}	Reconstruction	89.2%	*96%*
ε_{Vtx}	Vertex fit	99.9%	*99%*
ε_1	$\varepsilon_{L1} \cdot \varepsilon_{L2} \cdot \varepsilon_{Rec} \cdot \varepsilon_{Vtx}$	74.5%	*90%*
ε_{t0}	Pseudo-proper time cut	93.2%	*93%*
ε_{Flg}	Only primary vertex tracks	96.4%	92%
$\varepsilon_{\Delta R}$	Second track inside cone	n/a	99%
ε_{d0}	Impact parameter cut	n/a	90%
ε_2	$\varepsilon_{t0} \cdot \varepsilon_{Flg} \cdot \varepsilon_{\Delta R} \cdot \varepsilon_{d0}$	89.8%	76%
ε	Overall efficiency $\varepsilon_1 \cdot \varepsilon_2$	67%	69%
	Observed signal cross section	15 nb	16 nb
	N_S for 10 pb^{-1}	150,000	160,000
	N_B in mass window for 10 pb^{-1}	7000	700,000
	Signal/Background ratio	21.4	0.23

Table 10: Predicted and observed cross-sections for prompt charmonia, and efficiencies of various selection and background suppression cuts described in Section 4.

Not all cuts are applicable to all samples; those which are not are labelled accordingly. Numbers in italics are our estimates in cases where no adequate fully simulated sample was available. The efficiencies for $\mu 6 \mu 4$ samples are calculated relative to the Monte Carlo sample with generator level cuts on the two fastest muon transverse momenta of 6 and 4 GeV. For the $\mu 10$ samples, the generator-level cut of 10 GeV was applied to the p_T of the fastest muon.

Expected yields N_S of quarkonia for 10 pb^{-1} are given at the bottom of the table, along with background yields N_B within the invariant mass window of $\pm$300 MeV around the J/ψ mass, and the signal-to-background ratios at the J/ψ mass.

For higher, excited charmonium states with vector quantum numbers the efficiencies are expected to be similar, but not necessarily identical. The biggest differences are expected for ψ', where the production mechanisms as well as decay kinematics are significantly different.

4.4 Analysis of χ production

As mentioned previously, a sizeable fraction of prompt J/ψ are expected to originate from radiative decays of heavier states, χ_c . These states have even C parity and therefore have a strong coupling to the color-singlet two gluon state, thus their dominant production mechanism for the phase space area accessible in ATLAS is via the subprocess shown in Figure 2(b) in Section 1.

Consequently, about 30 to 40 % of J/ψ in our signal come from decays of $\chi_c \rightarrow J/\psi + \gamma$. Unfortunately, the energies of these photons tend to be quite small. The ability of ATLAS to detect these photons and resolve various χ states is analysed in the following.

Reconstructing χ_c candidates requires associating a reconstructed J/ψ with the photon emitted from the χ decay. The transverse energy of all reconstructed photons in events with a prompt J/ψ is shown in Figure 39 (light grey histogram). The photon energies are measured by the ATLAS electromagnetic calorimeter.

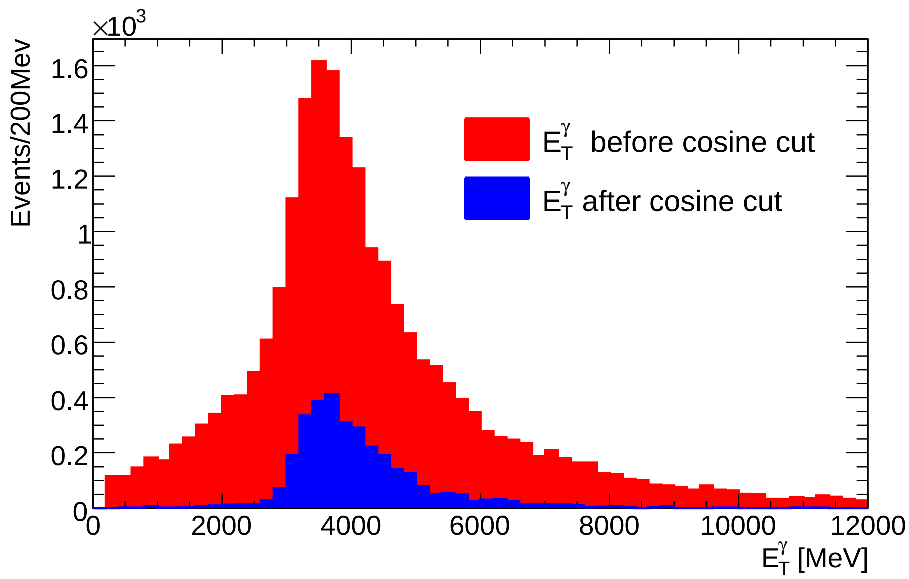

Figure 39: Transverse energy distributions of photons reconstructed in prompt J/ψ events before (red histogram) and after (blue histogram) cuts on the opening angle between the photon and the J/ψ momentum direction.

For χ_c reconstruction, each reconstructed charmonium candidate is combined with every photon reconstructed in the event, and the invariant mass of the $\mu\mu\gamma$ system is calculated using the information from the electromagnetic calorimeter.

The $\mu\mu\gamma$ system is considered to be a χ candidate, if:

- the difference between the invariant masses of the $\mu\mu\gamma$ and $\mu\mu$ systems lies between 200 and 800 MeV, and

- the cosine of the opening angle α between the J/ψ and γ is larger than 0.98.

The last requirement comes from the observation that for the correct $\mu\mu\gamma$ combinations the angle α is usually very small (see Figure 40). From analysis of the mc-truth information it was found that all of the true χ were found in the peak visible very close to $cos(\alpha) = +1$.

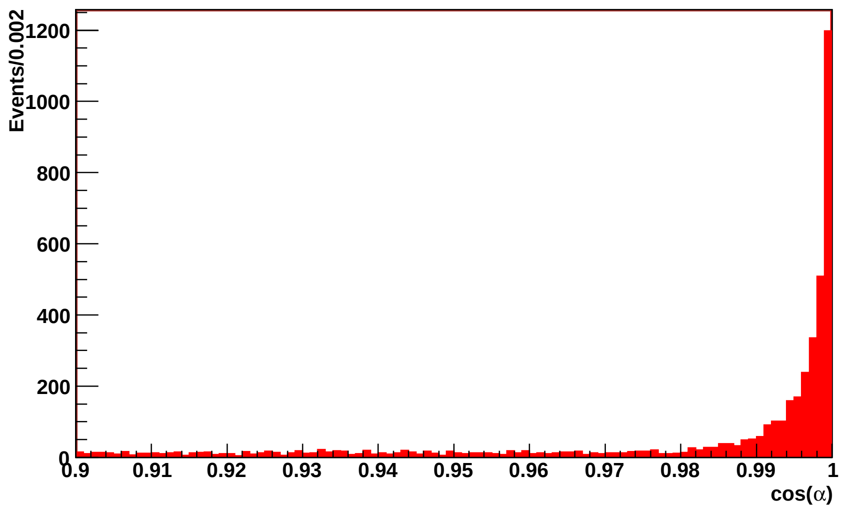

Figure 40: Cosine distribution of the opening angle between the J/ψ momentum direction and each reconstructed γ in an event. True γ originating from $\chi \rightarrow J/\psi\gamma$ decays have a $\cos\alpha > 0.98$ in the reconstructed events.

The transverse energy distribution for those photon candidates which satisfy the above requirements is presented in Figure 39 by the blue histogram. These significantly reduce the combinatorial background but it becomes clear that the efficiency to reconstruct χ in this decay mode using calorimetry is relatively low (as was observed before by the Tevatron results).

Figure 41 shows the distribution in ΔM for the selected χ_c decay candidates. The expected mean positions of the peaks corresponding to χ_0, χ_1 and χ_2 signals are 318, 412 and 460 MeV, respectively. are indicated by arrows. The grey histogram shows the contribution from the background process of J/ψ production from B-hadron decays, some of which survive the pseudo-proper time cut.

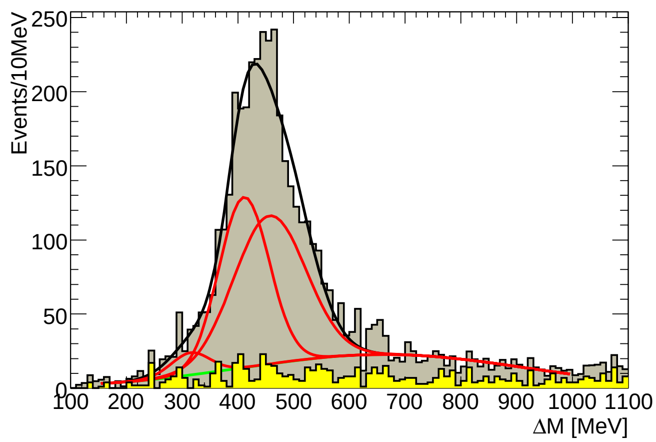

Figure 41: Difference in invariant masses of $\mu\mu\gamma$ and $\mu\mu$ systems in prompt J/ψ events (grey) with $bb \to \mu 6 \mu 4 X$ background surviving cuts (yellow). The lines show the results of the fit described in the text. Event yields correspond to an integrated luminosity of 10 pb^{-1}.

The solid line in Figure 41 is the result of a simultaneous fit to the measured distribution, with the three peak positions fixed at their expected values, and the common resolution function $\sigma(\Delta M)$. The resolution in $\sigma(\Delta M)$ is expected to increase with increasing ΔM. The red lines show the shapes of individual peaks and of the background continuum. The fit parameters are the heights of the three gaussian peaks $h_{\chi 0}, h_{\chi 1}, h_{\chi 2}$, and the three parameters describing the smooth polynomial background. The true amplitudes of the peaks (15, 125 and 90, respectively) are reproduced reasonably well:

$$\begin{aligned} h_{\chi 0} &= 15 \pm 3, \\ h_{\chi 1} &= 115 \pm 5, \\ h_{\chi 2} &= 100 \pm 5, \end{aligned} \tag{10}$$

with a strong negative correlation between the last two. The resolution is found to increase from about 38 MeV at χ_0 to about 60 MeV at χ_2, while the overall reconstruction efficiency of χ_c states is estimated to be about 5%, it may be possible to significantly improve the resolution by using photon conversions (software still in development), but this is unlikely to yield a big increase in efficiency.

4.5 Event monitoring using charmonium

Two streams of the data are running in parallel to to the nominal streams and are dedicated to monitor the detector operations, calibration and data quality check.

The J/ψ will be used in both online and offline monitoring at ATLAS in the express and physics streams. The express stream will contain 10 hours of data which is expected to include around 15,000 J/ψ (with di-muon $\mu4\mu4$ trigger cuts), which will be used for quasi-real time calibration and alignment of the detector. Charmonium mass shifts in a number of different variables can be used to monitor detector alignment, material effects, and magnetic field scale and stability, as well as to provide checks of muon reconstruction algorithm performance. It took many years at the Tevatron to collect sufficient statistics across a range of variables to allow for proper correction for material and alignment and the disentanglement of various detector effects. The expected rate of charmonium production at ATLAS is such that we can expect to be able to perform meaningful monitoring and corrections online and have statistics comparable to that used at CDF for such studies within weeks.

There are many examples of where monitoring of charmonium mass shifts can be useful in data-taking. Mass shifts in charmonia as a function of transverse momentum as in Figure 42 can reveal problems with energy loss corrections and the muon momentum scale. Mass shifts in Monte Carlo charmonia data have already been of used within ATLAS to improve muon reconstruction algorithms.

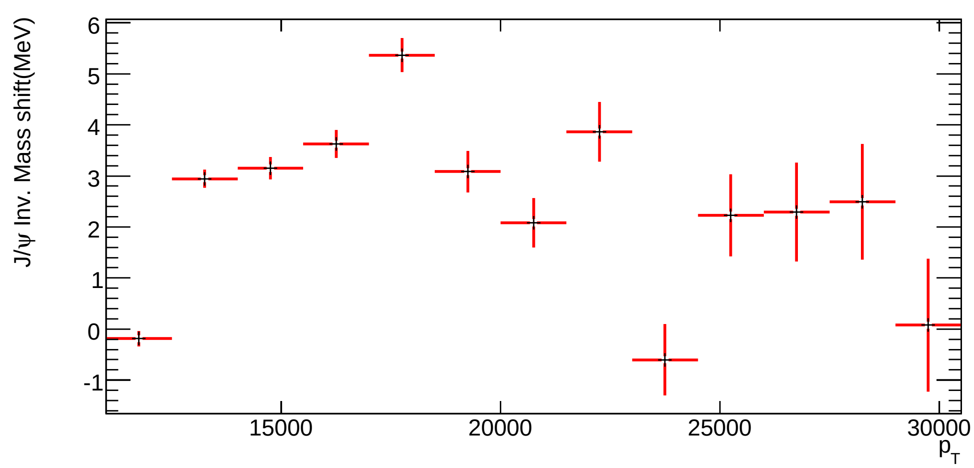

Figure 42: J/ψ mass shift versus p_T

In addition to being crucial for understanding of the detector, analysis of mass shifts on reconstructed Monte Carlo data can also be useful as a cross-check of algorithm performance. Mass shifts in the J/ψ have already been used to find previously unobserved large shifts in the charmonium mass in the forward detector regions (see Figure 43). This problem we found to be due to an overcorrection of the Geant 4 muon energy loss at high η in the muon reconstruction algorithms which is now fixed (the effect of the fix is overlaid in the same figure).

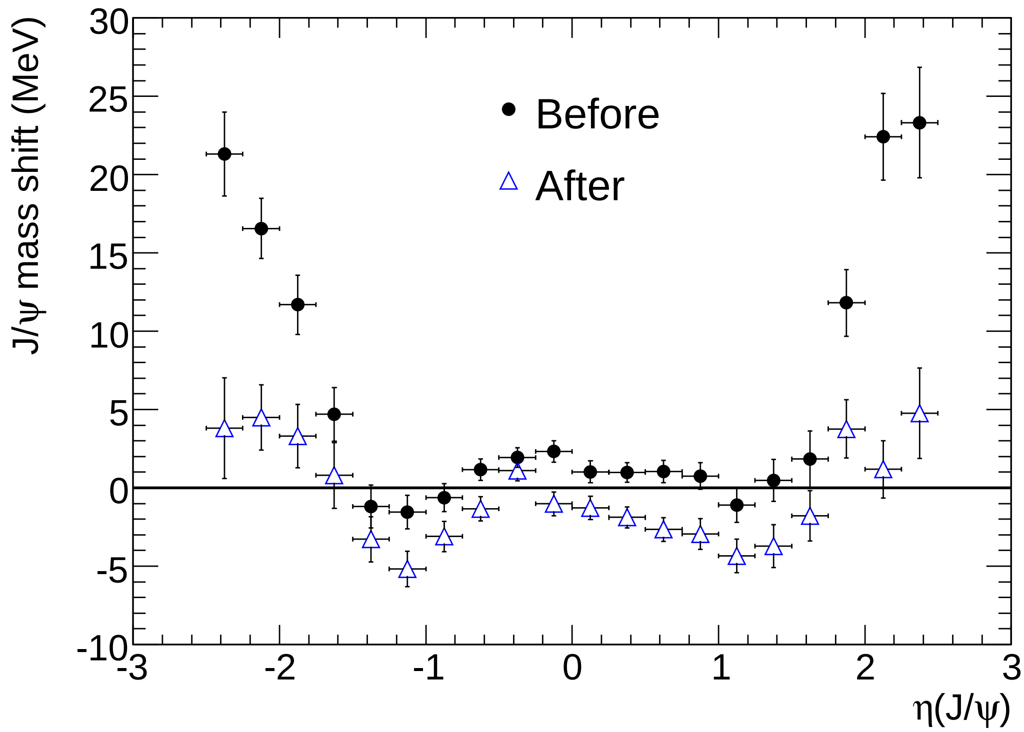

Figure 43: J/ψ mass shift in η before (black dots) and after (blue triangles) correction of muon reconstruction algorithms for Geant 4 energy loss.

An important effect is the mass shift as a function of the difference in curvature of positive and negative muons. This effect was observed before at the CDF experiment. Horizontal misalignments in the detector places result in a constant curvature offset that can lead to significant charge-dependent tracking effects. A misalignment may be such that a negative track has a higher assigned curvature than is truly the case (and hence lower momentum), whilst a positive track would be affected in the opposite way.

Figure 44 shows an example of such a measurement at ATLAS simulation with two weeks worth of simulated data. For detector alignment and data monitoring charmonium provides a complementary low p_T point to the Z, for calibration and allows for the

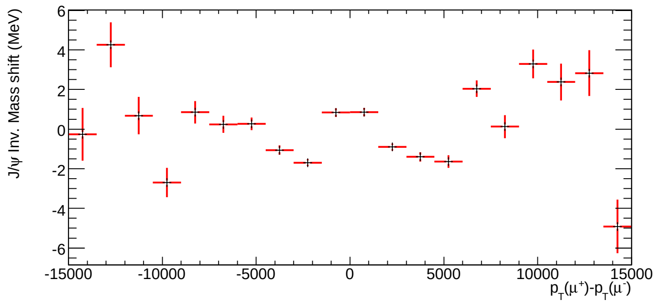

Figure 44: J/ψ invariant mass shift with p_T difference between positive and negative muons.

possibility to identify any systematic variations that may develop at higher p_T's.

5 Spin-alignment studies

The NRQCD model predicts that prompt quarkonia, produced in pp collisions, are transversely polarised, where the polarisation value increases as a function of the transverse momentum of the particle (see Figure 6). Other production models predict different p_T dependencies of the polarisation and so this quantity serves as an important measurement for discrimination between these models.

5.1 Theoretical derivation

This sections describes the derivation of the $(1+\alpha cos^2\theta^*)$ form of the J/ψ angular decay distribution. The derivation presented below applies not just to the decay $J/\psi \rightarrow \mu^+\mu^-$, but to all parity-conserving vector meson decays to spin -1/2 fermion-antifermion pairs. It is based on the analysis in [80], which provides a complete and general discussion of angular distributions in particle decays. To obtain an appropriate coordinate system for analyzing $J/\psi \rightarrow \mu^+\mu^-$ events at ATLAS experiment the relevant independent vectors are:

- the proton momentum $\vec{p}_p$ in the lab frame
- the J/ψ momentum $\vec{p}_{J/\psi}$ in the lab frame
- the μ^+ momentum $\vec{p_\mu}^{J/\psi}$ in the J/ψ rest frame

The production plane is defined by the vectors $\vec{p}_p$ and $\vec{p}_{J/\psi}$. For this analysis, the decay coordinate system $(\hat{x};\hat{y};\hat{z})$ is then defined by the following conditions:

- $\hat{z}$ lies along $\vec{p}_{J/\psi}$
- $\hat{y}$ is the production plane normal, lying along $\vec{p}_p \times \vec{p}_{J/\psi}$
- $\hat{x}$ completes the right-handed coordinate system: $\hat{x} = \hat{y} \times \hat{z}$

Because $\hat{z}$ lies along $\vec{p}_{J/\psi}$, the directions of these unit vectors do not change under boosts between the lab frame and the J/ψ rest frame. Their lengths can be normalized to unity as necessary. The angular distribution of the two-body decay in the J/ψ rest frame is then determined by two angles: the polar angle θ^* and the azimuthal angle ϕ^* of the positive muon.

$$\vec{p_\mu}^{J/\psi} = \left|\vec{p_\mu}^{J/\psi}\right| \cdot (sin\theta^*\, cos\phi^*\, \hat{x} + sin\theta^*\, sin\phi^*\, \hat{y} + cos\theta^*\, \hat{z}) \qquad (11)$$

The decay is analyzed in the helicity basis, in which the $\mu^+ \mu^-$ final state is characterized by the helicities of the muons. The μ^+ and μ^- helicities, λ^+ and λ^-, can each be +1/2 or -1/2. There are thus four conceivable matrix elements for the decay, $M(\pm\frac{1}{2},\pm\frac{1}{2})$. Parity conservation forbids the two for which $\lambda^+ = \lambda^-$ and also implies that $M(+\frac{1}{2},-\frac{1}{2}) = M(-\frac{1}{2},+\frac{1}{2})$ The information on the production polarization of the J/ψ mesons is contained in the density matrix ρ:

$$\rho = \begin{pmatrix} \rho_{11} & \rho_{10} & \rho_{1-1} \\ \rho_{01} & \rho_{00} & \rho_{0-1} \\ \rho_{-11} & \rho_{-10} & \rho_{-1-1} \end{pmatrix} \tag{12}$$

It is Hermitian and satisfies $Tr(\rho) \equiv \rho_{11} + \rho_{00} + \rho_{-1-1} = 1$. The longitudinal and transverse polarization fractions are ρ_{00} and $\rho_{11} + \rho_{-1-1}$ respectively. Since the $\hat{z}$ axis lies in the production plane, parity conservation imposes further constraints on ρ:

$$\begin{aligned} \rho_{-1-1} &= \rho_{11} \\ \rho_{-11} &= \rho_{1-1} \\ \rho_{-10} &= -\rho_{10} \\ \rho_{0-1} &= -\rho_{01} \end{aligned} \tag{13}$$

This reduces the number of independent real parameters in ρ to four. A convenient set is $\rho_{00}, \rho_{1-1}, Re(\rho_{01})$ and $Im(\rho_{01})$ For a given production density matrix, the angular distribution of decays $W(\theta^*,\phi^*)$ is:

$$W(\theta^*,\phi^*) = N \cdot \sum_{\lambda^+,\lambda^-,m,m'} \left|M(\lambda^+,\lambda^-)\right|^2 \rho_{mm'} D^{j*}_{m\lambda}(\theta^*,\phi^*,0) D^{j}_{m'\lambda}(\theta^*,\phi^*,0) \tag{14}$$

Here N is a normalization factor, $\lambda = \lambda^+ - \lambda^-$, j=1 (the J/ψ spin) and the D's are Wigner functions:

$$D^j_{mm'}(\alpha,\beta,\gamma) = e^{-im\alpha} d^j_{mm'}(\beta) e^{-im'\gamma} \tag{15}$$

The d functions are widely used and can be looked up in various sources. They satisfy

$$d^j_{m'm} = (-1)^{m-m'} d^j_{mm'} = d^j_{-m-m'} \tag{16}$$

which allows all the necessary d functions for this calculation to be derived from

$$d^1_{11}(\beta) = \frac{1+cos\beta}{2} \qquad d^1_{10}(\beta) = \frac{-sin\beta}{\sqrt{2}} \qquad d^1_{1-1}(\beta) = \frac{1-cos\beta}{2} \tag{17}$$

Calculating W is then tedious but straightforward algebra; the sum contains 18 terms, encompassing the two possible combinations of (λ^+,λ^-) and the nine possible combinations of (m,m'). The first step is to sum over (λ^+,λ^-) and simplify the Wigner functions:

$$W(\theta^*,\phi^*) \propto \sum_{m,m'} \rho_{mm'} e^{i(m-m')\phi^*} \left(d^1_{m1}(\theta^*) d^1_{m'1}(\theta^*) + d^1_{m-1}(\theta^*) d^1_{m'-1}(\theta^*) \right) \tag{18}$$

Writing out the d functions and substituting out all the redundant elements of ρ, the eventual result is:

$$W(\theta^*,\phi^*) \propto \frac{1+\rho_{00}}{2}(1+\frac{1-3\rho_{00}}{1+\rho_{00}}cos^2\theta^*)+\rho_{1-1}cos2\phi^*(1-cos^2\theta^*) \\ +\sqrt{2}Re(\rho_{01})cos\phi^* sin2\theta^* \quad (19)$$

With the change of variable $\alpha = \frac{1-3\rho_{00}}{1+\rho_{00}}$ the first term becomes the familiar expression $\frac{2}{\alpha+3}(1+\alpha cos^2\theta^*)$. The other two terms depend on $cos2\phi^*$ and $cos\phi^*$, which both vanish when integrated over ϕ^*. In the polarization analysis, the data and Monte Carlo samples are always integrated over ϕ^* so these two terms are ignored.

5.2 Polarization measurements

In general, polarisations can be measured using the angular distribution of the daughter particles produced in the particles decay.

The polarisation determines the distribution of the decay angle (as showed in the previous section)

$$\frac{d\Gamma}{d\cos\theta^\star} = \frac{C}{\alpha+3}\cdot(1+\alpha\cos^2\theta^\star). \quad (20)$$

The quantity $\cos\theta^\star$ varies between -1 and $+1$; where a factor $C/(\alpha+3)$ is used to normalise the distribution to a unit. The polarisation parameter α, defined as $\alpha = (\sigma_T - 2\sigma_L)/(\sigma_T + 2\sigma_L)$, is equal to $+1$ for transversely polarised production, where transverse polarisation refers to helicity ± 1. For longitudinal (helicity 0) polarisation α is equal to -1. Between these two extremes lies a mixture of transverse and longitudinal production. Unpolarised production consists of equal fractions of helicity states $+1$, 0 and -1, and corresponds to $\alpha = 0$.

Attempts to measure the polarisation of charmonia have been made at CDF. They suffered from low $|\cos\theta^\star|$ acceptance, and hence from difficulties in separating detector efficiency corrections from polarisation state effects. Additionally, feed-down from χ states and B-decays dilute the prompt sample and lead to an effective depolarisation which is difficult to measure. In particular, data from the Tevatron is limited to below around 20 GeV where the polarisation is best predicted and the theory most understood.

Figure 45(b) shows the measured $\cos\theta^\star$ distribution from CDF for J/ψ decays in the region $7 \leq p_T(\text{ GeV}) < 9$.

At ATLAS we aim to initially measure the polarisation of directly produced mesons only and extend this measurement up to the high p_T region ($\sim$ 50 GeV) with extended coverage in $\cos\theta^\star$. This will allow for reduced systematics. Better discrimination of longitudinal and transverse polarisations (which have their largest differences at high $|\cos\theta^\star|$) and improved fidelity of efficiency measurements for single and di-muons disentangled from the polarisation state. In the J/ψ case, the promptly produced mesons

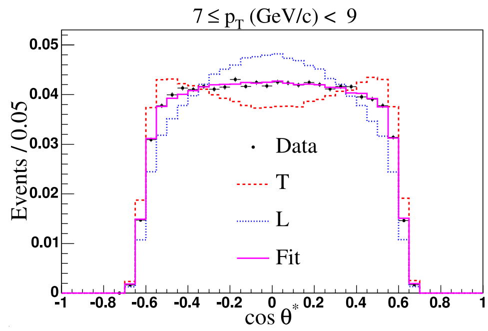

(a) $\cos\theta^\star$ distribution CDF

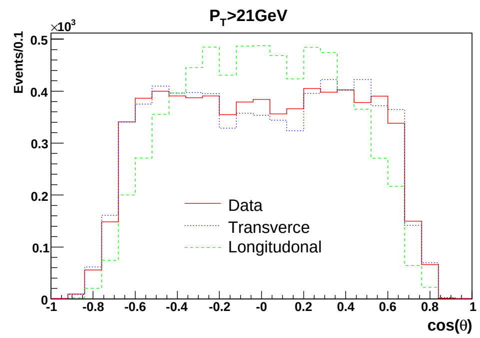

(b) $\cos\theta^\star$ distribution MC-ATLAS

Figure 45: An example of the $\cos\theta^\star$ distribution seen for J/ψ in CDF data [56] in the $7 \leq p_T(\text{ GeV}) < 9$ region and and the MC-data from ATLAS simulation along with MC templates for longitudinal and transverse polarisations.

and those that originated from B-hadron decay can be separated using the displaced decay vertices characteristic of the latter. With a high production rate of quarkonia it would be possible to insist on a significantly higher purity of J/ψ in the analysed sample to reduce the depolarisation effect from B-decays whilst still retaining high statistics.

Several effects affect the polarization measurement. The first is the dependence of the detector acceptance with respect to $\cos\theta^\star$. For example, in a decay with a large value of $\cos\theta^\star$, one muon emerges nearly in the same direction as the quarkonia, but the other is emitted almost backwards and so has a low momentum in the lab frame. With a di-muon trigger signature such as $\mu6\mu4$, the second muon with a low transverse momentum is likely to fail the trigger or the selection requirements. Therefore, the events with large values of $|\cos\theta^\star|$ have significantly lower probability of entering the data sample.

In Section 3.4.3 the acceptance of $\cos\theta^\star$ with a di-muon trigger was presented and shown to be similar to the situation observed at the Tevatron, with low acceptance beyond values larger than ±0.6. Figure 49 presents the distribution of $\cos\theta^\star$ for the di-muon $\mu6\mu4$ trigger in six p_T slices of $9 \leq p_T(\text{ GeV}) < 12$, $12 \leq p_T(\text{ GeV}) < 13$, $13 \leq p_T(\text{ GeV}) < 15$, $15 \leq p_T(\text{ GeV}) < 17$, $17 \leq p_T(\text{ GeV}) < 21$ and $p_T \geq 21$ GeV respectively. Solely due to the decay kinematics we see that as the transverse momentum of the J/ψ increases we accept a greater region of the distribution, from a maximum of 0.5 at the lowest p_T's to over 0.8 at high p_T. In all cases we see that the distribution suffers from an acceptance distribution identical to what would be expected if the sample had longitudinal polarisation (the sample is actually unpolarised). Clearly this is a problem, and is likely to be a source of systematic error in the Tevatron results.

5.3 Templet fit method

The J/ψ polarization is measured using a chi-squared fit to the $cos^2\theta^\star$ distribution in the MC-data sample. The MC-data events are histogrammed in cos $cos^2\theta^*$. The distributionse are ploted on Figure 49 in six bins of p_T , a MC longitudinally polarized sample (dash-dotted green), a MC transversely polarized sample (dashed blue) and a MC-data sample (solid red). As one can see from these plots, it is not trivial to measure

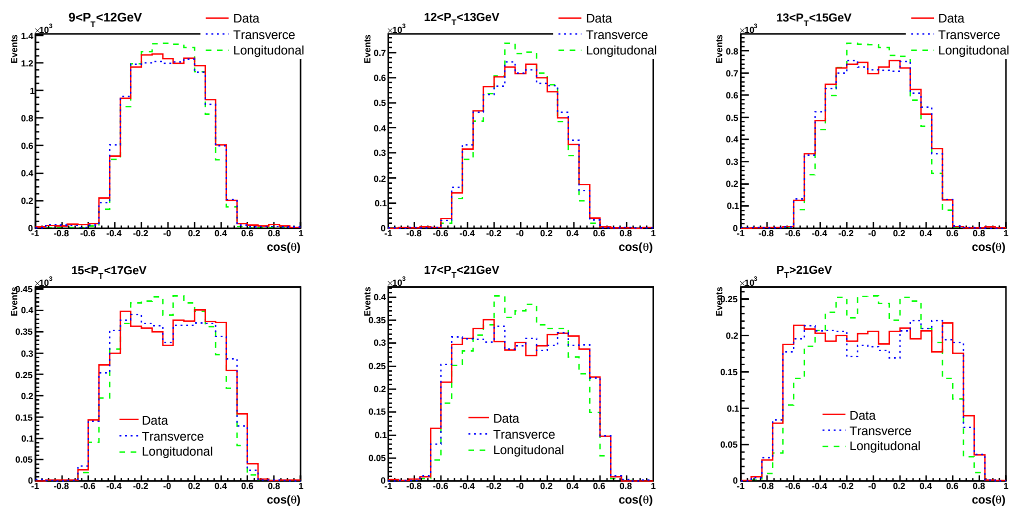

Figure 46: Distribution of $\cos\theta^\star$ for J/ψ ($\mu 6 \mu 4$) in slices of J/ψ transverse momentum.Statistics correspond to about 5 pb^{-1} for the MC-Data sample and to about 5 pb^{-1} for the MC-templates.

the polarization parameter from the usual fit on the MC-data sample ,colored in red. The data points that are not effected from the acceptance of the detector (as explained in the Section3.4.3) are concentrated in a number of bins near $cos^2\theta^\star = 0$. At higher p_T range that number of bins is increased. This enables to perform usual fit of the angular distribution to the theoretical predicted formula. Nevertheless, at higher p_T ranges the number of direct J/ψ drastically fall from few tens of thousand events in the first p_T bin ($9 < p_T < 12GeV$) to few hundreds events in the last p_T bin ($p_T > 21GeV$) (with the statistics of $10pb^{-1}$). We chose to use the "template fit" method where the Monte Carlo samples are used as reference based on histogram templates of $cos^2\theta^*$ distributions. A MC-data histogram is fitted to a sum of three Monte Carlo templates: one for a longitudinally polarized sample second for a transversely polarized sample and third is for background events sample. Longitudinal and transverse Monte Carlo samples were generated with the same number of events, after the acceptance was applied. Therefore the fitted weighting between the longitudinal and transverse templates yields the transversal fraction β, and hence the polarization parameter α is given by the following (Equation 21).

$$\alpha = \frac{2-3\beta}{\beta-2} \tag{21}$$

The background events sample was generated with zero polarization ($\alpha = 0$) using the same detector acceptance effects as in the MC-data sample. The Monte Carlo samples generated are large enough, so that statistical fluctuations in the templates are negligible. The χ^2, showed in the following equation function was build as a sum over the four data samples.

$$\chi^2 = \sum_i^N \frac{(D_i - (\beta \cdot T_i + (1-\beta) \cdot L_i) \cdot N_1 - B_i \cdot N_2)^2}{D_i + (\beta^2 \cdot T_i + (1-\beta)^2 \cdot L_i) \cdot N_1^2 + B_i \cdot N_2^2} \tag{22}$$

In that equation the notation is the following:

- D-is the measured MC-data sample
- T-is the transversally polarized template
- L-is the longitudinally polarized template
- B-is the background sample
- $N_{1,2}$ - are the Normalization parameters

Figure 47 shows the χ^2 distributions (expalined above) in six p_T ranges as a function of the transversaly fraction β. By looking at the parameter β where the χ^2 function reach its minimum value we got the polarization parameter α and its error. The measured values of α in six bins of p_T are presented in Figure 48. As one can see from this plot the average polarization is well concentrated around $\alpha = 0.5$, which is the initial value of polarization that was set in MC-data sample.

5.4 Alternative method

As explained in Section 3.4.3, with the di-muon trigger signature such as $\mu6\mu4$, the acceptance at large values of $|\cos\theta^{\star}|$ (where the difference between various polarisation states is the biggest) is strongly reduced, especially at low transverse momenta of charmonium. The kinematic acceptance $\mathscr{A}(p_T, \cos\theta^*)$ of the $\mu6\mu4$ cuts applied at the generator level, with respect to the full generator level sample with no cuts on muon transverse momenta, is shown with solid red lines in Figure 49 for various p_T slices of J/ψ .

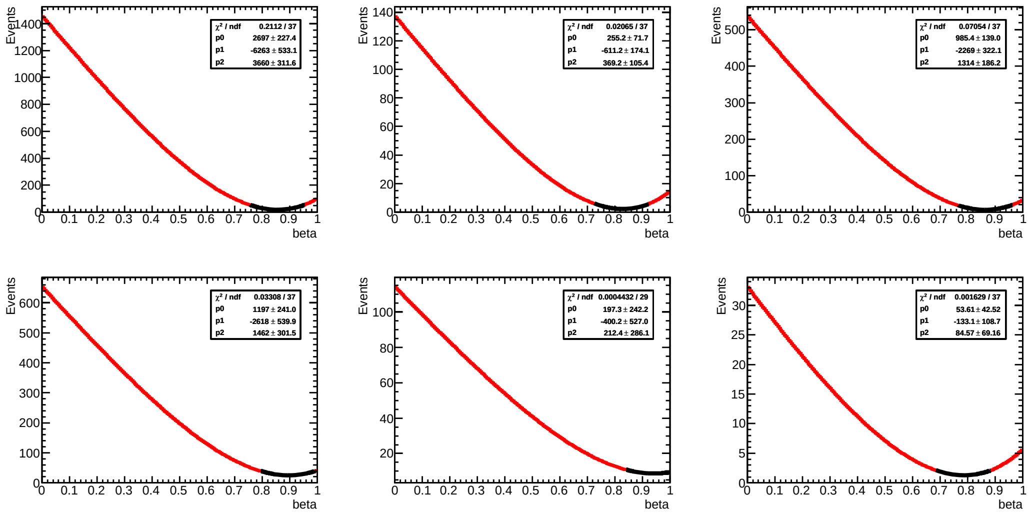

Figure 47: The χ^2 distributions in six bins of p_T.

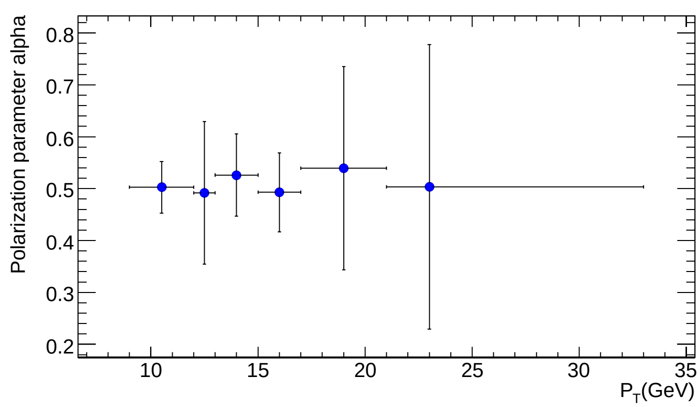

Figure 48: The measured polarization parameter α and its error in six p_T bin. The initial polarization of $\alpha = 0.5$ was set to the MC data sample. Statistics correspond to about 5 pb^{-1}.

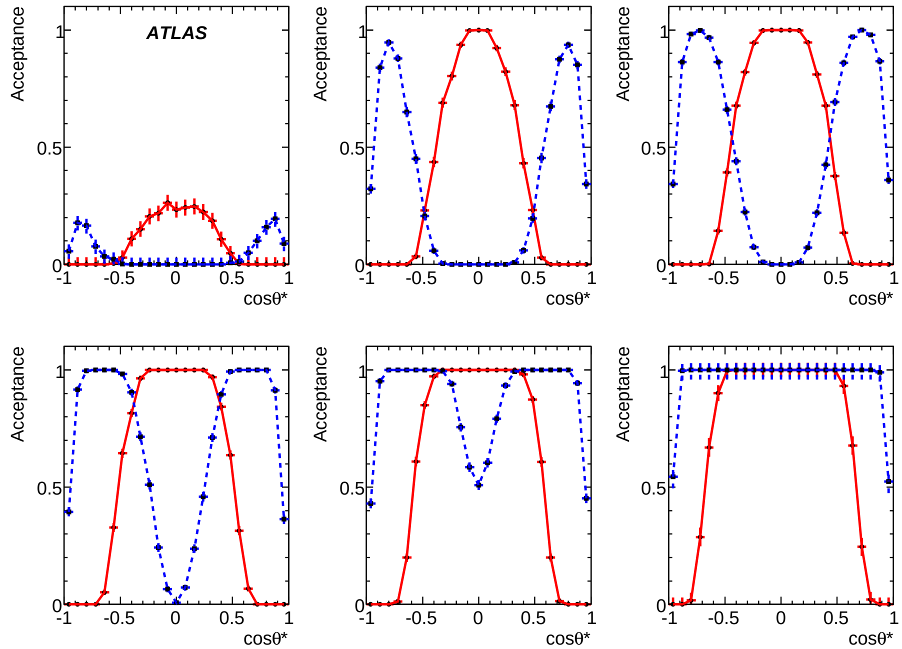

Figure 49: Kinematic acceptances of the $\mu6\mu4$ (solid red lines) and $\mu10$ (dashed blue lines) generator level cuts, calculated with respect to the sample with no generator level cuts on muon p_T, in slices of J/ψ transverse momentum: left to right, top to bottom $9-12$ GeV, $12-13$ GeV, $13-15$ GeV, $15-17$ GeV, $17-21$ GeV, above 21 GeV.

The acceptance is seen to be quite low at J/ψ p_T below 12 GeV, but in higher p_T slices there is an area in the middle of $\cos\theta^*$ range with essentially 100% acceptance, which becomes broader with increasing p_T of the J/ψ , but does not go beyond $|\cos\theta^*| \simeq 0.5$.

The acceptance for the single muon ($\mu10$) trigger sample, shown with the dashed blue lines in Figure 49, is different: here the areas of 100% acceptance are at high $|\cos\theta^*|$, and the dip in the middle gradually fills up with increasing p_T. This sample essentially has a full acceptance at $p_T > 20$ GeV, apart from the drop at $|\cos\theta^*| > 0.95$ due to the cut of 0.5 GeV on the p_T of the track of the second muon.

The plots in Figure 49 were obtained using a dedicated generator-level Monte Carlo sample. The error bars shown in the figure reflect both statistical errors and the uncertainties due to possible dependence on the η coverage.

The simulated "raw" measured distributions $dN^{\rm raw}/d\cos\theta^*$, for the same slices of J/ψ transverse momenta, are shown in Figure 50. Again, solid red and dashed blue lines represent the events selected by the di-muon $\mu6\mu4$ and the single muon $\mu10$ triggers, respectively. The sample was generated with zero polarisation. The raw numbers

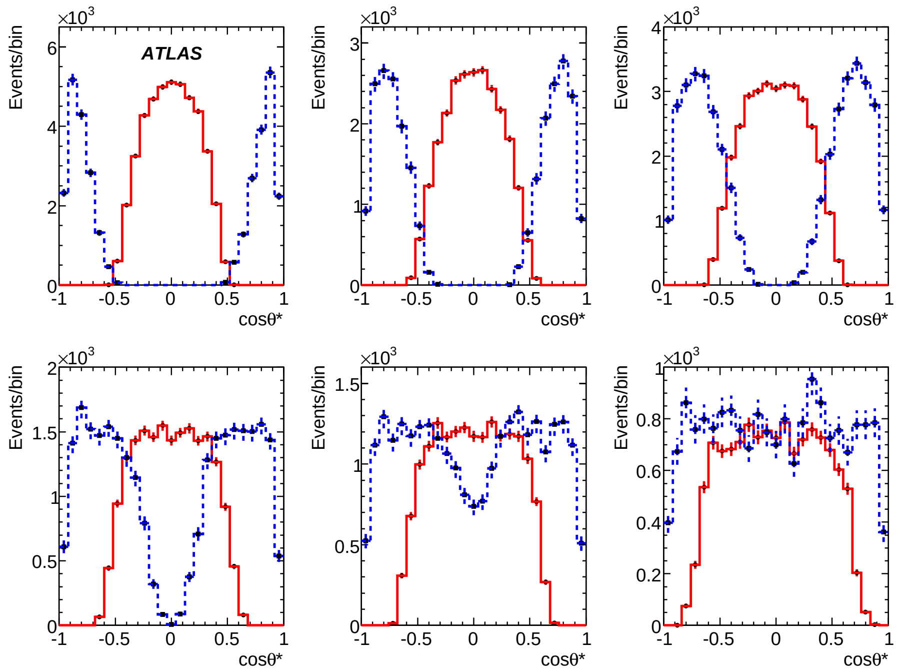

Figure 50: Measured distributions for $\mu6\mu4$- (solid red lines) and $\mu10$- (dashed blue lines) triggered events, in the same p_T slices of the J/ψ candidate as in Figure 49. The simulated data sample is unpolarised. Statistics correspond to 10 pb^{-1}.

of measured events in the $\mu10$ sample were obtained by fitting the invariant mass distributions with a gaussian peak and a linear background, for each bin of $\cos\theta^*$ in each p_T slice. With the estimated signal-to-background ratios shown in Figure 38(a), this causes an increase in the statistical errors, typically by a factor of 2.

In this case the corrected distributions $dN^{\mathrm{cor}}/d\cos\theta^*$ are calculated according to the following formula:

$$\frac{dN^{\mathrm{cor}}}{d\cos\theta^*} = \frac{1}{\mathscr{A}(p_T,\cos\theta^*)\cdot\varepsilon_1\cdot\varepsilon_2}\cdot\frac{dN^{\mathrm{raw}}}{d\cos\theta^*} \tag{23}$$

Here ε_1 stands for the trigger and reconstruction efficiency, while ε_2 denotes the efficiency of background suppression cuts for each sample, as defined in Table 10. Their values have been averaged over the accessible phase space within the relevant p_T slice. Studies have shown that while ε_1 depend on p_T (cf. Figure 30(a)), ε_2 remain essentially constant over the phase space of interest. The efficiencies ε_1 and ε_2 for both samples are listed in Table 11, while the acceptances $\mathscr{A}(p_T,\cos\theta^*)$ are shown in Figure 49.

p_T, GeV	$9-12$	$12-13$	$13-15$	$15-17$	$17-21$	>21
$\varepsilon_1(\mu6\mu4)$, %	67 ± 1	75 ± 1	77 ± 1	78 ± 1	79 ± 1	80 ± 1
$\varepsilon_2(\mu6\mu4)$, %	90 ± 1	90 ± 1	90 ± 1	90 ± 1	90 ± 1	90 ± 1
$\varepsilon_1(\mu10)$, %	86 ± 1	89 ± 1	90 ± 1	90 ± 1	90 ± 1	90 ± 1
$\varepsilon_2(\mu10)$, %	76 ± 1	76 ± 1	76 ± 1	76 ± 1	76 ± 1	76 ± 1

Table 11: Efficiencies for the $\mu6\mu4$ and $\mu10$ samples, averaged over each of the six p_T slices.

At high p_T the two samples ($\mu6\mu4$ and $\mu10$) increasingly overlap, thus allowing for a cross-check of acceptance and efficiency corrections. However, for measurement purposes the $\mu6\mu4$ samples are used whenever possible, complemented by $\mu10$ samples at high $\cos\theta^*$. In order to achieve this, the distributions shown in Figure 50 were appropriately masked and combined. The combined distributions $dN^{\text{cor}}/d\cos\theta^*$, corrected according to Equation 23, are shown in Figure 51. The errors shown in the plots include the statistical errors on the raw data, as well as the uncertainties on the acceptance and efficiencies. These $\cos\theta^*$ distributions are fitted using Equation 20, with α and C as free parameters for each p_T slice. The disadvantage of this method is that it requires higher statistics to perform polarization measurement than the ”template fit” method does.

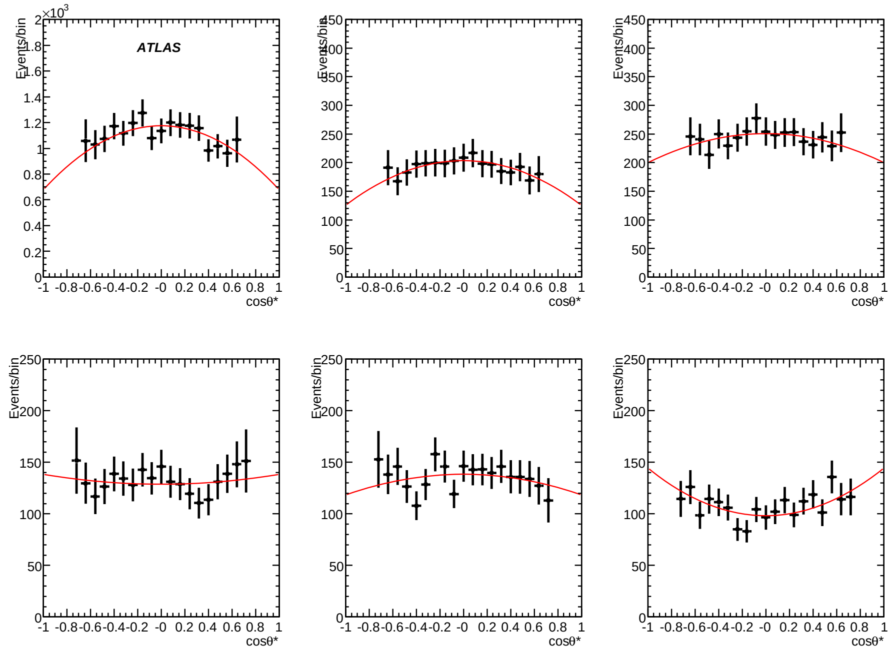

Figure 51: Combined and corrected distributions in J/ψ polarisation angle $\cos\theta^*$, for the same p_T slices as in Figure 49. The data sample is unpolarised. Statistics correspond to 10 pb^{-1}.

6 Systematics uncertainties

In this section we list the various potential sources of systematics and evaluate the approximate values of uncertainties in polarization measurements. It is obvious that the exact values of these parameters would be determined only when ATLAS (LHC) start to take data. The current evaluation of the systematics are based only on simulation studies. The systematic uncertainties were defined in each p_T interval as the difference between the measured α without any expected uncertainty and the α value derived with uncertainty in a specific parameter applied. These uncertainties are summarised in Table 12.

The J/ψ polarization was calculated assuming that α is a constant for a given p_T bin. To estimate the uncertainty due to this approximation, the bias error in the polarization parameter α was calculated according to the expected uncertainty in the initial α of the MC-data sample. It is shown in the first row of the Table 12.

We do not know exactly the ratio between the signal (directly produced $J/\psi \rightarrow \mu^+\mu^-$) and the background (mainly indirect $B \rightarrow J/\psi \rightarrow \mu^+\mu^-$). The estimated ratio and its uncertainty included in our MC studies (see also Appendix A.1 and /,/citeLow-pTmuonnote, are extrapolation of the Tevatron measurements at lower energy. Using this information we vary the signal to background (S/B) ratio and measure the expected uncertainty in the polarization parameter α due to that effect. The results are given in the second row of the Table 12.

Currently the trigger efficiency and purity is hard to estimate. We introduce a trigger efficiency uncertainty of 5 %. In our polarization systematic studies the effect of that levelof uncertanty in both Level 1 and Leval 2 trigger efficiensies is demonstrated on the third and forth rows of the Table 12.

The background rejection study (shown in the Section 4.1.1) gives us an estimation of the amount of indirect J/ψ that survive the rejection criteria and effectively change the measured polarization. By inserting the expected uncertainty in the Pseudo-Proper time measurement, we estimate the uncertainty in the polarization parameter α due to the resolution of the secondary vertex measurement. The result of this study is shown in the fifth row of the Table 12.

Our knowledge of the ratio between the directly produced J/ψ and the J/ψ which comes from the higher charmonium stares $\chi_{c0,1,2}$ decays is limited. The expected values of the χ_c rejection are shown in the Section 4.4. By inserting this (χ_c rejection) uncertainty in the polarization measurements algorithm we estimate the the uncertainty in the polarization parameter α due to the existence of unpolarized J/ψ in the signal sample. The result of this study is shown in the sixth row of the Table 12.

As we saw in our reconstruction studies (presented in the Sections 4 and 4.5) the offline reconstruction algorithms and as a result the polarization measurements depend on the kinematic, on the pseudorapidity and the invariant mass. To estimate the uncertainty in the polarization parameter of direct J/ψ , we insert the expected uncertainties in these values. The results of the study are shown in the seventh and eight rows of the Table 12.

As presented in the Sections 4, the polarization measurement depends on the momentum measurement resolution. By inserting the expected uncertainties in the momentum measurements (along the x,y,z axis), we estimate the uncertainties in the polarization parameter α . Its impact is shown in the last row of the Table 12.

J/ψ transverse momentum (GeV)	$9-12$	$12-13$	$13-15$	$15-17$	$17-21$	>21
$\Delta\alpha$ theoretical uncertainties						
α variation	0.01	0.03	0.05	0.05	0.08	0.1
$B\rightarrow J/\psi$ cross-section uncertainty	0.05	0.05	0.05	0.07	0.1	0.11
$\Delta\alpha$ trigger resolution uncertainties						
LVL1 efficiency	0.3	0.15	0.005	0.005	0.01	0.01
LVL2 efficiency	0.3	0.1	0.08	0.05	0.02	0.02
$\Delta\alpha$ background rejection uncertainties						
Indirect J/ψ separation	0.21	0.2	0.2	0.2	0.2	0.1
χ_c rejection	0.01	0.005	0.002	0.03	0.02	0.02
$\Delta\alpha$ detector resolution uncertainties						
Eta acceptance	0.18	0.04	0.04	0.015	0.01	0.01
J/ψ Inv. mass	0.03	0.03	0.02	0.02	0.02	0.02
Momentum resolution	0.01	0.12	0.05	0.04	0.11	0.28

Table 12: Systematics uncertainties in measuring the polarization parameter α of the direct J/ψ events as a function of the J/ψ p_T (Statistics correspond to 5 pb^{-1}).

The table above is based on studies of simulation with the number of event generated equivalent to 5 pb^{-1} of data. The errors are expected to improve significantly with the increase of the data sample. Looking on the table above it is clearly seen that different sources of systematic dominate the error in different p_T regions. While the main contribution to systematic uncertainty in the low p_T region is expected to come from the trigger uncertainty, the main contribution in higher p_T regions are a result of our poor knowledge in the $B\rightarrow J/\psi$ cross-section and the momentum resolution effect which increases with the increase in p_T. All the values stated here are a rough estimate that would certainly change a lot once the detector will start to collect real data. A detailed comparison between data and Monte Carlo is required in order to get a precise evaluation of the systematic uncertainty of this measurement.

7 Summary

During the initial run of the LHC with the luminosity of 10^{31} cm^{-2} s^{-1}, one day of running roughly corresponds to the integrated luminosity of 1 pb^{-1}. The low luminosity of the early LHC runs will allow to keep a low muon p_T threshold, which will enable us to collect a large fraction of the J/ψ produced in the pp collisions.

With the $\mu 6 \mu 4$ trigger, this would translate to about 15,000 $J/\psi \to \mu\mu$ recorded events. If the $\mu 4 \mu 4$ trigger is used, this number would increase to about 17,000 , with these additional events mainly concentrated at the lower end of the charmonium transverse momenta. All these events should be perfectly useable for detector alignment, acceptance and trigger efficiency, as well as, understanding the tracking of the inner detector and the muon system performance.

At the integrated luminosity of about 10 pb^{-1}, recorded statistics of $J/\psi \to \mu\mu$ with the $\mu 6 \mu 4$ trigger will be roughly equal to the statistics used in this thesis. Arguably, this should be enough to make first measurements of the cross-sections, p_T and η distributions and measurement of the spin alignment of J/ψ as a function of their transverse momenta. At early stage, first attempts may be made to understand the performance of the electromagnetic calorimetry at low photon energies, and to try to reconstruct χ_c states from their radiative decays.

The Tevatron is currently the only proton proton accelerator which reached energy close to that expected at the LHC. The data collected at the Tevatron contradicted the QCD based (CSM) predictions for directly produced onia cross-section. Following its analysis the models were tuned to meet the cross-section measurements. However this has opened a discrepancy between the Non Relativistic QCD modified predictions for the direct onia polarization p_T dependence. CDF has measured the J/ψ polarization p_T dependence and both CDF and D0 measured it in the Υ channel. There are disagreements between CDF and D0 as well as disagreement with the NRQCD predictions. On top of LHC increased number of events it has an additional advantage of reaching higher p_T region allowing measurement in the regime which is more sensitive to the differences between the various theoretical predictions. Therefore we show in this thesis that we expect to signicantly improve the previous measurements and try to improve our understanding of the strong coupling theory at that energy scale. The measurement strongly depends on our tracking and low p_T muon triggering understanding. Two competitive triggering approaches are described in this analysis (the so called $\mu 6 \mu 4$ and $\mu 10$ methods). It is shown that the two methods are complementary, on one hand in the higher p_T region they provide a cross check one to each other and on the other hand in the lower p_T region they are complementary since they have a very small overlap. It is suggested to combine the two approaches for a complete understanding of the effect.

By the end of the year, with the expected integrated luminosity of 100 pb^{-1}, the transverse momentum spectra are expected to reach about 100 GeV and possibly beyond. With several million $J/\psi \to \mu\mu$ decays, and (hopefully) good understanding of the detector, $\chi_c \to J/\psi\gamma$ should become observable, while other measurements mentioned above will become increasingly precise.

During the future high luminosity runs, we will have to increase the trigger threshold, and rescale the lower trigger threshold. Nevertheless the higher luminosity will further expand the range of reachable transverse momenta, and allow further tests of the production mechanisms and the polarization measurements, as well as make χ_c reconstruction easier.

A Appendix

A.1 PYTHIA generation of heavy quarkonium

The PYTHIA program can be used to generate high-energy physics events, i.e. sets of outgoing particles produced in the interactions between two incoming particles. The objective is to provide as accurate as possible a representation of event properties in a wide range of reactions, within and beyond the Standard Model. This is implemented with emphasis on those events where strong interactions play a role, directly or indirectly, and therefore multihadronic final states are produced. Since our theoretical knowledge here is rather limited the program is based on a combination of analytical results and various QCD-based models. In the following Appendix it is described the usage of PYTHIA for generation of heavy quarkonium events within ATLAS computer framework including the reconstruction and analysis environment [81]. It also describes direct J/ψ event generation with PYTHIA simulation code in recent versions and the new showering model presented in PYTHIA and the differences between previous and more recent versions of this Monte Carlo (MC) code. The "`Pythia i`" package provides tools for generating particles using PYTHIA as the generator code and job controle file as the controller. It is described the modiffcations and additions introduced in these PYTHIA releases and required changes to the users initialisation parameters. The major change from PYTHIA release 6.3 and above is the introduction of a new underlying-event framework for hadronic collisions and new transverse momentum ordered initial (ISR) and final (FSR) state parton showers with an associated set of new tuning parameters. An important modification relevant from our point of view is the addition of new J/ψ and Υ channels in the NRQCD COM framework.

A.2 Implementation of color-octet processes in PYTHIA

color-octet simulation has recently become available as standard in PYTHIA and currently implements the leading order diagrams in α_s for quarkonium production in both singlet and octet modes. NRQCD long-distance matrix elements are currently set to unity by default, some values based on fits to experimental data. PYTHIA now provides a number of intermediate color-octet quarkonium states (see Table 13) that can be produced in color-octet subprocesses and which subsequently decay into singlet states with the emission of one or more soft gluons. Currently the branching fractions in PYTHIA have been set such that all charmonium octet states decay exclusively to the J/ψ singlet state (443) plus a gluon, and bottomonium octet states into the Υ singlet state (553) plus a gluon. The masses of the octet states have been chosen to allow this, without too much excess phase space, i.e. the emitted gluon is always very soft. The color-octet particle codes are 9900000 bigger than that of the corresponding color-singlet state (and so reside amongst the generator-specific codes). PYTHIA includes the leading order

Particle ID	Octet state
9900441	$c\bar{c}[^1S_0^{(8)}]$
9900443	$c\bar{c}[^3S_1^{(8)}]$
9910443	$c\bar{c}[^3P_0^{(8)}]$
9900551	$b\bar{b}[^1S_0^{(8)}]$
9900553	$b\bar{b}[^3S_1^{(8)}]$
9910553	$b\bar{b}[^3P_0^{(8)}]$

Table 13: PYTHIA codes (KF) for new color-octet states.

color-singlet subprocess for 3_1^S production.

$$g + g \to Q\bar{Q}[^3S_1^(1)] + g; \qquad \text{for } Q = c; b \tag{24}$$

A summary of all the available color-singlet and color-octet production subprocesses available in PYTHIA is given in Table 14. Several existing color-singlet processes are repeated in the new heavy quarkonium framework so as to provide a coherent way of defining wavefunction and matrix element normalisations for both singlet and octet modes.

There are some new PYTHIA parameter (MSEL) values which combine several quarkonium production channels together. These are presented in Table 15.

Next-to-leading-order (NLO) calculations for quarkonium production are currently only available for total cross-sections [82], so simulation of subprocesses such as $g + g \to Q\,\bar{Q}\,[^3S_1^{(1)}] + g + g$ are not yet available. This NLO contribution is thought to be of comparable magnitude to that of the $^1S_0^{(8)}$ and $^3P_J^{(8)}$ contributions and so is likely to affect the calculated values of the NRQCD matrix elements from Tevatron fits.

A.3 NRQCD matrix elements

PYTHIA includes ten long-distance matrix elements for charmonium and bottomonium production in the NRQCD framework that are currently set to unity by default. From fits to Tevatron data, many studies have provided values for these matrix elements, a sample of which is presented in Table 16. These values are used for all studies in this report unless otherwise specified. It is important to note that all ^3P_J octet states are simulated in PYTHIA using a single NRQCD matrix element $\langle\mathscr{O}(J/\psi)[^3P_0^{(8)}]\rangle$, scaled to other states using the relation [13]

$$\langle\mathscr{O}(^3P_J^{(8)})\rangle = (2J+1)\langle\mathscr{O}(^3P_0^{(8)})\rangle. \tag{25}$$

Color-singlet/octet production in PYTHIA			
Charmonium subprocesses		Bottomonium subprocesses	
421	$g+g\to c\bar{c}[^3S_1^{(1)}]+g$	461	$g+g\to b\bar{b}[^3S_1^{(1)}]+g$
422	$g+g\to c\bar{c}[^3S_1^{(8)}]+g$	462	$g+g\to b\bar{b}[^3S_1^{(8)}]+g$
423	$g+g\to c\bar{c}[^1S_0^{(8)}]+g$	463	$g+g\to b\bar{b}[^1S_0^{(8)}]+g$
424	$g+g\to c\bar{c}[^3P_J^{(8)}]+g$	464	$g+g\to b\bar{b}[^3P_J^{(8)}]+g$
425	$g+q\to q+c\bar{c}[^3S_1^{(8)}]$	465	$g+q\to q+b\bar{b}[^3S_1^{(8)}]$
426	$g+q\to q+c\bar{c}[^1S_0^{(8)}]$	466	$g+q\to q+b\bar{b}[^1S_0^{(8)}]$
427	$g+q\to q+c\bar{c}[^3P_J^{(8)}]$	467	$g+q\to q+b\bar{b}[^3P_J^{(8)}]$
428	$q+\bar{q}\to g+c\bar{c}[^3S_1^{(8)}]$	468	$q+\bar{q}\to g+b\bar{b}[^3S_1^{(8)}]$
429	$q+\bar{q}\to g+c\bar{c}[^1S_0^{(8)}]$	469	$q+\bar{q}\to g+b\bar{b}[^1S_0^{(8)}]$
430	$q+\bar{q}\to g+c\bar{c}[^3P_J^{(8)}]$	470	$q+\bar{q}\to g+b\bar{b}[^3P_J^{(8)}]$
431	$g+g\to c\bar{c}[^3P_0^{(1)}]+g$	471	$g+g\to b\bar{b}[^3P_0^{(1)}]+g$
432	$g+g\to c\bar{c}[^3P_1^{(1)}]+g$	472	$g+g\to b\bar{b}[^3P_1^{(1)}]+g$
433	$g+g\to c\bar{c}[^3P_2^{(1)}]+g$	473	$g+g\to b\bar{b}[^3P_2^{(1)}]+g$
434	$g+q\to q+c\bar{c}[^3P_0^{(1)}]$	474	$g+q\to q+b\bar{b}[^3P_0^{(1)}]$
435	$g+q\to q+c\bar{c}[^3P_1^{(1)}]$	475	$g+q\to q+b\bar{b}[^3P_1^{(1)}]$
436	$g+q\to q+c\bar{c}[^3P_2^{(1)}]$	476	$g+q\to q+b\bar{b}[^3P_2^{(1)}]$
437	$q+\bar{q}\to c\bar{c}[^3P_0^{(1)}]+g$	477	$q+\bar{q}\to b\bar{b}[^3P_0^{(1)}]+g$
438	$q+\bar{q}\to c\bar{c}[^3P_1^{(1)}]+g$	478	$q+\bar{q}\to b\bar{b}[^3P_1^{(1)}]+g$
439	$q+\bar{q}\to c\bar{c}[^3P_2^{(1)}]+g$	479	$q+\bar{q}\to b\bar{b}[^3P_2^{(1)}]+g$

Table 14: color-singlet/octet production subprocesses introduced in PYTHIA 6.324 or higher versions and their corresponding PYTHIA parameter (ISUB) subprocess numbers.

MSEL value	Switches on	ISUB
61	all charmonium processes	421-439
62	all bottomonium processes	461-479
63	both of the above	421-439 and 461-479

Table 15: New PYTHIA parameter (MSEL) subprocess menus available in PYTHIA.

In addition to this, it has been noted [83] that the p_T-behaviour of the ^3P_J and $^1S_0$ charmonia differential cross-sections above 5 GeV is virtually identical and so only a linear combination of the two contributions can be extracted from data. For this reason the matrix elements for these two states may be combined into one effective matrix element [84]. The combined differential cross-section of these two contributions can then be simulated as an appropriately-scaled $^1S_0$ cross-section. Whilst this degeneracy is not the case for bottomonia in the $0 < p_T < 15$ GeV region, the differences between the two contributions are not great enough to reliably fit them separately, so an effective matrix element may also be legitimately used for the ^3P_J and $^1S_0$ contributions in bottomonia production.

PYTHIA parameter	Value	Matrix element
PARP(141)	1.16	$\langle\mathcal{O}(J/\psi)[^3S_1^{(1)}]\rangle$
PARP(142)	0.0119	$\langle\mathcal{O}(J/\psi)[^3S_1^{(8)}]\rangle$
PARP(143)	0.01	$\langle\mathcal{O}(J/\psi)[^1S_0^{(8)}]\rangle$
PARP(144)	0.01	$\langle\mathcal{O}(J/\psi)[^3P_0^{(8)}]\rangle/m_c^2$
PARP(145)	0.05	$\langle\mathcal{O}(\chi_{c0})[^3P_0^{(1)}]\rangle/m_c^2$
PARP(146)	9.28	$\langle\mathcal{O}(\Upsilon)[^3S_1^{(1)}]\rangle$
PARP(147)	0.15	$\langle\mathcal{O}(\Upsilon)[^3S_1^{(8)}]\rangle$
PARP(148)	0.02	$\langle\mathcal{O}(\Upsilon)[^1S_0^{(8)}]\rangle$
PARP(149)	0.02	$\langle\mathcal{O}(\Upsilon)[^3P_0^{(8)}]\rangle/m_b^2$
PARP(150)	0.085	$\langle\mathcal{O}(\chi_{b0})[^3P_0^{(1)}]\rangle/m_b^2$

Table 16: Matrix element parameters in PYTHIA used in this study for charmonium and bottomonium production in the NRQCD framework (derived from data in [59]).

For J/ψ production, the effective matrix element can be written in the form:

$$M_{3.5}(^1S_0^{(8)} + {}^3P_J^{(8)}) = \langle\mathcal{O}[^3S_1^{(8)}]\rangle + 3.5\langle\mathcal{O}[^3P_J^{(8)}]\rangle/m_c^2$$

A comparison was conducted between J/ψ events simulated with an effective matrix element of 0.045 for ^3P_J and $^1S_0$ contributions and events simulated with separate matrix element parameters as given in Table 16. The two methods produce almost identical results. For the purposes of this study however, it was decided that the two contributions would be simulated separately (rather than with an effective matrix element) and combined at the analysis stage to ensure that any differences between the two contributions (particularly in the case of bottomonium) are not lost.

A.4 Event Kinematics

In this section are compared various distributions generated with PYTHIA version 6.221 (as used for the generation of the so-called Rome events) and version 6.403 used in current ATLAS software. The top plot in Figure 52 compares the transverse momentum distributions of charmonium, the middle plot — the pseudorapidity of charmonium and the bottom one — the event multiplicity of hadrons in the charmonium production events. The comparison was done using the "old showering model" in both cases (see Section A.5 for details). The events were generated with a threshold on the transverse momentum of the two outgoing muons. The highest transverse momentum muon was required to have p_T above 6 GeV and the second one above 4 GeV ($\mu6\mu4$).

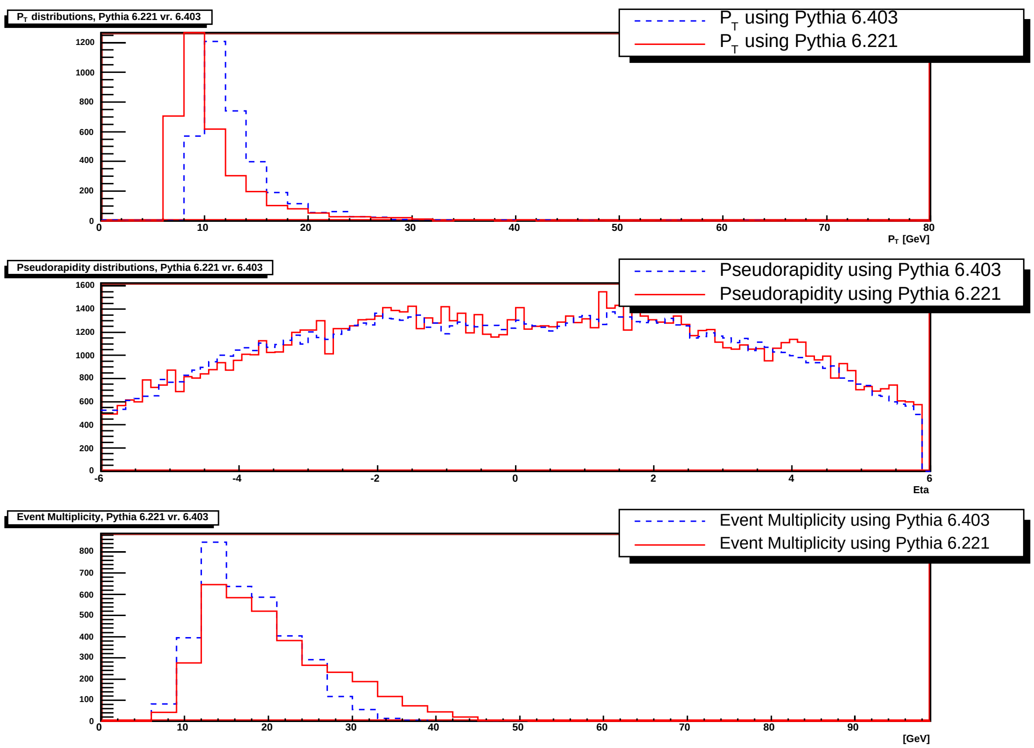

Figure 52: Events kinematics (transverse momentum, pseudorapidity and event multiplicity) for the two PYTHIA versions 6.221 (red) and 6.403 (blue).

The comparison of the two PYTHIA versions shows a good agreement in terms of the pseudorapidity, however there are slight deviations in the event multiplicity and transverse momentum distributions. The newer PYTHIA version gives slightly higher p_T at the level of about 2 GeV and its multiplicity is slightly decreased.

A.5 New showering model

Some improvements are required in the way parton showers in the energetic pp collisions expected at the LHC are simulated. Each of the commonly used Monte Carlo simulation programs such as HERWIG, ARIADNE, PYTHIA/JETSET uses somewhat different approach for simulating this complicated process. The PYTHIA authors have decided to face this complexity by developing a new scheme in which the different QCD processes, occurring when highly energetic hadrons collide, are interleaved in a common sequence ordered by decreasing transverse momentum. As a result, they open a phase space competition between multiple parton-parton interactions and radiative correction effects.

Up until now the performance of the PYTHIA old showering scheme was verified using the data collected by existing accelerators. PYTHIA tuned with the "Tune A" [85] set of parameters was able to describe the data collected with the Tevatron. Hence, the hope is that the new approach will be able to repeat the successes of the simpler approach of the old scheme, and moreover to explain and predict hadron showering effects in the much higher energy regime.

In the new scheme the branchings are taken in order of falling hardness with interplay between the multiple parton interactions and ordered initial state radiation (ISR). An ISR branching reduces the phase space available to all further branchings at a lower scale. This is true for all interactions and not just the hardest as was the case in previous PYTHIA versions. The branching of the hardest interaction will only be unaffected if it is above the P_T scales of all secondary interactions. While moving to the new multiple interaction model, with P_T-ordered ISR and final state radiation (FSR) showers, PYTHIA authors introduced a separate top-level event generation routine PYEVNW instead of the previous PYEVNT routine.

A long list of parameters has to be set differently depending on the model used. Obviously not all parameter combinations are meaningful. Therefore in the following table we give two recommended sets of parameters suitable for the old model (PYEVNT) and the new one (PYEVNW). It should be noted that the previous showering model and Multiple Interaction (MI) scenario used for older ATLAS data sets is still kept in the recent PYTHIA versions and is accessible through appropriate switches in job controle file (see for example appropriate parameters in Table 17). However one should keep in mind that the parameters of the "old" model are not available in the C++ PYTHIA version 8.

A.6 Parton distribution functions

A study was conducted into the differences between charmonium production using the CTEQ6M Parton Distribution Function (PDF) (which uses next-to-leading order calculations in the $\overline{MS}$ scheme) and the CTEQ6L1 PDF (which uses leading order calcula-

parameter	PYEVNT	PYEVNW	Description
MSTP(81)	1	21	New model, smooth ISR, high FSR
MSTP(70)	-	2	New model, smooth ISR, high FSR
MSTP(72)	-	2	New model, smooth ISR, high FSR
PARP(82)	2.0	2.50	P_{T0} and reconnect
MSTP(95)	-	1	P_{T0} and reconnect
PARP(78)	-	1.3	P_{T0} and reconnect
MSTP(82)	4	5	ExpOfPow(1.8) overlap profile
PARP(83)	0.5	1.8	When MSTP(82)=5 can vary continuously with lower cutoff at 0.4 and interesting range between 1-2.
PARP(89)	1800	1800	Reference energy & rescaling pace
PARP(90)	0.25	0.25	Reference energy & rescaling pace
PARJ(81)	-	0.14	Λ_{FSR} scale
MSTP(89)	-	1	Beam remnants
MSTP(89)	-	0	Beam remnants
PARP(79)	-	2.0	Beam remnants
PARP(80)	-	0.01	Beam remnants
PARP(67)	4	-	Scale factor for ISR
PARP(84)	0.4	-	Parameter of the assumed matter overlaps between the two colliding hadrons.
PARP(85)	0.9	-	Probability that an additional interaction in the old multiple-interaction formalism gives two gluons, with color connections to "nearest neighbours" in momentum space.
PARP(86)	0.95	-	PARP(85) or as a closed gluon loop.

Table 17: The recommended parameter sets suitable for the two different showering models implemented in the code. The second column lists the "Tune-A" set of parameters associated with the old PYEVNT routine, while the third column lists values recommended when using the new showering model PYEVNW.

tions [with a leading order α_s value]) (see [86] for further details).

Using a PYTHIA p_T-cutoff of 1.0 GeV and muon trigger cuts of 1.25 GeV on each muon and rapidity within $|y| < 0.6$, a sample of three million charmonium events was produced at CDF run II beams and energies ($p\bar{p}$, 1.96 TeV) using both CTEQ6M and CTEQ6L1. This was also compared with the LHC ATLAS setup at 14 TeV described previously with these two PDFs.

It was found that the CTEQ6L1 predicted cross-section was around 50% larger than that of the CTEQ6M sample. at both the Tevatron and LHC setups (see Table 18 for details).

	Tevatron ($p\bar{p}$, 1.96 TeV)	LHC (pp, 14 TeV)
CTEQ6L1	12 nb	37 nb
CTEQ6M	8 nb	27 nb

Table 18: Predicted PYTHIA integrated cross-sections for charmonium production at CDF run II and ATLAS.

Currently the CTEQ6L1 PDF (giving a less conservative cross-section estimate) is the default PDF used in ATLAS physics analyses. This PYTHIA study and its tuned parameters set was utilized in our J/ψ polarization p_T dependence analysis. One need to bare in mind that once the LHC data is available it will require further tunning to the Monte-Carlo parameter set. The current method can be used as a framework for the tunning process.

References

[1] S. Weinberg, Phys. Rev. Lett. 19, 1264 (1967); A. Salam, p. 367 of Elementary Particle Theory, ed. N. Svartholm (Almquist and Wiksells, Stockholm, 1969); S.L. Glashow, J. Iliopoulos, and L. Maiani, Phys. Rev. D2, 1285 (1970).

[2] P.W. Higgs: Broken Symmetries, Massless Particles and Gauge Fields, Phys. Lett. 12, 132,133, 1964

[3] D.J. Gross , F. Wilczek, Asymptotically Free Gauge Theories, Phys. Rev. D 8, 3633 (1973).

[4] K. Hagiwara , K. Hikasa, Searches for Quark and Lepton Compositeness, in Review of Particle Physics Phys. Lett. B 592, (2004).

[5] C. Amsler , Non-qq Candidates, in Review of Particle Physics Phys. Lett. B 592, (2004).

[6] For some examples, see C. Quigg,Gauge Theories of the Strong,Weak and Electromagnetic Interactions, Addison-Wesley (1984), pp.11-15.

[7] C. Quigg, Realizing the Potential of Quarkonium, FERMILAB-CONF-97-266-T (1997).

[8] I. Hinchliffe, Quantum Chromodynamics, in Review of Particle Physics Phys. Lett. B 592, (2004).

[9] E. Braaten ,T.C. Yuan , ”Gluon Fragmentation into Heavy Quarkonium”, Phys. Rev. Lett. 71, 1673 (1993).

[10] For a detailed discussion of heavy quark production, see for example, R.K. Ellis, W.J. Stirling , B.R. Webber, ”QCD and Collider Physics”, Cambridge University Press (1996), pp. 347-384.

[11] J.F. Amundson et al., ”Quantitative Tests of Color Evaporation: Charmonium Production”, Phys. Lett. B390, 323 (1997).

[12] See e.g. V. G. Kartvelishvili, A. K. Likhoded, S. R. Slabospitsky, Sov. J. Nucl. Phys. **28** (1978) 280; M. Gluck, J. F. Owens and E. Reya, “Gluon Contribution To Hadronic J/ψ Production,” Phys. Rev. D **17** (1978) 2324; V. G. Kartvelishvili, A. K. Likhoded, Sov. J. Nucl. Phys. **39** (1984) 298.

[13] G.T. Bodwin, E. Braaten , G.P. Lepage, ”Rigorous QCD Analysis of Inclusive Annihilation and Production of Heavy Quarkonium”, Phys. Rev. D 51, 1125 (1995), Erratum ibid. D55, 5853 (1997).

[14] W.E. Caswell , G.P. Lepage, ”Effective Lagrangians for Bound State Problems in QED, QCD, and Other Field Theories”, Phys. Lett. B167, 437 (1986)

[15] A. Manohar, Effective Field Theories, in ”Schladming 1996, Perturbative and non-perturbative aspects of quantum field theory” (1996).

[16] E. Braaten, S. Fleming , T.C. Yuan, ”Production of Heavy Quarkonium in High Energy Colliders”, Ann. Rev. Nucl. Part. Sci. 46, 197 (1996).

[17] P. Cho , A. Leibovich, ”Color-Octet Quarkonium Production”, Phys. Rev. D 53, 150 (1996); idem, Color-Octet Quarkonium Production. II, Phys. Rev. D 53, 6203 (1996).

[18] M. Beneke , M. Kramer, ”Direct J/ψ and ψ Polarization and Cross Sections at the Tevatron”, Phys. Rev. D 55, 5269 (1997). 44

[19] M.A. Sanchis-Lozano , B. Cano-Coloma, ”Charmonia production in hadron colliders and the extraction of color-octet matrix elements”, Nucl. Phys. B508, 753 (1997).

[20] B.A. Kniehl , G. Kramer, Inclusive J/ψ and $\psi(2S)$ Production from B Decay in p-p Collisions, Phys. Rev. D 60, 014006 (1999).

[21] B.A. Kniehl , G. Kramer, ”Tevatron-HERA Color Octet Charmonium Anomaly Versus Higher-Order QCD Effects”, Eur. Phys. J. C 6, 493 (1999).

[22] M. Beneke, I.Z. Rothstein , M.B. Wise, ”Kinematic Enhancements of Non- Perturbative Corrections to Quarkonium Production”, Phys. Lett. B408, 373 (1997).

[23] C-Y. Wong,”The Soft Gluon Emission Process in the Color-Octet Model for Heavy Quarkonium Production”, Phys. Rev. D 60, 114025 (1999).

[24] E. Braaten , S. Fleming, Color-Octet Fragmentation and the 0 Surplus at the Tevatron, Phys. Rev. Lett. 74, 3327 (1995).

[25] L.V. Gribov, E.M. Levin, Phys. Rep. 100, (1983).

[26] E. M. Levin and M. G. Ryskin, Phys. Rep. 189, 267 (1990).

[27] S. Catani, M. Ciafaloni, and F. Hautmann, Phys. Lett. B 242, 97 (1990); Nucl. Phys. B366, 135 (1991).

[28] J. C. Collins and R. K. Ellis, Nucl. Phys. B360, 3 (1991).

[29] E. A. Kuraev, L. N. Lipatov, and V. S. Fadin, Sov. Phys. JETP 45, 199 (1977); Ya. Balitski and L. N. Lipatov, Sov. J. Nucl. Phys. 28, 822 (1978).

[30] M. Ciafaloni, Nucl. Phys. B296, 49 (1998); S. Catani, F. Fiorani,and G. Marchesini, Phys. Lett. B 234, 339 (1990); Nucl.Phys. B336, 18 (1990); G. Marchesini, ibid. B445, 49 91995).

[31] V. N. Gribov and L. N. Lipatov, Sov. J. Nucl. Phys. 15, 438 (1972); G. Altarelli and G. Parisi, Nucl. Phys. B126, 298 (1977); Yu. L. Dokshitzer, Sov. Phys. JETP 46, 641 (1977)

[32] E. M. Levin, M. G. Ryskin, Yu. M. Shabelski, and A. G. Shuvaev, Sov. J. Nucl. Phys. 53, 1059 (1991); 54, 1420 (1991); M.G. Ryskin, Yu. M. Shabelski, and A. G. Shuvaev, Z. Phys. C 69, 269 (1996).

[33] J. R. Forshaw and R. G. Roberts, Phys. Lett. B 335, 494 (1994).

[34] V. Del Duca, Sci. Acta 10, 91 (1995).

[35] V. A. Saleev and N. P. Zotov, Mod. Phys. Lett. A 9, 151 (1994); 11, 25 (1996).

[36] A. V. Lipatov and N. P. Zotov, Mod. Phys. Lett. A 15, 695 (2000); A. V. Lipatov, V. A. Saleev, and N. P. Zotov, ibid. 15, 1727 (2000).

[37] S. P. Baranov and N. P. Zotov, Phys. Lett. B 458, 389 (1999).

[38] S. P. Baranov, H. Jung, and N. P. Zotov, Nucl. Phys. Proc. Suppl. B99, 192 (2000).

[39] H. Jung, in Proceedings of the Workshop on Monte Carlo Generators, edited by A. Doyle, G. Grindhammer, G. Ingelman, and H. Jung DESY, Hamburg, (1999), p. 75.

[40] S. P. Baranov and N. P. Zotov, Phys. Lett. B 491, 111 (2000).

[41] S. P. Baranov and M. Smizanska, Phys. Rev. D 62, 014012 (2000).

[42] Ph. Hagler, R. Kirschner, A. Sha?fer, L. Szymanowski, and O. V. Teryaev, Phys. Rev. D 62, 071502 (2000).

[43] F. Yuan and K.-T. Chao, Phys. Rev. D 63, 034006 (2001).

[44] Ph. Hagler, R. Kirschner, A. Shafer, L. Szymanowski, and O.V. Teryaev, Phys. Rev. Lett. 86, 1446 (2001).

[45] S. P. Baranov, Phys. Lett. B 428, 377 (1998).

[46] R. Brugnera, in Deep Inelastic Scattering, Proceedings of the Ninth International Workshop, Bologna, Italy, 2001, edited by G. Bruni, G. Iacobucci, and R. Nania World Scientific, Singapore,(2002).

[47] H1 Collaboration, C. Adloff et al., Eur. Phys. J. C 25, 25 (2002). Nucl. Phys. B174, 317 (1980).

[48] E. Braaten and S. Fleming, Phys. Rev. Lett. 74, 3327 (1995).

[49] E. L. Berger and D. L. Jones, "Inelastic Photoproduction Of J/ψ And Upsilon By Gluons," Phys. Rev. D **23** (1981) 1521; B. Humpert, "Narrow Heavy Resonance Production By Gluons," Phys. Lett. B **184** (1987) 105.

[50] F. Abe *et al.* [CDF Collaboration], "Inclusive J/ψ , psi (2S) and b quark production in anti-p p collisions at s**(1/2) = 1.8-TeV," Phys. Rev. Lett. **69** (1992) 3704.

[51] M. Kramer, "Quarkonium production at high-energy colliders," Prog. Part. Nucl. Phys. **47** (2001) 141 [arXiv:hep-ph/0106120].

[52] E. Braaten and S. Fleming, "Color octet fragmentation and the psi-prime surplus at the Tevatron" Phys. Rev. Lett. **74** (1995) 3327 [arXiv:hep-ph/9411365].

[53] G. T. Bodwin, E. Braaten and G. P. Lepage, "Rigorous QCD predictions for decays of P wave quarkonia," Phys. Rev. D **46** (1992) 1914 [arXiv:hep-lat/9205006].

[54] M. Cacciari and M. Kramer, "Color-Octet Contributions to J/Psi Photoproduction," Phys. Rev. Lett. **76** (1996) 4128 [arXiv:hep-ph/9601276].

[55] C. Adloff *et al.* [H1 Collaboration], "Charmonium production in deep inelastic scattering at HERA," Eur. Phys. J. C **10** (1999) 373 [arXiv:hep-ex/9903008].

[56] A. Abulencia *et al.* [CDF Collaboration], "Polarization of J/ψ and ψ_{2S} mesons produced in $p\bar{p}$ collisions at $\sqrt{s}$ = 1.96-TeV," Phys. Rev. Lett. **99** (2007) 132001 [arXiv:0704.0638 [hep-ex]].

[57] J. P. Lansberg, J. R. Cudell and Yu. L. Kalinovsky, "New contributions to heavy quarkonium production," Phys. Lett. B **633** (2006) 301 [arXiv:hep-ph/0507060]; P. Artoisenet, J. P. Lansberg and F. Maltoni, "Hadroproduction of J/[psi] and [Upsilon] in association with a heavy-quark pair" Phys. Lett. **B653**, 60 (2007).

[58] T. Sjostrand, S. Mrenna and P. Skands, "PYTHIA 6.4: Physics and manual," JHEP **0605** (2006) 026 [arXiv:hep-ph/0603175].

[59] P. Nason *et al.*, "Bottom production," arXiv:hep-ph/0003142.

[60] LHC Study Group, The Large Hadron Collider: Conceptual Design, CERN-AC-95-5, 1995.

[61] ATLAS Collaboration, ATLAS Technical Proposal for a General-Purpose pp Experiment at the Large Hadron Collider at CERN, CERN/LHCC/94-43, 1994.

[62] ATLAS Inner Detector Community, ATLAS Inner Detector Technical Design Report, CERN/LHCC/97-16 17, (1997).

[63] ATLAS Collaboration, ATLAS Calorimeter Performance Technical Design Report, CERN/LHCC/96-40, (1997).

[64] ATLAS Muon Collaboration, ATLAS Muon Spectrometer Technical Design Report, CERN/LHCC/97-22, 1997.

[65] E. Etzion, J.Ginzburg etc. "The Certification of ATLAS Thin Gap Chambers Produced in Israel and China" TAUP 2787-04 15 Nov (2004)

[66] E. Etzion,Y. Benhammou, J. Ginzburg etc. "The Cosmic Ray Hodoscopes for Testing Thin Gap Chambers at the Technion and Tel-Aviv University", Transactions on Nuclear Science, volume51, number 5, pp2091-2096 (2004)

[67] F. Abe et al., The CDF Collaboration, Υ Production in $p\bar{p}$ Collisions at $\sqrt{s} = 1.8 TeV$, Phys. Rev. Lett 75, 4358 (1995).

[68] F. Abe et al., The CDF Collaboration, J/ψ and $\psi(2S)$ Production in $p\bar{p}$ Collisions at $\sqrt{s} = 1.8 TeV$, Phys. Rev. Lett 79, 572 (1997).

[69] V. M. Abazov *et al.* [D0 Collaboration], DØ Note 5089-conf.

[70] S. P. Baranov, "Highlights from the kT-factorization approach on the quarkonium production puzzles," Phys. Rev. D **66** (2002) 114003.

[71] V. G. Kartvelishvili and A. K. Likhoded, Yad. Fiz. **40** (1984) 1273.

[72] V. V. Braguta, A. K. Likhoded and A. V. Luchinsky, "Observation potential for chi/b at the Tevatron and LHC," Phys. Rev. D **72** (2005) 094018 [arXiv:hep-ph/0506009].

[73] A. V. Luchinsky, "Determination of chi/b spin in the decays chi/b0,2 –¿ psi psi and chi/b0,2–¿ psi psi –¿ 2(mu+ mu-)," arXiv:hep-ph/0604129.

[74] N. Brambilla *et al.* [Quarkonium Working Group], "Heavy quarkonium physics," arXiv:hep-ph/0412158. HEP-PH/0412158;

[75] ATLAS Collaboration, CSC-Note, "Triggering low p_T muons and di-muons for B physics".

[76] J. Marriner "Secondary Vertex Fit with Mass and Pointing Constrains (CTVMFT)" CDF Note 1996.

[77] W.-M. Yao et al. ”The Review of Particle Physics”, Journal of Physics, G 33, 1 (2006) and 2007 partial update for 2008. http://pdg.lbl.gov/

[78] ATLAS Collaboration, CSC-Note, ”*B* physics J/Psi moun trigger efficiency”.

[79] A. Dewhurst, J. Ginzburg, D. Price, M. Smizanska, T. Stahl, W. Walkowiak, “Low pT muon and di-muon rates in ATLAS” [ATL-COM-PHYS-2007-089]

[80] J.D. Jackson, Particle and Polarization Angular Distributions, in High Energy Physics (Les Houches 1965) ed. C. DeWitt M. Jacob, Gordon and Breach Science Publishers (1965).

[81] E. Etzion, J. Ginzburg, V. Kartvelishvili, D. Price (2006). ”Heavy Quarkonium Production Simulations at ATLAS, [ATL-PHYS-INT-2007-001]

[82] A. Petrelli, M. Cacciari, M. Greco, F. Maltoni and M. L. Mangano, “NLO production and decay of quarkonium,” Nucl. Phys. B **514** (1998) 245 [arXiv:hep-ph/9707223].

[83] P. L. Cho and A. K. Leibovich, “color-octet quarkonia production II,” Phys. Rev. D **53** (1996) 6203 [arXiv:hep-ph/9511315].

[84] M. A. Sanchis-Lozano, “New extraction of color-octet NRQCD matrix elements from charmonium hadroproduction,” Nucl. Phys. Proc. Suppl. **86** (2000) 543 [arXiv:hep-ph/9907497].

[85] R. D. Field, Matrix elements and Monte Carlo Tuning Workshop, Fermilab October 2002, http://cepa.fnal.gov/CPD/MCTuning/.

[86] J. Pumplin, D. R. Stump, J. Huston, H. L. Lai, P. Nadolsky and W. K. Tung, “New generation of parton distributions with uncertainties from global QCD analysis,” JHEP **0207** (2002) 012 [arXiv:hep-ph/0201195].